

# **Full-wave Moment Tensor and Tomographic Inversions Based on 3D Strain Green Tensor**

**Yang Shen  
Xiaoping Yang**

**Science Applications International Corporation  
4001 N. Fairfax Drive  
Arlington, VA 22209**

**Final Report**

**31 January 2010**

**APPROVED FOR PUBLIC RELEASE; DISTRIBUTION IS UNLIMITED.**



**AIR FORCE RESEARCH LABORATORY  
Space Vehicles Directorate  
29 Randolph Rd  
AIR FORCE MATERIEL COMMAND  
HANSCOM AFB, MA 01731-3010**

---

## NOTICES

Using Government drawings, specifications, or other data included in this document for any purpose other than Government procurement does not in any way obligate the U.S. Government. The fact that the Government formulated or supplied the drawings, specifications, or other data does not license the holder or any other person or corporation; or convey any rights or permission to manufacture, use, or sell any patented invention that may relate to them.

This report was cleared for public release and is available to the general public, including foreign nationals. Qualified requestors may obtain copies of this report from the Defense Technical Information Center (DTIC) (<http://www.dtic.mil>). All others should apply to the National Technical Information Service.

AFRL-RV-HA-TR-2010-1011 HAS BEEN REVIEWED AND IS APPROVED FOR PUBLICATION IN ACCORDANCE WITH ASSIGNED DISTRIBUTION STATEMENT.

//signature//

---

ROBERT J. RAISTRICK  
Contract Manager

//signature//

---

Domenic Thompson, Maj, USAF, Chief  
Battlespace Surveillance Innovation Center

This report is published in the interest of scientific and technical information exchange, and its publication does not constitute the Government's approval or disapproval of its ideas or findings.

REPORT DOCUMENTATION PAGE				Form Approved OMB No. 0704-0188	
Public reporting burden for this collection of information is estimated to average 1 hour per response, including the time for reviewing instructions, searching existing data sources, gathering and maintaining the data needed, and completing and reviewing this collection of information. Send comments regarding this burden estimate or any other aspect of this collection of information, including suggestions for reducing this burden to Department of Defense, Washington Headquarters Services, Directorate for Information Operations and Reports (0704-0188), 1215 Jefferson Davis Highway, Suite 1204, Arlington, VA 22202-4302. Respondents should be aware that notwithstanding any other provision of law, no person shall be subject to any penalty for failing to comply with a collection of information if it does not display a currently valid OMB control number. <b>PLEASE DO NOT RETURN YOUR FORM TO THE ABOVE ADDRESS.</b>					
1. REPORT DATE (DD-MM-YYYY) 01-31-2010		2. REPORT TYPE Final Report		3. DATES COVERED (From - To) 02-28-2006 to 12-31-2009	
4. TITLE AND SUBTITLE Full-wave Moment Tensor and Tomographic Inversions Based on 3D Strain Green Tensor				5a. CONTRACT NUMBER FA8718-06-C-0014	
				5b. GRANT NUMBER	
				5c. PROGRAM ELEMENT NUMBER 62601F	
6. AUTHOR(S) Yang Shen <sup>1</sup> and Xiaoping Yang				5d. PROJECT NUMBER 1010	
				5e. TASK NUMBER SM	
				5f. WORK UNIT NUMBER A1	
7. PERFORMING ORGANIZATION NAME(S) AND ADDRESS(ES)  Science Applications International Corporation 4001 Fairfax Drive Arlington, VA 22209				8. PERFORMING ORGANIZATION REPORT NUMBER	
9. SPONSORING / MONITORING AGENCY NAME(S) AND ADDRESS(ES)  Air Force Research Laboratory 29 Randolph Rd. Hanscom AFB, MA 01731-3010				10. SPONSOR/MONITOR'S ACRONYM(S)  AFRL/RVBYE	
				11. SPONSOR/MONITOR'S REPORT NUMBER(S) AFRL-RV-HA-TR-2010-1011	
12. DISTRIBUTION / AVAILABILITY STATEMENT  Approved for Public Release; Distribution Unlimited.					
13. SUPPLEMENTARY NOTES  <sup>1</sup> Graduate School of Oceanography, University of Rhode Island, South Ferry Rd., Narragansett, RI 02882					
14. ABSTRACT We developed a unified source moment tensor and tomographic inverse method based on finite-difference simulations of wave propagation at local to teleseismic distances. The new method accounts for complex wave propagation in three-dimensional (3D) earth, linearizes the inverse problem by iteratively updating the earth model, and provides an accurate way to integrate body- and surface-wave observations. The finite-difference methods developed to date make it possible to construct hierarchical FD-SGT databases efficiently and with great flexibility. The spherical finite-difference method is well suited for regional and global wave propagation, while the finite-difference method with boundary-conforming grids that follow topography provides higher accuracy at local and near regional scales. The self-consistent FD-SGT databases constructed from finite-difference simulations of wave propagation in full-wave tomographic models can be used to determine the moment tensors within minutes after a seismic event, making it possible for real time monitoring using 3D models.					
15. SUBJECT TERMS Seismic velocity models, Moment tensors, Seismic tomography, Finite frequency, Finite difference					
16. SECURITY CLASSIFICATION OF:			17. LIMITATION OF ABSTRACT	18. NUMBER OF PAGES	19a. NAME OF RESPONSIBLE PERSON
a. REPORT UNCLASSIFIED	b. ABSTRACT UNCLASSIFIED	c. THIS PAGE UNCLASSIFIED			Robert Raistrick
			SAR	129	19b. TELEPHONE NUMBER (include area code) 781-377-3726

## Table of Contents

<b>1. SUMMARY .....</b>	<b>1</b>
<b>2. INTRODUCTION.....</b>	<b>1</b>
<b>3. METHODS, ASSUMPTIONS, AND PROCEDURES.....</b>	<b>3</b>
<b>3.1 Overview of Unified Tomography and Source Moment Tensor Inversion     Based on FD-SGT Databases .....</b>	<b>3</b>
<b>3.2. Finite-Difference Wave Simulations .....</b>	<b>4</b>
<b>3.3. Source Characterization and Construction of Hierarchical FD-SGT Database     .....</b>	<b>5</b>
<b>3.4. Sensitivity Kernels Based on 3D Reference Model and Full Wave     Tomography .....</b>	<b>6</b>
<b>4. DISCUSSION AND CONCLUSIONS .....</b>	<b>7</b>
<b>5. RECOMMENDATIONS.....</b>	<b>8</b>
<b>REFERENCES.....</b>	<b>17</b>
<b>LIST OF SYMBOLS, ABBREVIATIONS, AND ACRONYMS .....</b>	<b>20</b>
<b>APPENDIX A .....</b>	<b>A-1</b>
<b>APPENDIX B .....</b>	<b>B-1</b>
<b>APPENDIX C .....</b>	<b>C-1</b>
<b>APPENDIX D .....</b>	<b>D-1</b>

## List of Figures

<b>Figure 1 Schematic illustration of the unified tomography and moment tensor inversions based on 3D FD-SGT databases.....</b>	<b>9</b>
<b>Figure 2 Comparisons between the 3-component synthetics calculated by the spherical finite-difference algorithm and normal-mode summation. ....</b>	<b>10</b>
<b>Figure 3 Selected earthquakes in the southeast Tibetan plateau during 2001-2004 and the stations used in moment tensor inversions.....</b>	<b>11</b>
<b>Figure 4 Comparison of the FD-SGT and GCMT solutions for 13 earthquakes during 2001-2004 in the southeast Tibetan plateau. ....</b>	<b>12</b>
<b>Figure 5 Observed waveforms are compared with the synthetics for the best source moment tensor solution. ....</b>	<b>13</b>
<b>Figure 6 The relative magnitudes of the integrated absolute P traveltime and amplitude sensitivities to S- and P-speed perturbations. ....</b>	<b>14</b>
<b>Figure 7 Phase sensitivity kernels of a regional Rayleigh wave to S wave-speed and P wave-speed perturbations relative to a 3D reference model. ....</b>	<b>15</b>
<b>Figure 8 P wave velocity variations at 8 km depth in the southeast Tibetan plateau. ....</b>	<b>16</b>

## ACKNOWLEDGMENTS

We thank Dr. Li Zhao for his contributions to the development of the finite-difference, scattering-integral method. Dr. Zhao is the co-author of several papers published or under preparation as the results of this project. The wave propagation simulations are carried out on a Beowulf PC cluster purchased with a grant from the National Science Foundation. This work would not be possible without the creativity and dedication of the students and postdocs directly or indirectly involved in the project, especially Mr. Zhigang Zhang and Dr. Wei Zhang.



## 1. SUMMARY

We developed a unified source moment tensor and tomographic inverse method based on finite-difference simulations of wave propagation at local to teleseismic distances. The new method accounts for complex wave propagation in three-dimensional (3D) earth, linearizes the inverse problem by iteratively updating the earth model, and provides an accurate way to integrate body- and surface-wave observations. These developments include:

- (1) A non-staggered-grid finite-difference code in the spherical coordinate system for simulation of regional and global wave propagation (Zhang et al., manuscript in preparation, hereinafter Zhang et al., 2010),
- (2) A new and efficient implementation of the Perfectly Matched Layer (PML) that provides a better performance in simulation of waves incident at a near-grazing angle, low frequency waves and evanescent waves (Zhang and Shen, submitted, 2009; Appendix A),
- (3) Earthquake location and moment tensor inversion using hierarchical Finite-Difference Strain Green tensor (FD-SGT) databases (Shen et al., submitted, 2009; Appendix B), and
- (4) Full-wave tomographic inversion of body and surface waves for a joint P and S velocity model. This full-wave tomography is based on an accurate representation of finite-frequency Pn/Sn waves (Zhang et al., 2007), a fuller utilization of an arrival on all three components of seismic records (Shen et al., 2008a), and the dependency of P waveforms on S velocity anomalies (Zhang and Shen, 2008; Appendix C) and Rayleigh waveforms on P velocity anomalies. As an example we have successfully applied the full-wave tomography method to the southeast Tibetan plateau (Shen et al., 2008b; Zhang et al., 2009; Appendix D).

The finite-difference methods developed to date make it possible to construct hierarchical FD-SGT databases efficiently and with great flexibility. The spherical finite-difference method is well suited for regional and global wave propagation, while the finite-difference method with boundary-conforming grids that follow topography provides higher accuracy at local and near regional scales. The self-consistent FD-SGT databases constructed from finite-difference simulations of wave propagation in full-wave tomographic models can be used to determine the moment tensors within minutes after a seismic event, making it possible for real time monitoring using 3D models.

## 2. INTRODUCTION

Accurate 3D earth models are essential for accurate predictions of seismic observables and source characterization. While recovering the true form and magnitude of earth structure has always been the goal of tomographic inversion, recent studies show that methods based on full wavefields in 3D reference models have several distinct advantages in relating seismic observations to highly heterogeneous Earth structures. Made possible by advance in high-performance computation, this full-wavefield



approach accounts for complex wave propagation in 3D heterogeneous earth (Zhao et al., 2005; Tromp et al., 2005; Liu and Tromp, 2006; Zhang et al., 2007), enables fuller utilization of an arrival on all three components of seismic records (Shen et al., 2008a), and linearizes the inverse problem by iteratively updating the 3D reference model. An important benefit of physically realistic and accurate modeling of full wavefields in 3D models is the consistency of the system of equations in inversion. This is particularly important for the integration of different types of observations (P, S, surface waves including empirical Green's functions derived from ambient noise) in inversion, which is an essential step to obtain a coherent and self-consistent model of the crust and mantle. Seismic tomography based on path- or structure-averaging (rays) and 1D or 2D reference models does not accurately place the 3D sensitivities of seismic observations in a complex 3D model. The mismatch in sensitivities due to approximations in theory becomes problematic when the target resolution is at scales smaller than the Fresnel zone. For example, a 1-Hz P/Pn wave recorded by a receiver ~1000 km from the source has a Fresnel zone width of ~200 km in the middle of the wave path. van der Lee and Frederiksen (2005) recognize that a more consistent and linear system of equations offered by the full-wavefield approach would fit the combined data sets better under comparable regularization biases.

In this field two methods have been developed so far to carry out full-wave tomography iteratively with 3D reference models. One is the adjoint-wavefield (AW) method, which back-propagates the data from receivers to image structure (Tromp et al., 2005; Liu and Tromp, 2006). The other is the Strain Green Tensor (SGT) based, scattering-integral (SI) method, which calculates and stores the sensitivity kernels for each data functional (Zhao et al., 2005; Zhang et al., 2007). Both methods are based on the same full wave theory. The main differences are in their computational approaches. In general, the adjoint method is CPU intensive, while the SGT database approach requires a large disk space and fast network. Chen et al. (2007a) provided a comparison of the AW and SI methods. We note that an advantage of the SI method is that the SGT databases can also be used in source moment tensor inversions, making it possible to account for complex wave propagation in 3D reference models in real time seismic monitoring. To date, the AW and SI methods use two different approaches to calculating synthetic waveforms: the spectral-element method (SEM) (Komatitsch et al., 2002) and finite-difference method (Olsen, 1994; Zhang et al., 2008; Zhang et al., 2010), respectively.

## METHOD, ASSUMPTIONS, AND PROCEDURES

### 3.1 Overview of Unified Tomography and Source Moment Tensor Inversion Based on FD-SGT Databases

In the SGT-based approach, the displacement can be expressed as (Zhao et al., 2006),

$$\begin{aligned}
 u_n(\mathbf{r}; \mathbf{r}_s) &= \partial_i^{\mathbf{r}} G_{nj}(\mathbf{r}; \mathbf{r}_s) M_{ji} \\
 &= \frac{1}{2} [\partial_i^{\mathbf{r}} G_{jn}(\mathbf{r}_s; \mathbf{r}) + \partial_j^{\mathbf{r}} G_{in}(\mathbf{r}_s; \mathbf{r})] M_{ji} \\
 &= H_{ijn}(\mathbf{r}_s; \mathbf{r}) M_{ji}
 \end{aligned} \tag{1}$$

where  $\mathbf{r}$  is the location vector,  $\mathbf{r}_s$  is the source location,  $M_{ji}$  the source moment tensor component ( $i, j=1-3$ ),  $G(\mathbf{r}; \mathbf{r}_s)$  and  $G(\mathbf{r}_s; \mathbf{r})$  the Green tensors for a unit impulsive force at the source and  $\mathbf{r}$ , respectively, and  $H_{ijn}(\mathbf{r}_s; \mathbf{r})$  the strain Green tensor composed of the spatial gradient of the Green tensors. The subscript  $n$  denotes the component of the displacement. The source-receiver reciprocity and the symmetry of the moment tensor have been applied in Equation 1. Notice the SGT can be at any location in the medium and thus can also be at the receiver location  $\mathbf{r}_R$ . Equation 1 is the basis upon which the FD-SGT moment tensor inversions are developed (Zhao et al., 2006; Shen et al., 2009).

The waveform change at  $\mathbf{r}_R$  due to a local model perturbation at an arbitrary position  $\mathbf{r}$ , can be expressed as (Zhao et al., 2006):

$$\delta u_n(\mathbf{r}_R; \mathbf{r}_s) = H_{ijn}(\mathbf{r}; \mathbf{r}_R) \delta C_{ijkl}(\mathbf{r}) \varepsilon_{lk}(\mathbf{r}; \mathbf{r}_s) \tag{2}$$

where  $\delta C_{ijkl}(\mathbf{r})$  is the perturbation of the fourth-order elasticity tensor and  $\varepsilon_{lk}(\mathbf{r}; \mathbf{r}_s)$  is spatial gradient elements of the displacement vector, which requires one forward wave simulation from the source. The total waveform change due to the model perturbation in the entire volume in the model can be found by volume integration of Equation 2. The above waveform perturbation equation is the essential ingredient in the SGT-based tomographic method. The Fréchet kernels relating elastic and anelastic properties to any seismic data, such as the frequency-dependent traveltime and amplitude anomalies, can be obtained from it (Zhao et al., 2005; Zhang et al., 2007; Zhang and Shen, 2008).

Figure 1 provides a schematic illustration of our unified and self-consistent source moment tensor and tomography inversion based on 3D FD-SGT databases. Station SGT databases are constructed from an initial 3D reference model by finite-difference simulation of the responses to orthogonal unit impulsive point force acting at the stations. The SGTs in a small volume surrounding the source reference location extracted from the databases make it possible to invert for source moment tensors and location in a global optimization scheme. Forward wave propagation simulation from the source in the 3D reference model provides synthetic waveforms at the station and within the entire model. Travel time, amplitude, and other waveform anomalies are measured from the observed and synthetic waveforms at stations. The forward wave field (from the source) and the station SGTs are used to calculate the finite-frequency sensitivities of the measurements

to perturbations in  $V_p$ ,  $V_s$  (or bulk and shear moduli), density, and attenuation. Together with the sensitivities to source parameters, the measurements and structural sensitivity kernels are used to invert for the earth structure. The tomographic inversion results are added to the 3D reference model and validated. This process can be repeated to progressively improve the model resolution.

## 3.2. Finite-Difference Wave Simulations

An accurate, efficient, and easy-to-use numerical method is the most basic tool in seismic studies using 3D reference models. Researchers have developed several methods to simulate wave propagation in 3D models. These include finite-difference, pseudo spectral, spectral element, and finite-element methods (e.g., Hung and Forsyth, 1998; Igel et al., 2002; Komatitsch et al., 2002). In particular, the spectral element method (SEM) has been used in the adjoint-wavefield tomography and source moment tensor inversions (e.g., Liu et al., 2004; Tromp et al., 2008). The SGT databases can be constructed using any numerical method, though we have focused on the development of the finite-difference method for several reasons. The finite-difference method does not require the grid mesh to conform to interior boundary topography (Moczo et al. 2007). It is thus relatively straightforward to apply the method to various regions. The finite-difference computation can be easily parallelized on high-performance distribute-memory computers. It is also one of the most widely used numerical methods in seismological studies.

Previous finite-difference simulations of wave propagation in spherical earth were based on staggered grids, which needed interpolation to generate values not located on staggered location, causing a loss of precision (Igel et al., 2002). To overcome this problem, we implement a finite-difference algorithm with non-uniform, non-staggered grids in a spherical coordinate system (Zhang et al., 2010). No interpolation is needed during the calculation in this scheme. The spatial finite-difference operator is the DRP/opt MacCormack scheme (Hixon, 1997; Zhang and Chen, 2006), whose formal accuracy is 4<sup>th</sup> order with optimization in numerical dispersion and dissipation errors; the time marching scheme can be 2<sup>nd</sup>-order Euler or 4<sup>th</sup>-order Runge-Kutta based on the trade-off between accuracy and computational efficiency. This implementation enables us to accurately simulate seismic waves in a spherical Earth with the fluid layer and 3D variations in wave speeds and attenuation. A number of numerical experiments have been conducted to validate the spherical finite-difference code by comparing the simulation results with the synthetics calculated by normal-mode summation (Figure 2).

At local to near regional scales, scattering of short-period waves by topography becomes important. To account for topography effects, we have implemented a 3D version of the traction imaging method (Zhang and Chen, 2006) to simulate wave propagation in the presence of irregular free surface (Zhang et al., 2008). The spatial finite-difference operator is the DRP/opt MacCormack scheme (Hixon, 1997); the time marching scheme is 4<sup>th</sup>-order Runge-Kutta. In this algorithm, boundary-conforming grids follow surface topography, avoiding the artifacts associated with the staircase approximation to arbitrarily irregular surface. For example, the simulation of strong ground motion after the May 12, 2008 Wenchuan earthquake at the east margin of the Tibetan plateau incorporates a 3D earth model (CRUST 2.0, Bassin et al, 2000), finite-

fault rupture, and realistic surface topography (Zhang et al., 2008). The model has a dimension of  $700 \text{ km} \times 300 \text{ km} \times 80 \text{ km}$  in the fault-parallel (N50°E), fault-normal (N40°W), and vertical directions, respectively. It is discretized with a horizontal-grid spacing of 500 m and variable vertical-grid spacing from 200 m near the surface to 1.5 km near 80 km depth. The simulation provided reliable synthetic waveforms up to  $\sim 0.33 \text{ Hz}$  in the sediment basin and up to  $\sim 0.8 \text{ Hz}$  elsewhere. One of the conclusions of the simulation is that rough topography above the rupture fault causes wave scattering, resulting in significantly larger peak ground motion on the apex of topographic relief than in the valley. Topography and scattering also reduce the wave energy in the forward direction of fault rupture but increase the peak ground motion in other parts of the basin. These results suggest the need for a localized hazard assessment in places of rough topography that takes topographic effects into account. From a technical point of view, this simulation was carried out on a 104 cpu-core cluster, demonstrating that it is feasible to simulate broadband wave propagation at regional distances on a moderate supercomputer.

Finally, we note that the perfectly matched layer (PML) has been widely used in seismic wave modeling to absorb waves at nonphysical boundaries surrounding the computational domain. However, the traditional PML performs poorly in absorbing low-frequency waves, evanescent waves or waves at grazing incidence. We developed an unsplit-field, complex frequency-shifted perfectly matched layer implementation using auxiliary differential equations (CFS ADE-PML) in seismic wave modeling (Zhang and Shen, 2009). One of the advantages of the CFS ADE-PML implementation is that it is straightforward to use with a higher-order time matching scheme to achieve a higher-order accuracy.

### **3.3. Source Characterization and Construction of Hierarchical FD-SGT Database**

Most earthquake source studies to date utilize 1D earth models in the calculation of synthetic waveforms or Green's functions. To accommodate 3D structural heterogeneities, segments of body and surface waves are time-shifted before waveform fitting (e.g., Zhao & Helmberger, 1994; Zhu & Helmberger, 1996). In places with highly heterogeneous structure, this “cut-and-paste” of waveform segments may not fully account for the complexity of wave phenomena caused by 3D structures (e.g., wave focusing/defocusing). Furthermore one of the major sources of errors in moment tensor inversion is phase skipping between the observed and synthetic waveforms. When traveltimes delays due to 3D velocity heterogeneities are comparable to or larger than the wave period, phase skipping becomes a challenging problem.

Advance in computation has made the use of 3D Green's function in earthquake source inversion an increasingly attractive option in routine operation. Liu et al. (2004) determined the source mechanisms of small to moderate earthquakes in southern California using synthetic waveforms calculated with the spectral-element method. Because the derivatives of the source parameters are determined numerically by differentiating synthetics with respect to the source parameters, up to 10 forward simulations are needed for each earthquake (6 moment tensor components, latitude, longitude, depth, and the reference location). When the reference location is far from the

true location, the derivatives of the location parameters may not adequately reflect the non-linear variation of waveforms as a function of location. Taking advantage of the source-receiver reciprocity, Zhao et al. (2006) introduced the use of strain Green's tensor in source inversion based on 3D reference models. We extend the SGT-database approach to regional and teleseismic scales, so we are able to use any combination of local and teleseismic waveforms in source inversion (Shen et al., 2009). We fit filtered and time-shifted waveforms directly. For a given source location, the waveforms are linear functions of the moment tensor elements, which can be solved as a linear inverse problem. To account for perturbations in earthquake source location, we carry out a grid search in the vicinity of the reference location.

Figure 3 shows the selected earthquakes in the southeast Tibetan plateau and the stations used in moment tensor inversion (Shen et al., 2009). Wave simulations are carried out at three scales (local/near regional, far regional, and teleseismic), resulting in three FD-SGT databases, one for each wave simulation level. An updated crust and upper mantle model (CUB 2.0, Shapiro & Ritzwoller, 2002) is used as the 3D reference model. The FD-SGT moment tensors agree well the global centroid moment tensor (GCMT) solutions (Fig. 4), with one notable exception at the eastern Himalayan syntaxis (event 03.230 in Figure 4). The GCMT solution shows a strike-slip event at 33 km depth, while our FDSGT solution is a shallow ( $2 \pm 16$  km) thrust event. Figure 5 shows an example of the fit between the observed waveforms and the synthetics calculated from the FD-SGT databases. The regional stations, the 3D model and shorter-period body waves than in the GCMT solutions tend to provide tighter constraints on the source location, particularly the depth. The lowest magnitude of the earthquakes in Figure 4 is Mw 4.35, though the method is applicable to smaller earthquakes. The SGT approach is most effective when the model predicts significantly better waveform fit than 1D models. As the crust and mantle velocity model improves, one may extend the useful surface waves to shorter periods and be able to determine the moment tensors of lower magnitude earthquakes.

### **3.4. Sensitivity Kernels Based on 3D Reference Model and Full Wave Tomography**

In recent years, seismologists have started to replace the great-circle path of a surface wave with sensitivity kernels having a finite width and symmetrically distributed across the great-circle path (e.g., Yoshizawa and Kennett, 2002; Ritzwoller et al., 2002a) or a more physically realistic kernel calculated using 1D (e.g., Li and Romanowicz, 1996; Zhou et al., 2004, 2006) or 3D (e.g., Liu and Tromp, 2006; Zhang et al., 2007) reference models. Similarly, several studies (e.g., Hung et al., 2004; Chen et al., 2007b; Sigloch et al., 2008) have replaced body-wave ray paths with “banana-doughnut” sensitivities calculated in 1D (e.g., Dahlen et al., 2000) or 3D (e.g., Tromp et al., 2005; Zhao et al., 2005; Liu and Tromp, 2006; Zhang et al., 2007) models.

To date the inversions of P- and S-wave speeds have been carried out separately under the assumption that P traveltimes are affected only by the P-wave speed of the elastic media and S traveltimes by the S-wave speed. The practice may stem from ray theory, in which P and S waves are completely decoupled except for conversions at discontinuities. Based upon numerical and analytical solutions, we have shown that for

finite-frequency waves, S-speed perturbation may have significant effects on P waveforms (Zhang and Shen, 2008). At places near the source or receiver, the cross-dependence of P waveforms on S-speed perturbation is substantial (Figure 6). For example, the integrated absolute P-traveltime sensitivity to S-speed perturbation is 31% of that to P-speed perturbation when the source-receiver distance is seven times the wavelength ( $L/\lambda=7$ , where  $\lambda$  is the wavelength and  $L$  the distance to the receiver). At a source-receiver distance of 100 wavelengths, the ratio is about 5%. This finite-frequency effect has important implications for seismic tomography, particularly at regional and local scales, where target structures are often located within several tens of wavelengths from receivers or from both sources and receivers. Even for regions far from sources and receivers, neglecting this cross-dependence means that the estimates of the P speed near the source and receiver are likely biased and such errors may propagate into the rest of the model in tomographic inversion.

Figure 7 shows the phase sensitivities of a regional Rayleigh wave to S- and P-wave speeds. Similar to the results for southern California in Liu and Tromp (2006), there are large 3D variations in the finite-frequency kernels due to wave-speed variations. Although commonly neglected in surface wave tomography, P-wave speed affects Rayleigh waves (also see Zhou et al. (2004) and Liu and Tromp (2006)). The maximum sensitivity to P-wave speed is on the surface and at a level comparable to the  $V_s$  kernel. It decreases to  $\sim 10\%$  of the maximum at depth of  $\sim \lambda/4$ . Since the peak of the  $V_s$  sensitivity is at the depth of  $\sim \lambda/3$  and heterogeneities in the mantle are generally much weaker than in the crust, it may be necessary to include the sensitivities to P-speed and density for long-period ( $\sim 50+$  s) Rayleigh waves in a high-resolution inversion. When integrated with P/Pn, Rayleigh waves may provide additional constraints on the P-wave structure in the crust. At the very least, incorporating the effects of P-speed on Rayleigh waves may minimize a likely cause contributing to the apparent Love-Rayleigh discrepancy and radial anisotropy.

Figure 8 shows the P wave velocity model of the southeast Tibetan plateau in the shallow (8 km) crust. The model is derived from a joint inversion of  $\sim 10,000$  measurements of phase anomalies of P/Pn, S/Sn and Rayleigh/Love waves in three frequency bands ranging from 0.008-0.1 Hz. After two iterations, the combined velocity anomalies relative to the initial reference model (CUB 2.0, Shapiro and Ritzwoller, 2002) show that the observations require a band of velocity increase just north of the Indus Yalu suture. Another band of high velocity anomalies is located at longitude  $\sim 102^\circ\text{E}$ . These high-velocity anomalies correlate well with areas of granitic and/or more metamorphosed Proterozoic rocks among the regional Mesozoic background (Geological map of the Tibetan plateau, China Academy of Geological Sciences, Chengdu). Compared to previous models and tomography of similar scales, the unprecedented P-wave resolution at such a shallow depth is attributed in part to the sensitivity of Rayleigh waves to P wave speed perturbations.

### 3. DISCUSSION AND CONCLUSIONS

We have systematically developed a finite-difference method to accurately and efficiently simulate seismic wave propagation at local to regional scales. The non-

staggered-grid finite-difference code in the spherical coordinate system is well suited for regional and global wave propagation, while the finite-difference method with boundary-conforming grids that follow topography provides higher accuracy at local and near regional scales. The CFS ADE-PML implementation of the Perfectly Matched Layer makes it possible to use a relatively small number of boundary layers to efficiently absorb waves incident at a near-grazing angle, low frequency waves and evanescent waves.

The local- and global-scale finite-difference methods make it possible to construct hierarchical FD-SGT databases with great flexibility. These SGT databases can be used to invert for the source moment tensors and locations, a highly nonlinear problem, in a global-minimum-misfit search. Because the SGT databases are pre-calculated, the inversion of the source parameters does not involve forward wave simulations “on the fly” and thus can be carried out in real time or near real time.

The full-wave tomography method provides an accurate way to integrate body- and surface-wave observations in a self-consistent way via 3D sensitivity kernels. Our ability to update the 3D models means we can linearize the tomographic problem by progressively determining heterogeneities at various scales from broad and smooth features to small-scale, large and sharp variations. For earthquake tomography, the rate of convergence depends on the initial reference model, since it affects the source moment tensor solutions, and thus measurements of the differences between the observed and synthetic waveforms (e.g., traveltimes). One possible strategy to deal with this nonlinear problem is to use Empirical Green’s Functions (EGFs) extracted from ambient noise to obtain a robust model for the crust and shallow upper mantle before the inversion for the earthquake source moment tensors and subsequent earthquake tomography. Because EGFs are dominated by fundamental-mode Rayleigh and Love waves, they can be used in the same way in full-wave tomography as earthquake Rayleigh and Love waves.

## **4. RECOMMENDATIONS**

An increasing number of seismologists have appreciated the advantages of the full-wave approach based on 3D reference models although only a few groups have actually used it to date. This is partly due to the fact that the method requires the use of high-performance supercomputers. One promising area of developments in computational technology is the use of clusters constructed with Graphic Processing Units (GPU), which can improve finite-difference simulations by a factor of 10 to 30 compared to CPU-based clusters (Abdelkhalek et al., 2009). So a well-adapted computation code on a moderate (\$100K) GPU cluster can be as powerful as a million-dollar CPU cluster. The porting of finite-difference codes to GPU clusters should be relatively straightforward and inexpensive. This will significantly lower the costs of computational resources needed to do full-wave source moment tensor and tomography inversion.

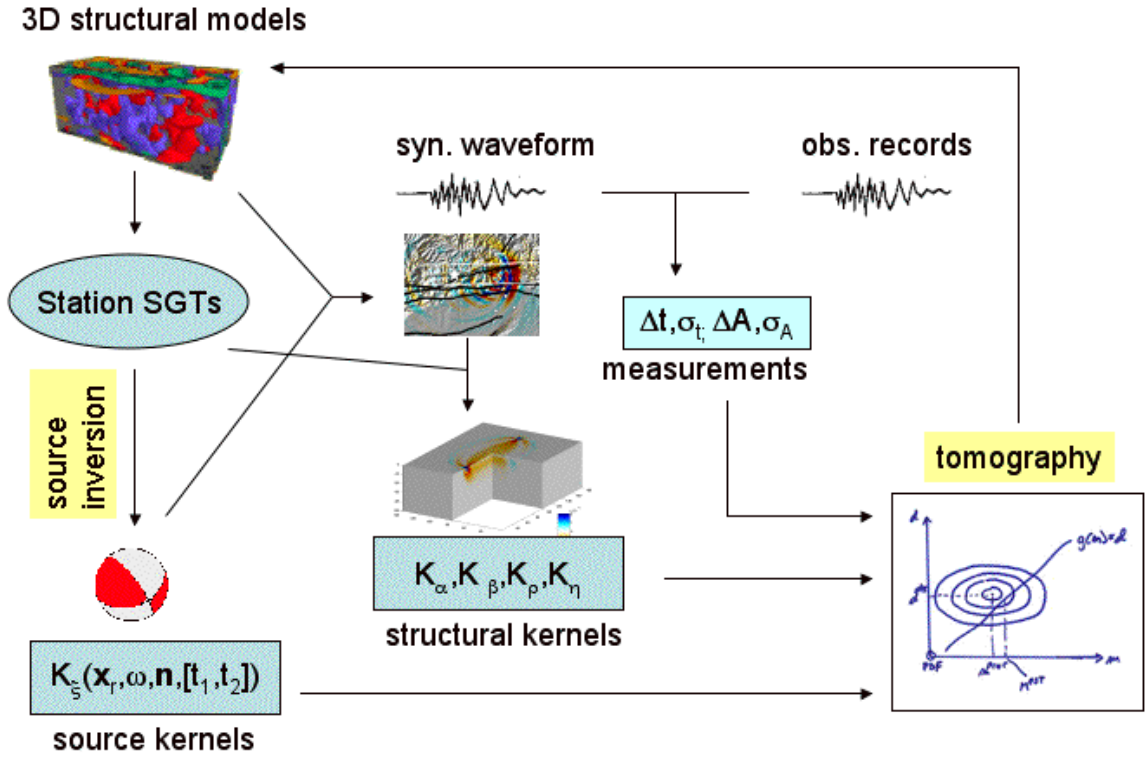


Figure 2 Schematic illustration of the unified tomography and moment tensor inversions based on 3D FD-SGT databases.



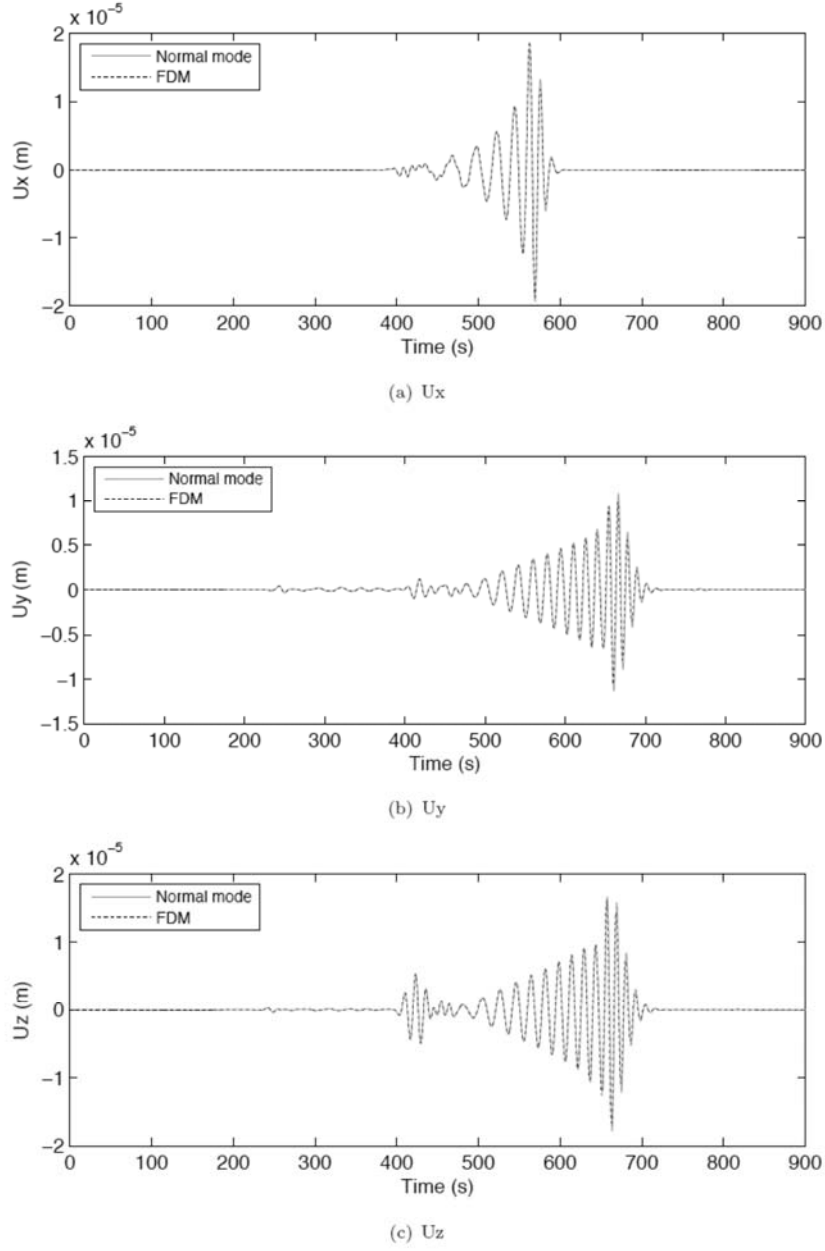


Figure 3 Comparisons between the 3-component synthetics calculated by the spherical finite-difference algorithm (dashed line) and normal-mode summation (solid line). The double couple source with the strike, dip and rake of  $45^\circ$ ,  $45^\circ$  and  $90^\circ$ , respectively, is located at  $(0^\circ\text{N}, 3^\circ\text{E})$ . The receiver is at  $(0^\circ\text{N}, 18^\circ\text{E})$  on the surface,  $15^\circ$  east of the source. The fit of the two solutions is excellent, verifying the accuracy of the finite-difference calculation.

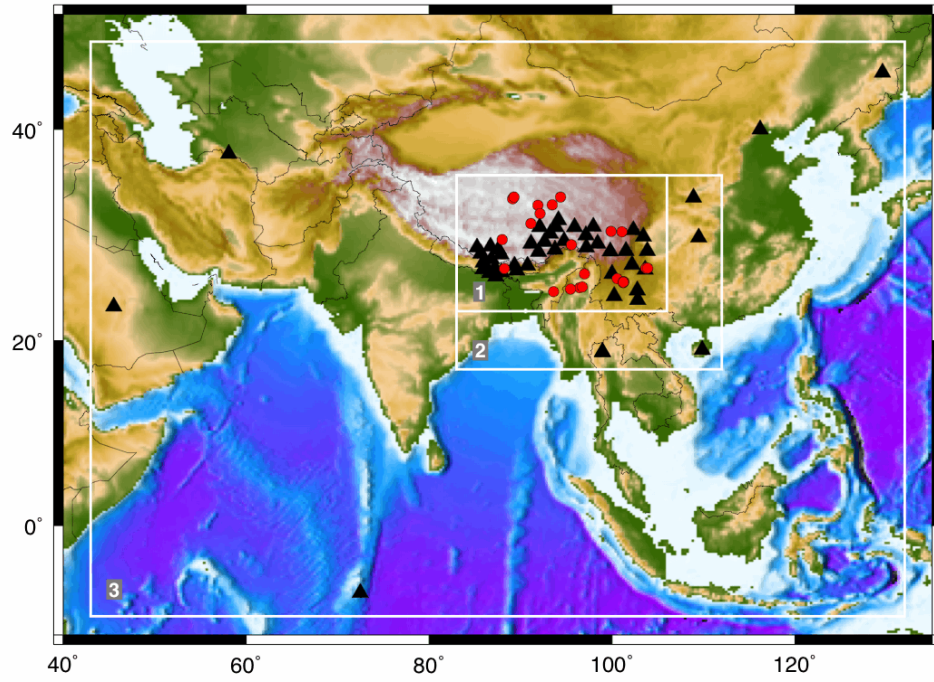


Figure 4 Selected earthquakes (dots) in the southeast Tibetan plateau during 2001-2004 and the stations (triangles) used in moment tensor inversions. White rectangles outline the three geographic scales of finite-difference wave simulation (1) local/near regional, (2) far-regional, and (3) teleseismic. Shen et al. (2009).

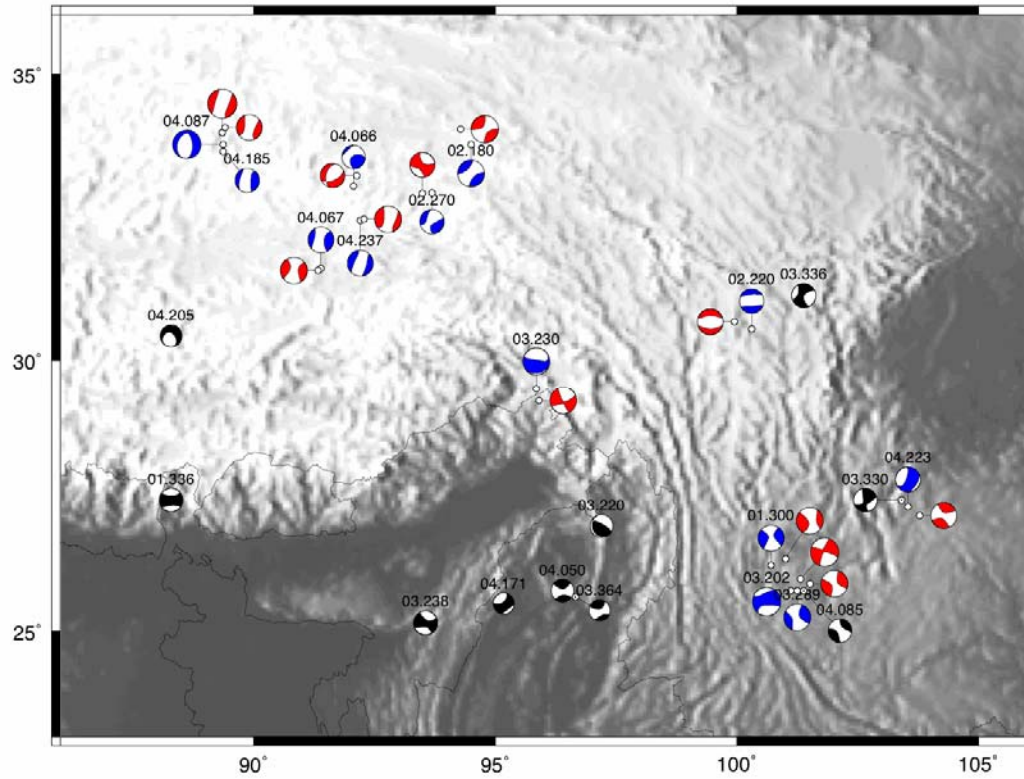


Figure 5 Comparison of the FD-SGT (white-and-blue symbols) and GCMT (white-and-red symbols) solutions for 13 earthquakes during 2001-2004 in the southeast Tibetan plateau. The numbers above the FDSGT solution denote the year and Julian day of the earthquake. Also plotted are the source mechanisms of 10 additional earthquakes without GCMT solutions (black-and-white symbols).

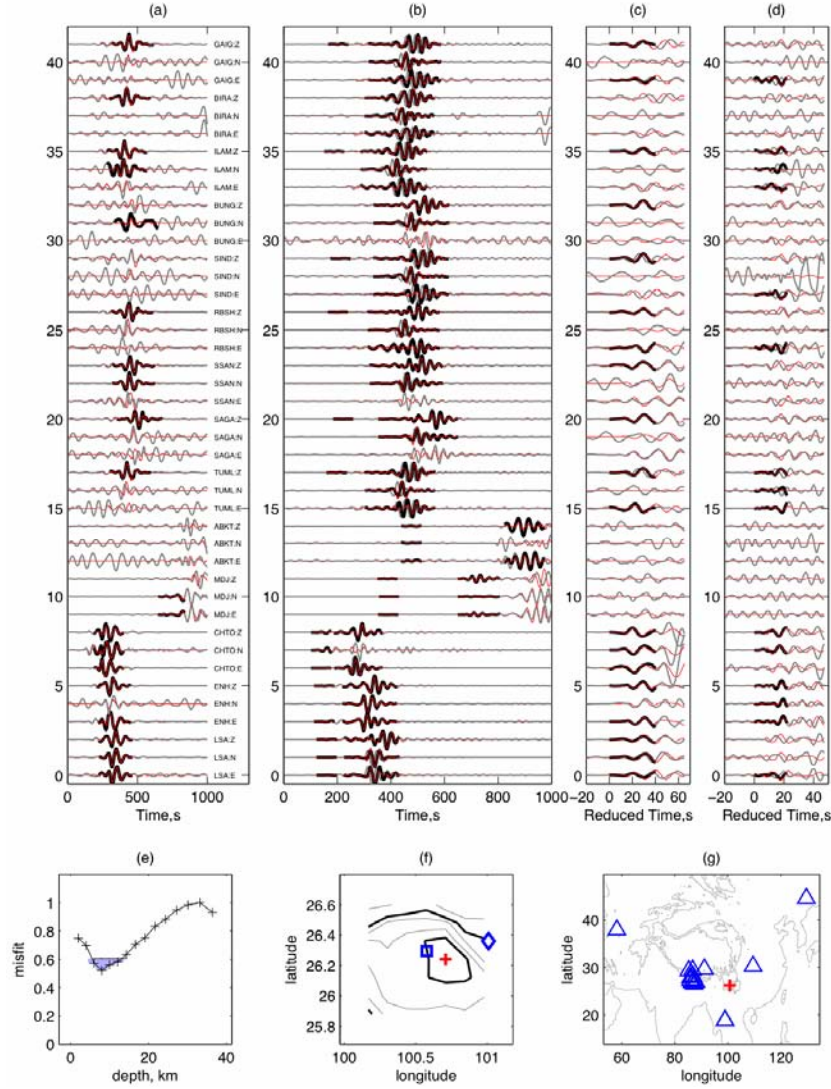


Figure 6 (a-d) Observed waveforms (thick gray lines) for event 01.300 of Figure 4 are compared with the synthetics for the best source moment tensor solution (red lines). The frequency bands are, from left to right, 0.00833-0.0167, 0.0167-0.0333, 0.0333-0.0667, and 0.0667-0.167 Hz. Dark thick lines are time-shifted observed waveforms used in the final inversion. For the first arrivals (in c and d), the time is reduced to align the arrivals within the time window. The amplitude is normalized by individual trace. (e) Normalized waveform misfit as a function of depth. Crosses mark the grid-search depths. The shaded region indicates the 1- $\sigma$  confidence limit. (f) Contours of various confidence limits at the depth of the global best solution (8 km for this event). The cross marks the FDSGT location, the square the EHB location (E.R. Engdahl, per. comm.), and the diamond the global centroid moment tensor location. From the innermost contour surrounding the FDSGT solution, the contours are the 68% (dark line), 80%, 90%, 95% (dark line), and 99% confidence limits. (g) Triangles and cross mark the stations used in the source inversion and the event, respectively. Gray contours follow 0, 2000 and 4000 m elevation. Shen et al. (2009).

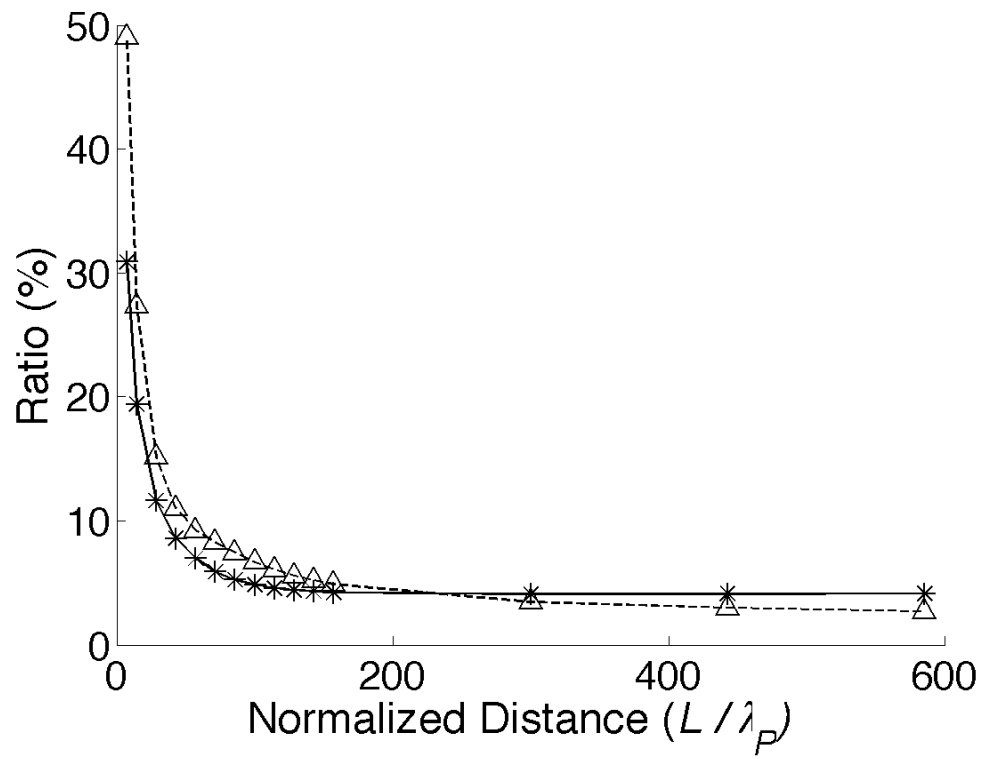


Figure 7 The relative magnitudes of the integrated absolute P traveltimes (asterisk) and amplitude (triangle) sensitivities to S- and P-speed perturbations vary with the normalized distance between the source and receiver. From Zhang and Shen (2008).

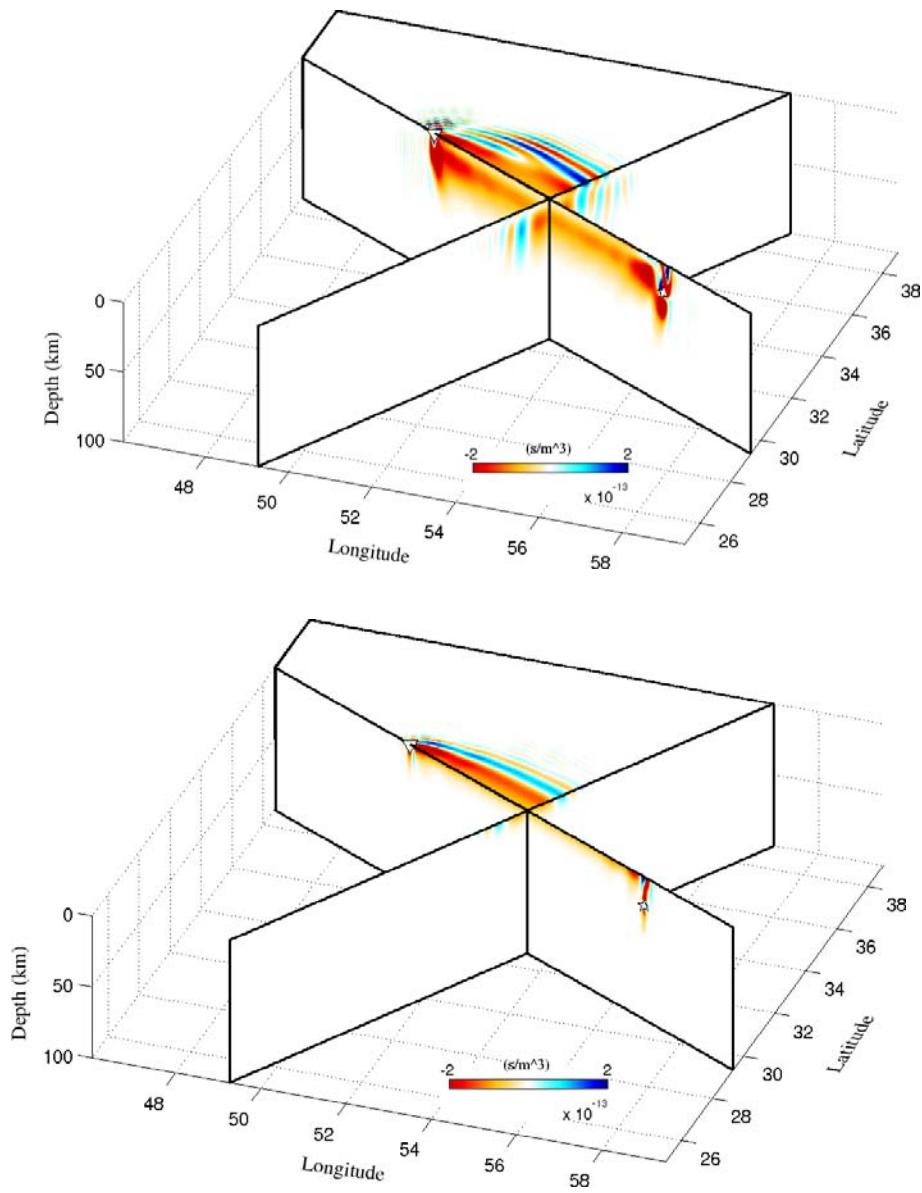


Figure 8 Phase sensitivity kernels of a regional Rayleigh wave to S wave-speed (Top) and P wave-speed (Bottom) perturbations relative to a 3D reference model. The period of the wave is 10-20 s. The two vertical cross-sections cut the model along the great circle path between the earthquake source (in the southeast corner of the model) and receiver (in the northwest corner of the model) and perpendicular to the great circle. Also shown is a quadrant of a horizontal section on the surface. The scale is  $\pm 2 \times 10^{-13} \text{ s/m}^3$  for both S and P wave speed.



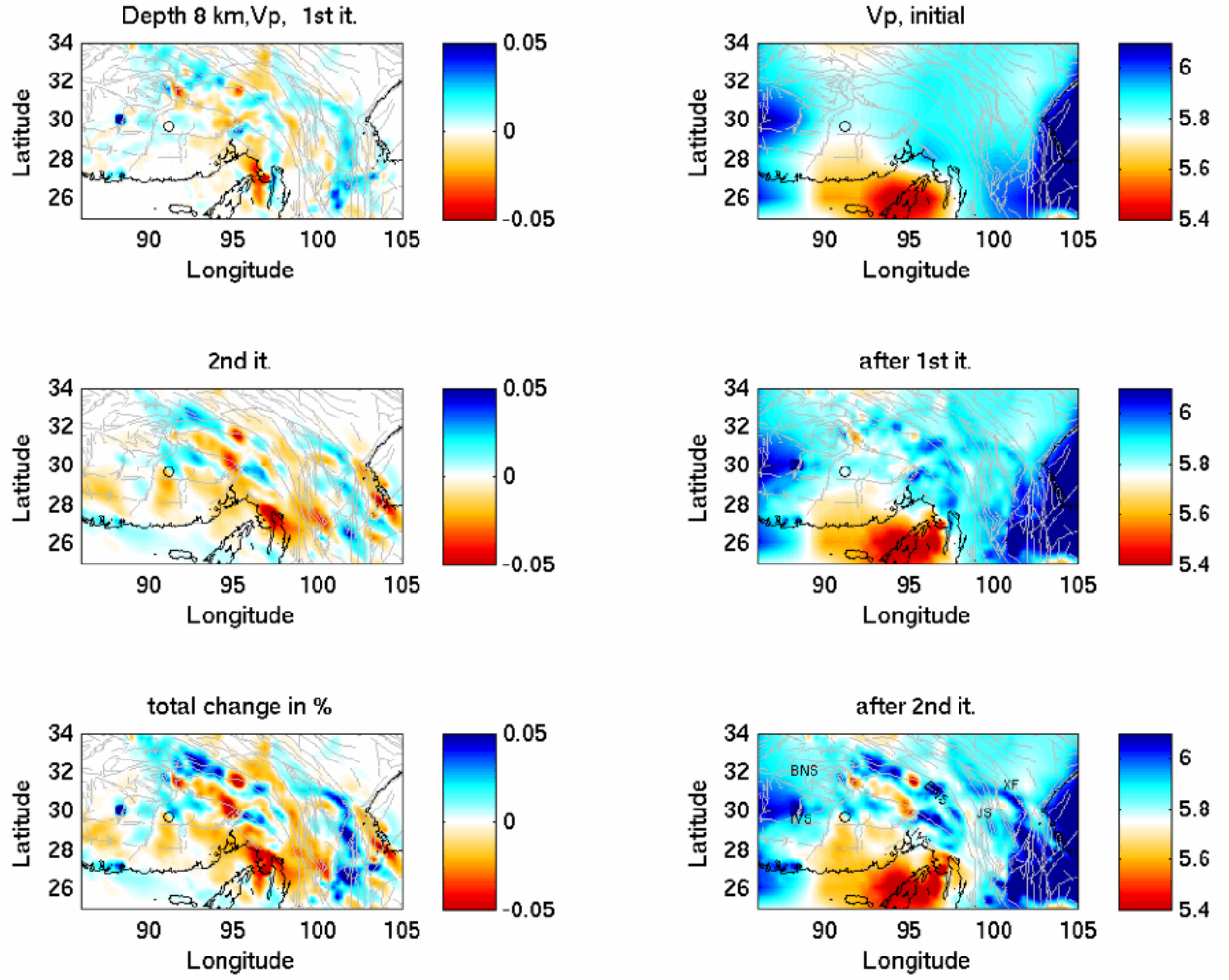


Figure 9 P wave velocity variations at 8 km depth in the southeast Tibetan plateau. The initial 3D reference model (top right) is converted from CUB 2.0 by a  $V_p/V_s$  ratio of 1.74 in the crust. The unit of the color bar is km/s. The left panels show the velocity perturbations after the 1<sup>st</sup> and 2<sup>nd</sup> iteration and the total velocity change in percent. The middle-right and bottom-right panels shows the updated models after the 1<sup>st</sup> and 2<sup>nd</sup> iterations. The high-velocity anomalies north of the Indus-Yalu suture (IYS) and Bangong-Nujiang suture (BNS) and along the Xianshuihei Fault system (XF) are correlated with areas of granitic and/or older and more metamorphosed Proterozoic rocks.

## REFERENCES

- Abdelkhalek, R., H. Calandra, O. Coulaud, G. Latu, J. Roman, Fast seismic modeling and reverse time migration on a GPU cluster, The 2009 High Performance Computing and Simulation – HPCS’09 (<http://hal.inria.fr/docs/00/40/39/33/PDF/hpcs.pdf>), 2009.
- Bassin C, Laske G, Masters G. The current limits of resolution for surface wave tomography in North America, *Eos Trans AGU*, 81, F897, 2000.
- Chen, P., T.H. Jordan, and L. Zhao, Full three-dimensional tomography: a comparison between the scattering-integral and adjoint-wavefield methods, *Geophys. J. Int.*, 170, 175-181, 2007a.
- Chen, P., L. Zhao, and T.H. Jordan, Full 3D tomography for crustal structure of the Los Angeles Region, *Bull. Seismol. Soc. Am.*, 97 (4), 1094-1120, doi: 10.1785/0120060222, 2007b.
- Dalen, F., S. Hung, and G. Nolet, Frechet kernels for finite-frequency travel times- I. Theory, *Geophys. J. Int.*, 157-174, 2000.
- Hung, S, and D. Forsyth, Modeling anisotropic wave propagation in oceanic inhomogeneous structures using the parallel multidomain pseudo-spectral method, *Geophys. J. Int.*, 726-740, 1998.
- Hung, S., Y. Shen, and L. Chiao, Imagining seismic velocity structure beneath the Iceland hotspot- a finite-frequency approach, *J. Geophys. Res.*, 109, B08305, doi:10.1029/2003JB002889, 2004.
- Hixon, R., On increasing the accuracy of MacCormack schemes for aeroacoustic applications, *AIAA Paper*, 97-1586, 1997.
- Igel, H., T. Nissen-Meyer, G. Jahnke, Wave propagation in 3D spherical sections: effects of subduction zones, *Phys. Earth Planet. Inter.*, 132, 219-234, 2002.
- Komatitsch, D., J. Ritsema, and J. Tromp, The spectral-element method, Beowulf computing, and global seismology, *Science* 298, 1737-1742, 2002.
- Li, X., and B. Romanowicz, Global mantle shear velocity model developed using nonlinear asymptotic coupling theory, *J. Geophys. Res.*, 101, 22,245-22,272, 1996.
- Liu, Q., Polet, J., Komatitsch, D., & Tromp, J., Spectral-element moment tensor inversions for earthquakes in southern California, *Bull. Seism. Soc. Am.*, 94, 1748-1761, 2004.
- Liu, Q., and J. Tromp, Finite-frequency kernels based on adjoint methods, *Bull. Seismol. Soc. Am.* 96, 2383-2397, 2006.
- Moczo, P, J.O.A. Rotertsson, L. Eisner, The finite-difference time-domain method for modeling of seismic wave propagation, *Advances in Geophysics*, 48, 421-516, 2007.
- Olsen, K.B., Simulation of three-dimensional wave propagation in the Salt Lake Basin, Ph.D. Thesis, University of Utah, Salt Lake City, Utah, 157p, 1994.
- Ritzwoller, M.H., NM. Shapiro, M.P. Barmin, and A.L. Levshin, Global surface wave diffraction tomography, *J. Geophys. Res.*, 107, DOI: 10.1029/2002JB001777, 2002.
- Shapiro, N.M. & Ritzwoller, M.H., Monte-Carlo inversion for a global shear velocity model of the crust and upper mantle, *Geophys. J. Int.*, 151, 88-105, 2002.
- Shen, Y., Z. Zhang, W. Zhang, Moment inversions of earthquakes in the southeast Tibetan plateau using finite-difference strain Green tensor database, submitted to *Geophys. J. Int.*, 2009.



- Shen, Y., Z. Zhang, L. Zhao, Component-dependent Frechet sensitivity kernels and utility of three-component seismic records, *Bull. Seism. Soc. Am.*, 98 (5), 2517-2525, doi:10.1785/0120070283, 2008a.
- Shen, Y., W. Zhang, Y. Ren, and X. Liang, Imaging the crust and upper mantle in the southern and southeastern Tibetan plateau: A three-dimensional full-wavefield approach, *Eos Trans. AGU*, 89(53), Fall Meet. Suppl., abstract T11E-06 Invited, 2008b.
- Sigloch, K., N. McQuarrie, G. Nolet, Two-stage subduction history under North America inferred from multiple-frequency tomography, *Nature Geosci.*, 1, 458-462, 2008.
- Tromp, J, D. Komatitsch, Q. Liu, C. Tape, A. Maggi, Imaging Earth's interior based upon adjoint method, *Eos Trans. AGU*, 89(53), Fall Meet. Suppl., Abstract DI21A-1730, 2008.
- Tromp, J., C. Tape, and Q. Liu, Seismic tomography, adjoint methods, time reversal and banana-doughnut kernels, *Geophys. J. Int.*, 160, 195-216, 2005.
- Van der Lee, S., and A. Frederiksen, Surface wave tomography applied to the north American upper mantle, in *Seismic Earth: Array Analysis of Broadband Seismograms*, *Geophys. Monograph Ser.* 157, AGU, pp. 67-80, 2005.
- Yoshizawa, K., and B.L.N. Kennett, Determination of the influence zone for surface wave paths, *Geophys. J. Int.* 149, 440-453, 2002.
- Zhang W, Chen X. Traction image method for irregular free surface boundaries in finite difference seismic wave simulation, *Geophys. J. Int.* 167, 337-353, 2006.
- Zhang, W., Y. Shen, Unsplit Complex Frequency Shifted PML Implementation Using Auxiliary Differential Equation for Seismic Wave Modeling, submitted to *Geophysics*, 2009.
- Zhang, W., Y. Shen, X. Chen, Numerical simulation of strong ground motion for the Ms8.0 Wenchuan earthquake of 12 May 2008, *Sci. China Ser. D-Earth Sci.*, 51, 1673-1682, 2008 (a pdf copy is available at <http://seismolab.gso.uri.edu/pub.html>).
- Zhang, W., Y. Shen, L. Zhao, 3D velocity-stress seismic wave modeling in spherical coordinate by a non-staggered finite difference method, manuscript in preparation, 2010.
- Zhang, Z., Y. Shen, Cross-dependence of finite-frequency compressional waveforms to shear seismic wave-speeds, *Geophys. J. Int.*, 174, 941-948, doi:10.1111/j.1365-246X.2008.03840.x, 2008.
- Zhang, Z., Y. Shen, W. Zhang, Full-wave finite-frequency tomography of the southeast Tibetan plateau, American Geophysical Union Fall Meeting (abstract S31D-08), 2009.
- Zhang, Z., Y. Shen, and L. Zhao, Finite-frequency sensitivity kernels for head waves, *Geophys. J. Int.* 171, 847-856, 2007.
- Zhao, L., Chen, P. & Jordan, T. H. Strain Green tensor, reciprocity, and their applications to seismic source and structure studies, *Bull. Seism. Soc. Am.*, 96, 1753-1763, doi:10.1785/0120050253, 2006.
- Zhao, L. & Helmberger, D.V., Source estimation from broadband regional seismograms, *Bull. Seism. Soc. Am.*, 84, 91-104, 1994.
- Zhao, L., T.H. Jordan, K.B. Olsen, and P. Chen, Fréchet kernels for imaging regional earth structure based on three-dimensional reference models, *Bull. Seism. Soc. Am.* 95, 2066-2080, 2005.

- Zhou, Y., F.A.Dahlen, and G. Nolet, 3-D sensitivity kernels for surface-wave observables, *Geophysical Journal International*, 158, 142-168, 2004.
- Zhou, Y., G. Nolet, F. A. Dahlen, and G. Laske, Global upper-mantle structure from finite-frequency surface-wave tomography" *Journal of Geophysical Research*, 111, B04304, doi:10.1029/2005JB003677, 2006.
- Zhu, L. & Helmberger, D.V., Advancement in source estimation techniques using broadband regional seismograms, *Bull. Seism. Soc. Am.*, 86, 1634-1641, 1996.

## **LIST OF SYMBOLS, ABBREVIATIONS, AND ACRONYMS**

AFRL	Air Force Research Laboratory
AW	Adjoint wavefield
CFS ADE-PML	Complex Frequency-Shifted Perfectly Matched Layer
EGF	Empirical Green's Functions
EHB	Engdahl-van der Hilst-Buland
FD-SGT	Finite-Difference Strain Green Tensor
GCMT	Global Centroid Moment Sensor
PML	Perfectly Matched Layer
SGT	Strain Green Tensor
SI	Scattering Integral

# APPENDIX A



**Unsplit Complex Frequency Shifted  
PML Implementation Using Auxiliary Differential Equation  
for Seismic Wave Modeling (resubmission of GEO-2009-  
0179)**

Journal:	<i>Geophysics</i>
Manuscript ID:	Draft
Manuscript Type:	Technical Paper
Date Submitted by the Author:	
Complete List of Authors:	Zhang, Wei; University of Rhode Island, Graduate School of Oceanography Shen, Yang; University of Rhode Island, Graduate School of Oceanography
Keywords:	finite difference, modeling, wave propagation, boundary conditions
Area of Expertise:	Seismic Modeling and Wave Propagation



**Unsplit Complex Frequency Shifted PML Implementation Using  
Auxiliary Differential Equation for Seismic Wave Modeling**

**Wei Zhang\* and Yang Shen†**

*\*Graduate School of Oceanography,*

*The University of Rhode Island,*

*Narragansett, RI 02882*

*e-mail: wzhang@gso.uri.edu*

*†Graduate School of Oceanography,*

*The University of Rhode Island,*

*Narragansett, RI 02882*

*e-mail: yshen@gso.uri.edu*

(December 10, 2009)

Running head: **ADE CFS-PML for Seismic Wave Modeling**

**ABSTRACT**

The complex frequency-shifted PML (CFS-PML) is more efficient than the standard PML to absorb low-frequency waves, evanescent waves and near-grazing incident waves. In seismic wave modeling, the CFS-PML has been implemented by the first-order-accuracy convolutional PML (CPML) technique or second-order-accuracy recursive convolution PML (RIPML) technique. Both involve an algorithm different from the numerical scheme used in the interior domain to update the auxiliary memory variables and thus can not be directly used in higher-order time marching schemes. In this paper, we introduce an alternative unsplit-field CFS-PML implementation using auxiliary differential equations (ADE) to update the auxiliary memory variables. This ADE CFS-PML im-

plementation results in complete first-order differential equations for both the wavefield components and the auxiliary memory variables. Thus the same numerical scheme used in the interior domain can be used to solve the ADE CFS-PML equations. We implement the ADE CFS-PML in both the FDTD method and a nonstaggered-grid MacCormack DRP/opt finite-difference method with the 4th-order Runge-Kutta scheme to demonstrate its straightforward implementation in different numerical time marching schemes. We perform a series numerical tests to investigate the optimal values of the CFS-PML parameters in seismic wave modeling and show that the scaling factor  $\beta$  transforms the PML to a transversely isotropic material. For normal incident waves,  $\beta$  only delays wave propagation but does not increase damping. For oblique incident waves, it bends the wavefront towards the normal direction of the PML layer, thus increases damping. Theoretically, a larger  $\beta$  can bend the wavefront more efficiently, but a very large  $\beta$  may cause strong spurious reflections if it causes the wavelength to be much shorter than what the numerical scheme can resolve. Our numerical tests indicate that the optimal  $\beta$  reduces the points per dominant wavelength at the outermost boundary to three, around half the value required by the numerical scheme.

At the free surface, the PML equations should be derived taking the free surface boundary condition into account in finite-difference methods. Otherwise, the free surface in the PML Layer will cause instability in the nonstaggered-grid finite-difference scheme or ineffective absorption of surface waves when the free surface coincides with the normal stress components in the staggered-grid finite-difference scheme.

Our numerical test of a two-layered medium with surface topography in a narrow vertical slice indicates that we can use a narrow slice mesh with the ADE CFS-PML to efficiently simulate full wave propagation in complex structure models.

INTRODUCTION

Numerical study of seismic wave propagation usually needs to simulate waves propagating in an unbounded space. However, numerical simulation is often implemented in a finite computational domain in practice. Thus some special treatments are needed at the computational boundaries to absorb waves propagating outward. Techniques based on two concepts are commonly used, one is called Absorbing Boundary Conditions (ABCs), which impose a proper boundary condition at the outermost boundaries to satisfy the condition that waves only propagate outward (Clayton and Engquist, 1977; Higdon, 1986, 1990; Randall, 1988; Liao et al., 1984; Bayliss et al., 1986), the other can be grouped into Absorbing Boundary Layers (ABLs, or sponge layers), which use finite layers to gradually damp wave amplitude, so using the Dirichlet boundary condition at the outermost boundary does not generate a strong reflection (Cerjan et al., 1985; Sochacki et al., 1987). Strengths and shortcomings of each group can be found in Festa and Vilotte (2005) and Komatitsch and Martin (2007). Perfectly matched layer (PML) (Bérenger, 1994), one of the ABLs techniques, is proven to effectively absorb waves at a wide range of incident angles with only several to tens layers and has become widely used in elastic wave modeling (Chew and Liu, 1996; Hastings et al., 1996; Collino and Tsogka, 2001; Marcinkovich and Olsen, 2003; Wang and Tang, 2003).

The original PML in Bérenger (1994) (we refer to this version as the standard PML in this paper) adopted a non-physical splitting of the wave field components and equations, which leads to two different sets of equations for the interior domain and the PML layer, and thus are not trivial to incorporate into an existing numerical modeling code. Furthermore, the split-field PML is mathematically weakly well-posed (Abarbanel and Gottlieb, 1997). Alternative interpretations of the PML as an artificial anisotropic medium (Sacks et al., 1995; Gedney, 1996), or complex coordinate stretching (Chew and Weedon, 1994; Teixeira and Chew, 2000) led to unsplit-field PML implemen-



tations involving convolution terms (Wang and Tang, 2003; Komatitsch and Martin, 2007), integral terms (Zeng and Liu, 2004; Drossaert and Giannopoulos, 2007b), or auxiliary differential equations (Ramadan, 2003). Hagstrom (2003) introduced a modified modal solution technique to derive PML equations and was used by Appelö and Kreiss (2006) in 2D elastic wave modeling. This technique can provide a stable PML implementation by choosing the parameters satisfying the geometric relations in anisotropic media (Bécache et al., 2003). Recently, Meza-Fajardo and Papageorgiou (2008) showed that stable result can be obtained in anisotropic media using a 3D damping profile in the PML based on the concept of complex coordinate stretching.

Though the standard PML has been widely used in seismic wave modeling, it can generate large spurious reflections for near-grazing incident waves, low frequency waves or evanescent waves (Festa and Vilotte, 2005; Komatitsch and Martin, 2007; Drossaert and Giannopoulos, 2007a). The complex frequency shifted PML (CFS-PML) (Kuzuoglu and Mittra, 1996) is more efficient in such circumstances using a frequency dependent damping (Festa and Vilotte, 2005; Festa et al., 2005; Komatitsch and Martin, 2007; Drossaert and Giannopoulos, 2007b,a). The CFS-PML was originally implemented in a split-field form and three auxiliary memory variables are needed for each derivative (Gedney, 1998). Roden and Gedney (2000) derived an unsplit-field CFS Convolutional-PML (C-PML) equation involving a convolution term that can be efficiently calculated using a recursive convolution algorithm (Luebbers and Hunsberger, 1992). This technique has been used in seismic wave modeling in elastic media (Komatitsch and Martin, 2007; Drossaert and Giannopoulos, 2007a) and poroelastic media (Martin et al., 2008a). Drossaert and Giannopoulos (2007b) derived an alternative CFS-PML implementation that involves integral terms, which can be calculated by a recursive integration algorithm. The recursive integration in C-PML is of first-order accuracy (Giannopoulos, 2008), and the trapezoidal rule in RIPML is of second-order accuracy (Drossaert and Giannopoulos, 2007b). Both approaches need an algorithm different from the numerical scheme

used in the interior domain to update the auxiliary memory variables and thus can not be directly used with higher-order time marching schemes, such as a 4th-order Runge-Kutta scheme used in the nonstaggered finite-difference velocity-stress method (Zhang and Chen, 2006) on a boundary-conforming grid to simulate seismic wave propagation in the presence of surface topography, in which the higher-order multi-stage Runge-Kutta scheme is important to allow a larger time step (Hixon, 1997). In the field of electromagnetic simulation, Ramadan (2003) proposed an unsplit-field implementation of the standard PML using auxiliary differential equations (ADE), and Wang and Liang (2006) extended this approach to the CFS-PML with a 2D alternating direction implicit (ADI) finite-difference time-domain (FDTD) method. This ADE CFS-PML implementation results in complete first-order differential equations for both the wavefield components and the auxiliary memory variables, thus the same numerical scheme used in the interior domain can be used to solve the ADE CFS-PML equations no matter whether a 2nd-order leap-frog scheme or a higher-order Runge-Kutta scheme is used.

In this paper, we implement the ADE CFS-PML in the seismic wave simulation both in the FDTD method and the nonstaggered-grid finite-difference method (Zhang and Chen, 2006) using a 4th-order Runge-Kutta time marching scheme. We derive the ADE CFS-PML equations for the velocity-stress equations. Then we analyze the free surface boundary condition inside the PML layer and modify the PML equations based on the free surface condition to avoid the instability caused by the incompatibility between the PML equations and the free surface boundary condition. We analyze the role of the scaling factor  $\beta$  in the CFS stretching function, which is still not clear in the literature of seismic wave modeling. We perform a series of numerical tests in a thin slab model to validate the ADE CFS-PML implementation and investigate the optimal values of the parameters in the CFS stretching function. We add the free surface to the thin slab model to demonstrate the efficiency of the modified PML equations taking into account the free surface condition in absorbing

surface waves. Finally, we simulate seismic wave propagation in a two-layered medium with surface topography in a narrow vertical slice to demonstrate the implementation of the ADE CFS-PML in the 4th-order Runge-Kutta scheme and its potential effectiveness in seismic exploration.

## VELOCITY-STRESS EQUATION AND FINITE DIFFERENCE NUMERICAL SCHEME

We consider the following velocity-stress formulation of the elastic wave equations for an isotropic medium in the Cartesian coordinate  $(x, y, z)$ ,

$$\mathbf{v}_{,t} = \frac{1}{\rho} \nabla \cdot \sigma, \quad (1)$$

$$\sigma_{,t} = \mathbf{c} : [\nabla \mathbf{v} + (\nabla \mathbf{v})^T], \quad (2)$$

where  $\mathbf{v} = (v_x, v_y, v_z)^T$  is the velocity vector,  $\sigma$  is the stress tensor and the components are  $\sigma_{ij}, i, j \in (x, y, z)$ ,  $\rho$  is the mass density, and  $\mathbf{c}$  is the stiffness tensor. In this paper, a comma followed by  $t, x, y$  and  $z$  in subscript means a derivative with respect to  $t, x, y$  or  $z$ . Equation 1-2 can also be written in a single vector form appropriate for the 4th-order Runge-Kutta scheme,

$$\mathbf{W}_{,t} = \mathbf{A}\mathbf{W}_{,x} + \mathbf{B}\mathbf{W}_{,y} + \mathbf{C}\mathbf{W}_{,z}, \quad (3)$$

where  $\mathbf{W} = (v_x, v_y, v_z, \sigma_{xx}, \sigma_{yy}, \sigma_{zz}, \sigma_{yz}, \sigma_{xz}, \sigma_{xy})$  is the velocity-stress vector,  $\mathbf{A}$ ,  $\mathbf{B}$  and  $\mathbf{C}$  are the coefficient matrices that can be easily derived. Sometimes it is more convenient to discuss the PML implementation in the component form, thus we express the  $v_x$  component of equation 1,

$$\rho v_{x,t} = \sigma_{xx,x} + \sigma_{xy,y} + \sigma_{xz,z}. \quad (4)$$

We use two numerical schemes to solve the above velocity-stress equations, one is the finite-difference time-domain (FDTD) method with a 2nd-order accuracy leap-frog time marching scheme

on a staggered grid (Levander, 1988; Graves, 1996), the other is the nonstaggered-grid finite-difference method with a 4th-order Runge-Kutta time marching scheme on a boundary-conforming grid (Zhang and Chen, 2006). Since PML implementations do not rely on how spatial derivatives are calculated, we only list the time marching schemes here. The 2nd-order leap-frog scheme can be written as

$$\sigma^{n+1/2} = \sigma^{n-1/2} + \Delta t L(\mathbf{v}^n), \quad (5)$$

$$\mathbf{v}^{n+1} = \mathbf{v}^n + \Delta t L(\sigma^{n+1/2}), \quad (6)$$

where superscript  $n - 1/2, n, n + 1/2$  and  $n + 1$  means time level,  $L(\sigma^{n+1/2})$  is the right hand side of the equation 2 evaluated at time level  $n + 1/2$  using an arbitrary order accuracy spacial staggered finite-difference operator,  $L(\mathbf{v}^n)$  is that of the equation 1 at time level  $n$ . The 4th-order Runge-Kutta scheme can be expressed as

$$h^{(1)} = \Delta t L(W^n) \quad (7)$$

$$h^{(2)} = \Delta t L(W^n + \alpha_2 h^{(1)})$$

$$h^{(3)} = \Delta t L(W^n + \alpha_3 h^{(2)})$$

$$h^{(4)} = \Delta t L(W^n + \alpha_4 h^{(3)})$$

$$W^{n+1} = W^n + \beta_1 h^{(1)} + \beta_2 h^{(2)} + \beta_3 h^{(3)} + \beta_4 h^{(4)},$$

where  $\alpha_2 \sim \alpha_4$  and  $\beta_1 \sim \beta_4$  are the coefficients of the 4th-order Runge-Kutta scheme,  $L(W^n)$  means the right hand side of equation 3 calculated for variable  $W^n$  using the spacial operator. Here the DRP/opt MacCormack operator (Hixon, 1997) is used.

## COMPLEX FREQUENCY-SHIFTED PML USING AUXILIARY DIFFERENTIAL EQUATIONS

Each face of a 3D computational grid can be terminated by a PML layer (Figure 1). In this paper, we will discuss the PML at the positive  $x$  face. The PML at the opposite face and along other directions can be derived in a similar way. For simplicity of notations, we also suppose the PML at the positive  $x$  face starts from  $x = 0$ .

Based on the concept of complex coordinate stretching (Chew and Weedon, 1994), the equations inside the PML layer have exactly the same form as that (equations 1-2) in the physical domain except that the coordinate  $x$  is replaced with a complex stretched coordinate  $\tilde{x}$ ,

$$\tilde{x} = \int_0^x s_x(\eta) d\eta, \quad (8)$$

where  $s_x$  is the complex stretching function that determines the characteristics of the PML model.

From relationship,

$$\frac{\partial}{\partial \tilde{x}} = \frac{1}{s_x} \frac{\partial}{\partial x}, \quad (9)$$

one can transform equations in the complex coordinate  $(\tilde{x}, y, z)$  into the Cartesian coordinate  $(x, y, z)$

where the numerical scheme will be used. Using equation 4 as an example, we have

$$i\omega \rho \hat{v}_x = \frac{1}{s_x} \frac{\partial \hat{\sigma}_{xx}}{\partial x} + \frac{\partial \hat{\sigma}_{xy}}{\partial y} + \frac{\partial \hat{\sigma}_{xz}}{\partial z}, \quad (10)$$

where a hat over a quantity denotes the value in the frequency domain. Once  $s_x$  is determined, we can transform this equation into time domain to get the PML equation suitable for time domain numerical methods. The special formulation of  $s_x$  is the key to distinguishing the standard PML, in which

$$s_x(x) = 1 + \frac{d_x(x)}{i\omega}, \quad (11)$$

and the CFS-PML, in which

$$s_x(x) = \beta_x(x) + \frac{d_x(x)}{\alpha_x(x) + i\omega}. \quad (12)$$

In above equations,  $d_x \geq 0$  is the attenuation factor that causes the amplitude of the wavefield to be exponentially reduced inside the PML layer,  $\alpha_x \geq 0$  is the frequency shifted factor that makes the attenuation frequency dependent,  $\beta_x \geq 1$  is the scaling factor, which has been found in numerical tests to be important for absorption of evanescent waves (Liu, 1999; Drossaert and Giannopoulos, 2007a) and near-grazing incident waves (Drossaert and Giannopoulos, 2007b), but the reason has not been theoretically explained in the literature of seismic wave modeling. we will discuss the role of  $\beta_x$  in later sections.  $d_x(x)$ ,  $\alpha_x(x)$ ,  $\beta_x(x)$  and therefore  $s_x(x)$  are all functions of  $x$ . In the following, we omit  $(x)$  for brevity.

The basic idea of the ADE implementation of the CFS-PML is to separate the derivative with respect to the complex coordinate into two parts and only keep  $i\omega$  term in the denominator in one of them,

$$\frac{1}{s_x} = \frac{1}{\beta_x + \frac{d_x}{\alpha_x + i\omega}} = \frac{1}{\beta_x} - \frac{1}{\beta_x} \frac{d_x}{(\alpha_x + i\omega)\beta_x + d_x}. \quad (13)$$

Thus,

$$\frac{1}{s_x} \frac{\partial \hat{\sigma}_{xx}}{\partial x} = \frac{1}{\beta_x} \hat{\sigma}_{xx,x} - \frac{1}{\beta_x} \frac{d_x}{(\alpha_x + i\omega)\beta_x + d_x} \hat{\sigma}_{xx,x}. \quad (14)$$

Defining an auxiliary memory variable  $T_{xx}^x$ ,

$$\hat{T}_{xx}^x = \frac{d_x}{(\alpha_x + i\omega)\beta_x + d_x} \hat{\sigma}_{xx,x}, \quad (15)$$

we can write equation 14 as,

$$\frac{1}{s_x} \frac{\partial \hat{\sigma}_{xx}}{\partial x} = \frac{1}{\beta_x} \hat{\sigma}_{xx,x} - \frac{1}{\beta_x} \hat{T}_{xx}^x, \quad (16)$$

Taking this equation into equation 10, we obtain the unsplit-field CFS-PML equation for the  $v_x$  component in the frequency domain,

$$i\omega\rho\hat{v}_x = \frac{1}{\beta_x}\hat{\sigma}_{xx,x} - \frac{1}{\beta_x}\hat{T}_{xx}^x + \hat{\sigma}_{xy,y} + \hat{\sigma}_{xz,z}, \quad (17)$$

where the memory variable  $T_{xx}^x$  is

$$i\omega\hat{T}_{xx}^x + \left(\alpha_x + \frac{d_x}{\beta_x}\right)\hat{T}_{xx}^x = \frac{d_x}{\beta_x}\hat{\sigma}_{xx,x}. \quad (18)$$

Transforming equations 17 and 18 to the time domain, we get the final ADE CFS-PML equation of  $v_x$  as

$$\rho v_{x,t} = \sigma_{xx,x} + \sigma_{xy,y} + \sigma_{xz,z} + \left[\frac{1}{\beta_x} - 1\right]\sigma_{xx,x} - \frac{1}{\beta_x}T_{xx}^x, \quad (19)$$

and

$$T_{xx,t}^x + \left(\alpha_x + \frac{d_x}{\beta_x}\right)T_{xx}^x = \frac{d_x}{\beta_x}\sigma_{xx,x}. \quad (20)$$

It is worth noting that we write the time domain PML equation as a correction to the original wave equation because it is easy to achieve parallel balance and implement in an existing code (Drossaert and Giannopoulos, 2007a). The ADE CFS-PML equations for axis  $y$  and  $z$  and other components can be obtained in the same manner. The complete ADE CFS-PML equations for the velocity-stress equations are in Appendix A.

Since the velocity-stress equations 1-2 and the ADE CFS-PML equations 19-20 are all first-order partial differential equations with respect to time  $t$ , they can be updated by the same time-stepping scheme. In the staggered 2nd-order leap-frog scheme, equation 20 can be discretized as

$$\frac{T_{xx}^{x|n+1} - T_{xx}^{x|n}}{\Delta t} + \left(\alpha_x + \frac{d_x}{\beta_x}\right)\frac{T_{xx}^{x|n+1} + T_{xx}^{x|n}}{2} = \frac{d_x}{\beta_x}\sigma_{xx,x}^{n+1/2}. \quad (21)$$

Then we can update  $T_{xx}^x$  and  $v_x$  through

$$T_{xx}^{x|n+1} = \frac{2 - \Delta t(\alpha_x + d_x/\beta_x)}{2 + \Delta t(\alpha_x + d_x/\beta_x)}T_{xx}^{x|n} + \frac{2\Delta t d_x/\beta_x}{2 + \Delta t(\alpha_x + d_x/\beta_x)}\sigma_{xx,x}^{n+1/2}, \quad (22)$$

and

$$v_x^{n+1} = v_x^n + \frac{\Delta t}{\rho} \left( \sigma_{xx,x}^{n+1/2} + \sigma_{xy,y}^{n+1/2} + \sigma_{xz,z}^{n+1/2} \right) + \frac{\Delta t}{\rho} \left( \frac{1}{\beta_x} - 1 \right) \sigma_{xx,x}^{n+1/2} - \frac{\Delta t}{\rho} \left( \frac{2}{2 + \Delta t(\alpha_x + d_x/\beta_x)} T_{xx}^{x|n} + \frac{\Delta t d_x/\beta_x}{2 + \Delta t(\alpha_x + d_x/\beta_x)} \sigma_{xx,x}^{n+1/2} \right). \quad (23)$$

The implementation in the 4th-order Runge-Kutta scheme is also straightforward. One can just includes the memory variables in the solution vector  $\mathbf{W}$  in equation 3, then uses the Runge-Kutta scheme (equation 7) to update the PML equations including the memory variable equations.

The computer memory requirement of the ADE CFS-PML is the same as the C-PML (Komatitsch and Martin, 2007) or RIPML (Drossaert and Giannopoulos, 2007b), one memory variable per normal derivative to the PML layer.

## ADE CFS-PML BOUNDARY AND FREE SURFACE BOUNDARY CONDITION

To our knowledge, there is no publication on how to implement the free surface boundary condition in the PML region, which is crucial to efficiently absorb surface waves in the FDTD method or avoid the stability problem in the nonstaggered finite-difference method.

In the physical region, the free surface boundary condition requires the traction to be zero,

$$\mathbf{n} \cdot \boldsymbol{\sigma} = 0, \quad (24)$$

where  $\mathbf{n}$  is the outward normal vector of the free surface. For a flat surface, the zero-traction condition is reduced to a zero-stress condition,

$$\sigma_{zz} = 0, \quad \sigma_{yz} = 0, \quad \sigma_{xz} = 0. \quad (25)$$

In the PML layer, the zero-valued stress components should remain zero at the free surface since the effect of the PML is to exponentially damp the wavefield to zero.



Because the velocity derivatives are related to the stress components through the stress-strain relation (equation 2), the zero-stress condition leads to velocity derivative constraints at the free surface,

$$v_{z,z} = -\frac{\lambda}{\lambda + 2\mu}v_{x,x} - \frac{\lambda}{\lambda + 2\mu}v_{y,y}, \quad (26)$$

$$v_{y,z} = -v_{z,y}, \quad (27)$$

$$v_{x,z} = -v_{z,x}. \quad (28)$$

Taking these equations into the stress-strain relation, the real equations to update  $\sigma_{xx}$  and  $\sigma_{yy}$  at the free surface are

$$\sigma_{xx,t} = (\lambda + 2\mu)v_{x,x} + \lambda v_{y,y} + \lambda \left[ -\frac{\lambda}{\lambda + 2\mu}v_{x,x} - \frac{\lambda}{\lambda + 2\mu}v_{y,y} \right], \quad (29)$$

$$\sigma_{yy,t} = \lambda v_{x,x} + (\lambda + 2\mu)v_{y,y} + \lambda \left[ -\frac{\lambda}{\lambda + 2\mu}v_{x,x} - \frac{\lambda}{\lambda + 2\mu}v_{y,y} \right]. \quad (30)$$

To effectively absorb the surface wave, the ADE CFS-PML equations of  $\sigma_{xx}$  and  $\sigma_{yy}$  at the intersection of the free surface and the PML should be derived from the above equations as

$$\sigma_{xx,t} = \frac{(\lambda + 2\mu)^2 - \lambda^2}{\lambda + 2\mu} \frac{1}{\beta_x} v_{x,x} + \frac{2\lambda\mu}{\lambda + 2\mu} \frac{1}{\beta_y} v_{y,y} - \frac{(\lambda + 2\mu)^2 - \lambda^2}{\lambda + 2\mu} \frac{1}{\beta_x} V_x^x - \frac{2\lambda\mu}{\lambda + 2\mu} \frac{1}{\beta_y} V_y^y, \quad (31)$$

$$\sigma_{yy,t} = \frac{2\lambda\mu}{\lambda + 2\mu} \frac{1}{\beta_x} v_{x,x} + \frac{(\lambda + 2\mu)^2 - \lambda^2}{\lambda + 2\mu} \frac{1}{\beta_y} v_{y,y} - \frac{2\lambda\mu}{\lambda + 2\mu} \frac{1}{\beta_x} V_x^x - \frac{(\lambda + 2\mu)^2 - \lambda^2}{\lambda + 2\mu} \frac{1}{\beta_y} V_y^y, \quad (32)$$

The above equations in the correction form to the PML equations is shown in Appendix A.

In the FDTD method, there are two possible locations for the free surface, coincident with the normal stress components or with the shear stress component  $\sigma_{xz}$  (Gottschammer and Olsen, 2001; Kristek et al., 2002). As the numerical tests presented in the following section show, the above modified ADE CFS-PML equations are crucial to effectively absorb surface waves if the free

surface coincides with the normal stress components. If the free surface coincides with  $\sigma_{xz}$ , the free surface boundary condition is implemented as in the physical domain by setting  $\sigma_{xz}$  and  $\sigma_{yz}$  to zero at the free surface and no special treatment is needed in the PML layer. In the nonstaggered finite-difference method, our numerical tests show that the modified PML equations 31 and 32 are essential for the stability of the solution if the velocity component free surface boundary condition (equation 26) is applied.

### THE ROLE OF THE SCALING FACTOR $\beta$

In the context of electromagnetic wave modeling, Petropoulos (2000) stated that  $\beta_x$  “allows for bending the waves towards the normal direction into the layer by increasing the corresponding component of the wave vector while leaving the tangential component unchanged; at the same time, it increases the damping in the normal direction into the layer” with a stretching function  $s_x = \beta_x(1 + \frac{d_x}{\alpha_x + i\omega})$ . The role of parameter  $\beta_x$  has not been thoroughly understood in seismic wave modeling. For example, a constant  $\beta = 1$  was used in Festa and Vilotte (2005) and Festa et al. (2005).  $\beta$  did not significantly affect the results in Komatitsch and Martin (2007)’s numerical tests, but played an important role in Drossaert and Giannopoulos (2007a,b)’s numerical tests.

To understand the role of  $\beta_x$ , we rewrite the CFS stretching function (equation 12) as

$$s_x = \beta_x \left( 1 + \frac{d_x/\beta_x}{\alpha_x + i\omega} \right). \quad (33)$$

The complex stretching of the velocity-stress equation 1-2 with the stretching function equation 33 is equivalent to using a stretching function

$$s_x = 1 + \frac{d_x/\beta_x}{\alpha_x + i\omega}. \quad (34)$$

to stretch the following equations

$$\begin{aligned}\frac{\partial \mathbf{v}}{\partial t} &= \frac{1}{\rho} \left( \frac{1}{\beta_x} \nabla_x + \nabla_{\parallel} \right) \cdot \sigma, \\ \frac{\partial \sigma}{\partial t} &= \mathbf{c} : \left\{ \left( \frac{1}{\beta_x} \nabla_x + \nabla_{\parallel} \right) \mathbf{v} + \left[ \left( \frac{1}{\beta_x} \nabla_x + \nabla_{\parallel} \right) \mathbf{v} \right]^T \right\}.\end{aligned}\quad (35)$$

The solutions of equation 35 in a homogenous isotropic medium is the same as the solution of the velocity-stress equations 1-2 in a transversely isotropic medium ( $x$  is the symmetry axis) that has the stiffness tensor

$$\tilde{\mathbf{C}} = \begin{pmatrix} \frac{\lambda+2\mu}{\beta_x^2} & \frac{\lambda}{\beta_x} & \frac{\lambda}{\beta_x} & 0 & 0 & 0 \\ \frac{\lambda}{\beta_x} & \lambda+2\mu & \lambda & 0 & 0 & 0 \\ \frac{\lambda}{\beta_x} & \lambda & \lambda+2\mu & 0 & 0 & 0 \\ 0 & 0 & 0 & \mu & 0 & 0 \\ 0 & 0 & 0 & 0 & \frac{\mu}{\beta_x^2} & 0 \\ 0 & 0 & 0 & 0 & 0 & \frac{\mu}{\beta_x^2} \end{pmatrix}.\quad (36)$$

Thus  $\beta_x$  introduces an anisotropy that reduces the phase velocity of the waves propagating normal to the PML layer to  $\frac{C}{\beta_x}$ . The plane wave solution of equation 35 can be written as,

$$\mathbf{u} = \mathbf{u}_0 e^{i\omega(t - \mathbf{s} \cdot \mathbf{x})},\quad (37)$$

where  $\mathbf{u}_0$  is the polarization vector,  $\mathbf{s} = \frac{\bar{\mathbf{s}}}{\tilde{C}}$  is the slowness vector which is normal to the wavefront surface,  $\tilde{C}$  is the phase velocity depending on the propagation direction. For simplicity, we consider waves propagating in  $(x, z)$ -plane. Thus equation 37 becomes

$$\mathbf{u} = \mathbf{u}_0 e^{i\omega \left( t - \frac{\cos \theta}{\tilde{C}} x - \frac{\sin \theta}{\tilde{C}} z \right)},\quad (38)$$

where  $\theta$  is the angle between the normal direction of the wavefront and  $x$ -axis. Taking equation 34 into equation 8, we can get the stretched  $\tilde{x}$

$$\tilde{x} = x + \int_0^x \frac{\alpha_x d_x / \beta_x}{\alpha_x^2 + \omega^2} d\eta - i \int_0^x \frac{\omega d_x / \beta_x}{\alpha_x^2 + \omega^2} d\eta.\quad (39)$$

Taking above equation into equation 38, we get the plane wave solution of the CFS-PML

$$\mathbf{u} = \mathbf{u}_0 e^{i\omega \left( t - \frac{\cos \theta}{C} x - \frac{\sin \theta}{C} z \right)} e^{-i \frac{\cos \theta}{C} \int_0^x \frac{\omega d_x / \beta_x \alpha_x}{\alpha_x^2 + \omega^2} d\eta} \underbrace{e^{-\frac{\cos \theta}{C} \left[ \int_0^x \frac{\omega^2}{\alpha_x^2 + \omega^2} d_x / \beta_x d\eta \right]}}_D. \quad (40)$$

For waves propagate normal to the PML layer (phase velocity  $\tilde{C} = \frac{C}{\beta_x}$ , and  $\cos \theta = 1$ , assuming a constant  $\beta_x$ ), the damping term  $D$  becomes  $\exp(-\frac{1}{C} [\int_0^x \frac{\omega^2}{\alpha_x^2 + \omega^2} d_x d\eta])$ , in which  $\beta_x$  is canceled out. This indicates that for normal incident waves,  $\beta_x$  only decreases the wave propagation speed without increasing damping. This is still true for a varying  $\beta_x$  profile, since each single layer within the PML can be taken as having a constant  $\beta$ . We validate this by calculating the waveform in the PML with different  $\beta_x$  values for a normal incident plane wave using the FDTD method. We set  $\alpha_x = 0$  and use polynomial scaled  $\beta_x$  and  $d_x$ . Figure 2a shows the maximum amplitude for different  $\beta$  values ( $\beta_0 = 1$  and  $\beta_0 = 9$ ) at each grid point inside a 25-cell-thick PML layer. The maximum amplitude distributions are nearly identical for different  $\beta$ , verifying that  $\beta$  does not increase damping directly. Figure 2b is the comparison of velocity at the grid point 15-cell into the PML, in which the wave using  $\beta_0 = 9$  arrives later than that using  $\beta_0 = 1$  due to the reduced wave speed by  $\beta_x$ . We note that the stretching function in Petropoulos (2000) is of a form  $s_x = \beta_x (1 + \frac{d_x}{\alpha_x + i\omega})$ , whose damping term contains the product of  $\beta_x$  and  $d_x$  in exponent. Therefore  $\beta_x$  in Petropoulos (2000) affects damping.

For grazing incident waves,  $\cos \theta$  is very small without using  $\beta_x$ . Thus the damping term  $D$  in equation 38 may not be small enough to efficiently damp the wave propagating sub-parallel to the PML layer and causes strong spurious reflections. Because of the anisotropy generated by  $\beta_x$ , the normal direction of the wavefront is bended towards the normal direction of the PML layer, thus  $\cos \theta$  in the damping term is increased and the absorption is improved. It should be noted that  $\beta_x$  can not be canceled out in the damping term for oblique incident waves because the phase velocity is a function depending on several components of the stiffness tensor.

## NUMERICAL TESTS

To demonstrate the ADE CFS-PML, we present results of three numerical tests. One is performed in a thin homogeneous 3D slab surrounded by PMLs on all surfaces to investigate the optimal values of the CFS parameters. In the second test, we add a free surface to the thin slab model to validate the modified PML equations that take into account the free surface boundary condition in absorption of surface waves. We use the FDTD method in the first two tests. In the third test, we use the nonstaggered finite-difference method with the 4th-order Runge-Kutta scheme in a two-layered model with a 3D topography to validate the ADE CFS-PML implementation in a higher-order time marching scheme.

Before showing the numerical test results, let us briefly review the choice of the parameter values in the CFS function. According to Roden and Gedney (2000),  $d$ ,  $\beta$  and  $\alpha$  should be spatially scaled in the PML layer to reduce reflection errors in the discrete space.  $d$  usually is zero at the PML-interior interface and maximum at the exterior boundary.  $\beta$  is equal to 1 at the PML-interior interface and maximum at the exterior boundary.  $\alpha$  is scaled in a reversed manner that the value is maximum at the PML-interior interface and gradually reduced to zero at the exterior boundary to absorb low frequency waves.

In this paper, we choose the commonly used  $p$ -order polynomial scaling function (Gedney, 1998; Roden and Gedney, 2000),

$$d_x = d_0 \left( \frac{x}{L} \right)^{p_d}, \quad (41)$$

$$\beta_x = 1 + (\beta_0 - 1) \left( \frac{x}{L} \right)^{p_\beta}, \quad (42)$$

$$\alpha_x = \alpha_0 \left[ 1 - \left( \frac{x}{L} \right)^{p_\alpha} \right], \quad (43)$$

where  $d_0$  and  $\beta_0$  are the maximum value of  $d$  and  $\beta$  at the exterior boundary (the optimal  $\beta_0$  is discussed in the next section),  $\alpha_0$  is the maximum value of  $\alpha$  at the PML-interior interface.  $L$  is

the width of the PML layer,  $x$  is the distance to the PML-interior interface.  $p_d$ ,  $p_\beta$  and  $p_\alpha$  typically range from 1 to 4, and 2 is commonly used. We use  $p_d = 2$  and  $p_\beta = 2$ . We choose  $p_\alpha = 1$  since Martin et al. (2008b) showed the linear variation of  $\alpha$  gets a more pronounced decay of energy.

The maximum value of  $d$  is obtained through a theoretical reflection coefficient relation (Collino and Tsogka, 2001),

$$d_0 = -\frac{(p_d + 1)c_p}{2L} \ln R, \quad (44)$$

where  $c_p$  is the compressional wave speed, and  $R$  is the theoretical reflection coefficient for a normal incident plane P wave with a Dirichlet condition ( $\mathbf{v} = 0$  and  $\sigma = 0$ ) at the exterior boundary of the PML layer. The trade-off between a small and a large  $d_0$  is that a too small  $d_0$  can not damp the wavefield enough in the PML layer and strong spurious reflections from the Dirichlet boundary will propagate back to the physical domain, and a too large  $d_0$  leads to spurious reflections caused by the dispersion (Collino and Tsogka, 2001). Thus the optimal  $d_0$  depends on the PML thickness  $L$  and the theoretical reflection coefficient  $R$ . Collino and Tsogka (2001) proposed  $R$  for different width of the PML layer as  $R^5 = 0.01$ ,  $R^{10} = 0.001$  and  $R^{20} = 0.0001$ , where the superscript denotes the width of the PML region in the amount of grid spacing. Marcinkovich and Olsen (2003) approximated the above relation by a third order polynomial function to get the  $R$  value for an arbitrary PML width between 1 and 20 layers. We approximate the relation by a logarithmic equation,

$$\log_{10} \left( \frac{R}{R^{10}} \right) = \frac{\log_{10}(R^{20}/R^{10})}{\log_{10}(20/10)} \log_{10} \left( \frac{N}{10} \right). \quad (45)$$

Thus  $R$  for an arbitrary PML layer width of  $N$  cell size can be expressed as

$$\log_{10}(R) = -\frac{\log_{10}(N) - 1}{\log_{10}(2)} - 3. \quad (46)$$

Equation 44 is optimized for normal incident waves. For oblique incident waves, a larger  $d_0$  than

that from equation 44 is needed to obtain optimal damping. From numerical tests, we find that increasing  $d_0$  to 2-3 times the value from equation 44 yields better solutions for grazing incidence.

Festa and Vilotte (2005) recommended  $\alpha_0$  to be  $\pi f_c$ , where  $f_c$  is the dominant frequency of the source time function. In our numerical tests, different values of  $\alpha_0$  ( $1.0\pi f_c$ ,  $1.5\pi f_c$  and  $2.0\pi f_c$ ) do not make a significant difference. Thus  $\alpha_0 = \pi f_c$  seems a good choice in practice.

### Thin Homogeneous 3D Slab Surrounded by PMLs

This test compares the performance of the ADE CFS-PML with the standard PML (by setting  $\beta_0 = 1$  and  $\alpha_0 = 0$ ) for body waves impinging the PML interface at a near-grazing angle and shows how the values of  $d_0$ ,  $\beta_0$  and  $\alpha_0$  affect the absorption.

Figure 3 shows the computational configurations. The source time function is a Ricker wavelet with a center frequency of 5 Hz and a time delay of 0.6 second. The time step is 1.5 ms and the total time step is 5000, resulting in a time window of 7.5 s, in which the reflected S wave can travel through the computational domain. The value of  $d_0$  is obtained through equation 44. Different  $\beta_0$  and different  $\alpha_0$  ( $0$ ,  $0.5\pi f_c$ ,  $1.0\pi f_c$ ,  $1.5\pi f_c$  and  $2.0\pi f_c$ ) are tested. The result of a large model (double the size along  $x$  and  $y$  and twelve times larger along  $z$  with a 20-cell-thick PML) is used as the reference.

Figure 4 shows the snapshots of the  $v_z$  component at 3.75 s. P wave has propagated outside the computational domain and the dominant phase is S wave. The standard PML (Figure 4b) shows stronger spurious evanescent waves at the positive  $z$  face.  $\alpha_0 = \pi f_c$  (Figure 4c) can eliminate such kind of spurious waves, but a spurious reflected wave immediately after the S phase can be clearly seen. Increasing  $\alpha_0$  to  $2\pi f_c$  does not significantly affect the result (not shown). Using  $\beta_0 = 10$  in addition to  $\alpha_0 = \pi f_c$  (Figure 4d) reduces the spurious reflected wave and yields better solution

for grazing incidence. Increasing  $d_0$  to three times larger (Figure 4e) can dramatically improve the absorption of grazing incident waves, but causes a stronger spurious reflection of waves at near-normal incidence at the positive  $y$  face. The above results indicate that the choices of the parameters  $\beta_x$ ,  $\alpha_x$  and  $d_0$  are important for absorption of grazing incident waves. A thicker PML (20-cell-thick, Figure 4f) can further absorb the normal incident waves.

Figure 5 shows the comparison of the  $v_z$  time series between the PML models and reference model at the receiver indicated in Figure 3. The amplitude of S wave in both the standard PML (Figure 5a) and the ADE CFS-PML with  $\alpha_0 = \pi f_c$  and  $\beta_0 = 1$  (Figure 5c) is larger than that of the reference model. This larger amplitude S wave consists of the incident S wave and the spurious reflected S wave, which propagates in the nearly same direction as the incident S wave. Figure 5c suggests that though  $\alpha$  can eliminate the spurious evanescent waves, it does not increase the damping of waves at grazing incidence, thus the spurious reflected body waves are still strong. This is reasonable from the damping term expression (without  $\beta_x$ )  $\exp(-\frac{\cos \theta}{C} \int_0^x \frac{\omega^2}{\alpha_x^2 + \omega^2} dx d\eta)$  that  $\alpha$  does not significantly affect the incident angle  $\theta$ , thus  $\cos \theta$  is very small for near-grazing incident waves no matter what value of  $\alpha$  is. On the contrary,  $\beta_x$  bends the wavefront towards the normal direction of the PML, thus decreases the slowness angle  $\theta$  and increases the damping of waves at near-grazing incidence. This effect can be seen from a snapshot comparison of  $\beta = 1$  (Figure 6a) and  $\beta = 10$  (Figure 6b). This is the reason that Figure 5e ( $\alpha_0 = \pi f_c$  and  $\beta_0 = 10$ ) shows the amplitude of S wave is close to that of the reference. But the increased damping due to bending is not large enough for P wave, so a discrepancy in P wave can be seen in Figure 5f. A three times larger  $d_0$  (with  $\beta_0 = 7$ ,  $\alpha_0 = \pi f_c$ ) significantly improves the absorption of waves at grazing incidence and has nearly perfect fits for both P and S waves (Figure 5g-5h).

To quantitatively measure the error, we use the following integral as a local error at the position



$\mathbf{x}$ ,

$$E_L(\mathbf{x}) = \frac{\sum_t |v_{\text{pml}}(\mathbf{x}, t) - v_{\text{ref}}(\mathbf{x}, t)|}{\sum_t |v_{\text{ref}}(\mathbf{x}, t)|}, \quad (47)$$

where  $v_{\text{pml}}(\mathbf{x}, t)$  is the simulated wavefield in the PML model and  $v_{\text{ref}}(\mathbf{x}, t)$  is the counterpart in the reference model. The local error distribution (Figure 7) confirms the conclusions from the waveform comparisons, that  $\alpha$  (Figure 7b,  $\alpha_0 = \pi f_c$ ,  $\beta_0 = 1$ ) eliminates the spurious evanescent waves in the standard PML (Figure 7a) and reduces the local error in the upper part of the computational domain, but the maximum error is still on the same order because the amplitude of the reflected S wave is similar;  $\beta$  (Figure 7c,  $\alpha_0 = \pi f_c$ ,  $\beta_0 = 10$ ) improves the absorption of the grazing incident waves and the local error is much smaller; a three time larger  $d_0$  efficiently increases damping of the grazing incident waves and reduces the local error (Figure 7d,  $\alpha_0 = \pi f_c$ ,  $\beta_0 = 7$ ).

We use an averaged local error in a subgrid located in the  $xz$  plane through  $y = 3000\text{m}$  as an indicator of the global error of the PML with a particular  $\beta_0$  and  $\alpha_0$ ,

$$E_G = \frac{1}{N} \sum_{i=20}^{580} \sum_{j=301}^{301} \sum_{k=20}^{61} E_L(i, j, k), \quad (48)$$

where  $N$  is the total number of the grid points of the subgrid,  $i, j, k$  are the grid index in the subgrid. The subgrid is 10-cell away from the PML-interior interfaces. Figure 8a shows the contour plot of the global error as a function of  $\beta_0$  and  $\alpha_0$ . It can be seen that  $\alpha_0/(\pi f_c)$  between 1 to 2 does not affect the overall accuracy. The optimal value of  $\beta_0$  is around  $10 \sim 12$  in this case. To investigate the optimal  $\beta_0$  variation with respect to the PML thickness  $N$  and the grid spacing (or wave speed, or source frequency), we perform a series numerical calculations with different  $N$  and  $c_s$ . The global error with respect to  $\beta_0$  in Figure 8b shows that the optimal  $\beta_0$  is insensitive to the PML thickness  $N$ , but increases when  $c_s$  increases (equivalent to grid spacing decreases, or source frequency decreases). Theoretically, a larger  $\beta$  can bend waves more efficiently, but a very large  $\beta$  can make the wavelength too short to be resolved by the numerical scheme, which can

cause strong numerical spurious reflections. Figure 8c and 8d show the normalized points per dominant wavelength ( $= \text{PPW} / \text{PPW}_0$ , where PPW is points per dominant wavelength,  $\text{PPW}_0$  is the minimal PPW requirement of the numerical scheme. For the 4th-order staggered finite-difference,  $\text{PPW}_0 = 6$ ) distribution inside the PML layer at the center frequency for the optimal  $\beta_0$  in Figure 8b ( $\beta_0 = 11$  for  $c_s = 1600$  m/s, and  $\beta_0 = 15$  for  $c_s = 2300$  m/s). The normalized points per dominant wavelength at the exterior boundary is around 0.5 in difference cases. Thus we can estimate the optimal  $\beta_0$  through

$$\beta_0 = \frac{C}{0.5 \text{PPW}_0 \Delta h f_c}. \quad (49)$$

It should be noted that we use the same parameter values in all PMLs on the six faces in this numerical test. In practice, one can use larger  $\beta_0$  and  $d_0$  only for a particular PML layer, for which grazing incidence is important.

### Thin 3D Slab With the Free Surface

We change one face of the thin slab in the previous test to the free surface to demonstrate the absorption of surface waves of the ADE CFS-PML and the effect of the modified PML equations that take into account the free surface boundary condition.

Figure 9 shows the computational configurations. The vertical force is located at (200, 3000, 795) m, half grid below the free surface. All other parameters are the same as the model in Figure 3. The free surface boundary condition is implemented using AFDA technique (Kristek et al., 2002), in which a compact finite-difference operator and biased finite-difference operators are used to calculate derivatives with respect to  $z$  axis at grid points near the free surface.

Figure 10 is the snapshot of the  $v_z$  component at 3.75 s. The free surface coincides with the location of the normal stress components. Because waves do not impinge the PML at near-grazing

incidence, the standard PML (Figure 10b) and the ADE CFS-PML (Figure 10c,  $\beta_0 = 1$  and  $\alpha_0 = \pi f_c$ ) both efficiently absorb surface waves. For the same reason, increasing  $\beta_0$  (not shown here) does not make significant difference. If the modified ADE CFS-PML equations 31 and 32 which incorporate the free surface boundary are not used, a relatively strong reflected surface phase can be clearly seen (Figure 10d). If the free surface is located at the  $\sigma_{xz}$  component, the amplitude of the reflected wave is smaller than Figure 10d, but stronger than Figure 10b. Thus the absorption of surface waves when the free surface coincident with the  $\sigma_{xz}$  component is not as efficient as the free surface coincident with the normal stress components.

### Two-layered Medium With Free Surface Topography in a Narrow Vertical Slice

In this test, we validate the ADE CFS-PML implementation in the 4th-order Runge-Kutta scheme, and demonstrate the optimal performance of the ADE CFS-PML in a narrow vertical slice to simulate wave propagation in a common situation involving seismic profiles.

The medium has two layers (Figure 11) separated at  $z = -8\text{km}$ . Boundary-conforming grid is used to conform grid with the surface topography. The horizontal grid spacing is 50m and a varying grid spacing (33m  $\sim$  60m) is used vertically. The source time function is a Ricker wavelet with a center frequency of 1.5 Hz and a time delay of 1 s. The value of  $d_0$  is calculated from equation 44, where the  $c_p$  of the first layer (3000 m/s) is used for the PML layers at  $x$  and  $y$  faces, and  $c_p$  of the lower layer (5000 m/s) is used for the bottom PML layer. The value of  $\alpha_0$  is  $\pi f_c$ . The optimal  $\beta_0$  is estimated to be 8 from equation 49 using the surface wave speed of the first layer. We also simulate with  $\beta_0 = 1$  for comparison with the optimal  $\beta_0$  value. Numerical solution of a larger model (double the length and depth, five times the width, a 25-cell-thick PML) is used as reference.

The difference between the ADE CFS-PML (Figure 12b,  $\alpha_0 = \pi f_c$  and  $\beta_0 = 1$ ) solution and

that of the reference (Figure 12a) is so small that it is hard to observe from the snapshots when the color is scaled to 1% of the maximum amplitude. Thus we compare the  $v_z$  time series at the receiver (triangle in Figure 11). Figure 13a shows the comparison between the solution of the reference (solid line), PML with  $\beta_0 = 1$  (dash-dotted line) and PML with  $\beta_0 = 8$  (dotted line).  $\alpha_0 = \pi f_c$  is used for both PML solutions. The fit is nearly perfect at this scale. Figure 13b shows the comparison in the time window 13 ~ 21 s with amplitude scaled to 0.2% of that in Figure 13a. We note that even at this scale, the solution of  $\beta_0 = 8$  (dotted line) overlaps with the reference, suggesting that the ADE CFS-PML with the optimal  $\beta$  matches the reference for this complex waveform containing scattered waves from the topography and multiple reflections from the inner interface. To further highlight the difference, Figure 13c shows the  $v_z$  difference between the PML with  $\beta_0 = 1$  and the reference ( $v_z^{\beta_0=1} - v_z^{ref}$ ) and that between the PML with  $\beta_0 = 8$  and the reference ( $v_z^{\beta_0=8} - v_z^{ref}$ ). The  $y$ -axis scale is around 0.5% of that in Figure 13a. It is clear the ADE CFS-PML can efficiently absorb waves in this narrow two-layered topographic model. The spurious waves do not significantly affect the reflections from the inner interface. The optimal  $\beta_0$  yields a better solution with the amplitude of the spurious waves smaller than that of  $\beta_0 = 1$ , at a level below 0.1% of the maximum amplitude. This numerical test indicates that we can use a narrow slice mesh with the ADE CFS-PML to simulate full wave propagation in complex structure models in a common situation involving seismic profiles.

## CONCLUSION

We introduce an efficient unsplit-field complex frequency-shifted perfectly matched layer implementation using auxiliary differential equations in seismic wave modeling. We derive the complete ADE CFS-PML equations for the velocity-stress equations. Because the ADE CFS-PML equations are first-order partial differential equations, it can be solved by the some numerical scheme used

in the inner domain no matter what time marching scheme is used. We demonstrate this by implementing the ADE CFS-PML in the 2nd-order leap-frog scheme and the 4th-order Runge-Kutta scheme.

We analyze the role of the scaling factor  $\beta$  in the CFS-PML and demonstrate that it introduces an intermediate transformation of the velocity-stress equations into an anisotropic medium that has a lower wave speed normal to the PML layer. For normal incident waves, it only delays the waves propagating into the PML layer without increased damping. For oblique incident waves, it can bend the waves towards the normal direction, thus increases  $\cos \theta$  in the damping term and improves the absorption. Numerical tests indicate that the frequency shifted factor  $\alpha$  only eliminates the evanescent waves caused by near-grazing incident waves, but does not significantly improve the absorption of the reflected body waves.  $\beta$  is more efficient and important in absorbing grazing incident waves.

Our numerical tests indicate that the incompatibility between the PML equations and the free surface boundary condition implementation can cause an unstable wave originating from the free surface in the PML layer in the nonstaggered-grid finite-difference. Thus we derive the PML equations taking the free surface boundary condition into account. Numerical tests validate that these modified PML equations solve the instability problem in the non-staggered finite-difference method, and improve the efficiency of absorbing surface waves in the staggered finite-difference method when the free surface coincides with the normal stress components.

We perform a series of numerical tests to validate the ADE CFS-PML implementation both in the FDTD method and the nonstaggered-grid finite-difference method using the 4th-order Runge-Kutta scheme. We investigate the different values of the CFS parameters on the efficiency of absorption based on quantitative error criteria. Our numerical tests indicate that the optimal  $\beta$  reduces the

points per dominant wavelength at the exterior boundary to three for the 4th-order finite-difference operator, around half the value required by the numerical scheme. Different values of  $\alpha_0$  ( $1.0\pi f_c$ ,  $1.5\pi f_c$  and  $2.0\pi f_c$ ) do not make a significant difference. Thus  $\alpha_0 = \pi f_c$  seems a good choice in practice. For grazing incidence, adjusting only parameters  $\alpha$  and  $\beta$  is not enough, one also needs to increase the maximum value  $d_0$  of the damping profile  $d$  to get optimal absorption.

Numerical test of a two-layered model with a surface topography in a narrow vertical slice indicates that the ADE CFS-PML yields accurate results compared with the reference in a much larger and thicker model, thus making it possible to carry out efficient 3D forward simulation in a common situation involving seismic profiles in seismic exploration.

# ACKNOWLEDGMENTS

This research was supported by the U.S. National Science Foundation (Grant number NSF-0551117) and U.S. Air Force Research Laboratory (Contract number fa8718-06-c-0014). We thank Giannopoulos' reminder of the 1st-order accuracy of the CPML implementation and fruitful comments on the ADE CFS-PML implementation in the FDTD method. Comments by Vladimir Grechka, Evert Slob and an anonymous reviewer help to improve the manuscript.

## APPENDIX A

## ADE CFS-PML EQUATIONS FOR THE ELASTIC WAVE EQUATIONS

ADE CFS-PML equations for the velocity-stress formulation of the elastic wave equations are

$$\begin{aligned}\sigma_{xx,t} = & (\lambda + 2\mu)v_{x,x} + \lambda v_{y,y} + \lambda v_{z,z} \\ & + (\lambda + 2\mu) \left[ \frac{1}{\beta_x} - 1 \right] v_{x,x} + \lambda \left[ \frac{1}{\beta_y} - 1 \right] v_{y,y} + \lambda \left[ \frac{1}{\beta_z} - 1 \right] v_{z,z} \\ & - (\lambda + 2\mu) \frac{1}{\beta_x} V_x^x - \lambda \frac{1}{\beta_y} V_y^y - \lambda \frac{1}{\beta_z} V_z^z,\end{aligned}\quad (\text{A-1})$$

$$\begin{aligned}\sigma_{yy,t} = & \lambda v_{x,x} + (\lambda + 2\mu)v_{y,y} + \lambda v_{z,z} \\ & + \lambda \left[ \frac{1}{\beta_x} - 1 \right] v_{x,x} + (\lambda + 2\mu) \left[ \frac{1}{\beta_y} - 1 \right] v_{y,y} + \lambda \left[ \frac{1}{\beta_z} - 1 \right] v_{z,z} \\ & - \lambda \frac{1}{\beta_x} V_x^x - (\lambda + 2\mu) \frac{1}{\beta_y} V_y^y - \lambda \frac{1}{\beta_z} V_z^z,\end{aligned}\quad (\text{A-2})$$

$$\begin{aligned}\sigma_{zz,t} = & \lambda v_{x,x} + \lambda v_{y,y} + (\lambda + 2\mu)v_{z,z} \\ & + \lambda \left[ \frac{1}{\beta_x} - 1 \right] v_{x,x} + \lambda \left[ \frac{1}{\beta_y} - 1 \right] v_{y,y} + (\lambda + 2\mu) \left[ \frac{1}{\beta_z} - 1 \right] v_{z,z} \\ & - \lambda \frac{1}{\beta_x} V_x^x - \lambda \frac{1}{\beta_y} V_y^y - (\lambda + 2\mu) \frac{1}{\beta_z} V_z^z,\end{aligned}\quad (\text{A-3})$$

$$\sigma_{yz,t} = \mu(v_{y,z} + v_{z,y}) + \mu \left( \left[ \frac{1}{\beta_z} - 1 \right] v_{y,z} + \left[ \frac{1}{\beta_y} - 1 \right] v_{z,y} \right) - \mu \left( \frac{1}{\beta_z} V_y^z + \frac{1}{\beta_y} V_z^y \right), \quad (\text{A-4})$$

$$\sigma_{xz,t} = \mu(v_{x,z} + v_{z,x}) + \mu \left( \left[ \frac{1}{\beta_z} - 1 \right] v_{x,z} + \left[ \frac{1}{\beta_x} - 1 \right] v_{z,x} \right) - \mu \left( \frac{1}{\beta_z} V_x^z + \frac{1}{\beta_x} V_z^x \right), \quad (\text{A-5})$$

$$\sigma_{xy,t} = \mu(v_{x,y} + v_{y,x}) + \mu \left( \left[ \frac{1}{\beta_y} - 1 \right] v_{x,y} + \left[ \frac{1}{\beta_x} - 1 \right] v_{y,x} \right) - \mu \left( \frac{1}{\beta_y} V_x^y + \frac{1}{\beta_x} V_y^x \right), \quad (\text{A-6})$$

$$\begin{aligned}\rho v_{x,t} = & \sigma_{xx,x} + \sigma_{xy,y} + \sigma_{xz,z} \\ & + \left[ \frac{1}{\beta_x} - 1 \right] \sigma_{xx,x} + \left[ \frac{1}{\beta_y} - 1 \right] \sigma_{xy,y} + \left[ \frac{1}{\beta_z} - 1 \right] \sigma_{xz,z} - \frac{1}{\beta_x} T_{xx}^x - \frac{1}{\beta_y} T_{xy}^y - \frac{1}{\beta_z} T_{xz}^z,\end{aligned}\quad (\text{A-7})$$

$$\begin{aligned}\rho v_{y,t} = & \sigma_{xy,x} + \sigma_{yy,y} + \sigma_{yz,z} \\ & + \left[ \frac{1}{\beta_x} - 1 \right] \sigma_{xy,x} + \left[ \frac{1}{\beta_y} - 1 \right] \sigma_{yy,y} + \left[ \frac{1}{\beta_z} - 1 \right] \sigma_{yz,z} - \frac{1}{\beta_x} T_{xy}^x - \frac{1}{\beta_y} T_{yy}^y - \frac{1}{\beta_z} T_{yz}^z,\end{aligned}\quad (\text{A-8})$$

$$\begin{aligned}\rho v_{z,t} = & \sigma_{xz,x} + \sigma_{yz,y} + \sigma_{zz,z} \\ & + \left[ \frac{1}{\beta_x} - 1 \right] \sigma_{xz,x} + \left[ \frac{1}{\beta_y} - 1 \right] \sigma_{yz,y} + \left[ \frac{1}{\beta_z} - 1 \right] \sigma_{zz,z} - \frac{1}{\beta_x} T_{xz}^x - \frac{1}{\beta_y} T_{yz}^y - \frac{1}{\beta_z} T_{zz}^z,\end{aligned}\quad (\text{A-9})$$

with the auxiliary differential equations for the memory variables damping along  $x$ ,

$$\begin{aligned} V_{x,t}^x + \left(\alpha_x + \frac{d_x}{\beta_x}\right) V_x^x &= \frac{d_x}{\beta_x} v_{x,x}, & V_{y,t}^x + \left(\alpha_x + \frac{d_x}{\beta_x}\right) V_y^x &= \frac{d_x}{\beta_x} v_{y,x}, \\ V_{z,t}^x + \left(\alpha_x + \frac{d_x}{\beta_x}\right) V_z^x &= \frac{d_x}{\beta_x} v_{z,x}, & T_{xx,t}^x + \left(\alpha_x + \frac{d_x}{\beta_x}\right) T_{xx}^x &= \frac{d_x}{\beta_x} \sigma_{xx,x}, \\ T_{xy,t}^x + \left(\alpha_x + \frac{d_x}{\beta_x}\right) T_{xy}^x &= \frac{d_x}{\beta_x} \sigma_{xy,x}, & T_{xz,t}^x + \left(\alpha_x + \frac{d_x}{\beta_x}\right) T_{xz}^x &= \frac{d_x}{\beta_x} \sigma_{xz,x}, \end{aligned} \quad (\text{A-10})$$

and for the memory variables damping along  $y$ ,

$$\begin{aligned} V_{x,t}^y + \left(\alpha_y + \frac{d_y}{\beta_y}\right) V_x^y &= \frac{d_y}{\beta_y} v_{x,y}, & V_{y,t}^y + \left(\alpha_y + \frac{d_y}{\beta_y}\right) V_y^y &= \frac{d_y}{\beta_y} v_{y,y}, \\ V_{z,t}^y + \left(\alpha_y + \frac{d_y}{\beta_y}\right) V_z^y &= \frac{d_y}{\beta_y} v_{z,y}, & T_{xy,t}^y + \left(\alpha_y + \frac{d_y}{\beta_y}\right) T_{xy}^y &= \frac{d_y}{\beta_y} \sigma_{xy,y}, \\ T_{yy,t}^y + \left(\alpha_y + \frac{d_y}{\beta_y}\right) T_{yy}^y &= \frac{d_y}{\beta_y} \sigma_{yy,y}, & T_{yz,t}^y + \left(\alpha_y + \frac{d_y}{\beta_y}\right) T_{yz}^y &= \frac{d_y}{\beta_y} \sigma_{yz,y}, \end{aligned} \quad (\text{A-11})$$

and for the memory variables damping along  $z$ ,

$$\begin{aligned} V_{x,t}^z + \left(\alpha_z + \frac{d_z}{\beta_z}\right) V_x^z &= \frac{d_z}{\beta_z} v_{x,z}, & V_{y,t}^z + \left(\alpha_z + \frac{d_z}{\beta_z}\right) V_y^z &= \frac{d_z}{\beta_z} v_{y,z}, \\ V_{z,t}^z + \left(\alpha_z + \frac{d_z}{\beta_z}\right) V_z^z &= \frac{d_z}{\beta_z} v_{z,z}, & T_{xz,t}^z + \left(\alpha_z + \frac{d_z}{\beta_z}\right) T_{xz}^z &= \frac{d_z}{\beta_z} \sigma_{xz,z}, \\ T_{yz,t}^z + \left(\alpha_z + \frac{d_z}{\beta_z}\right) T_{yz}^z &= \frac{d_z}{\beta_z} \sigma_{yz,z}, & T_{zz,t}^z + \left(\alpha_z + \frac{d_z}{\beta_z}\right) T_{zz}^z &= \frac{d_z}{\beta_z} \sigma_{zz,z}. \end{aligned} \quad (\text{A-12})$$

At the free surface in the PML layer, the PML equations of  $\sigma_{xx,t}$  and  $\sigma_{yy,t}$  taking the free surface boundary condition into account are

$$\begin{aligned} \sigma_{xx,t} &= (\lambda + 2\mu) v_{x,x} + \lambda v_{y,y} + \lambda v_{z,z} \\ &+ (\lambda + 2\mu) \left[ \frac{1}{\beta_x} - 1 \right] v_{x,x} + \lambda \left[ \frac{1}{\beta_y} - 1 \right] v_{y,y} + (\lambda + 2\mu) \frac{1}{\beta_x} V_x^x + \lambda \frac{1}{\beta_y} V_y^y \\ &- \frac{\lambda^2}{\lambda + 2\mu} \left\{ \left[ \frac{1}{\beta_x} - 1 \right] v_{x,x} + \left[ \frac{1}{\beta_y} - 1 \right] v_{y,y} \right\} - \frac{\lambda^2}{\lambda + 2\mu} \left[ \frac{1}{\beta_x} V_x^x + \frac{1}{\beta_y} V_y^y \right] \\ \sigma_{yy,t} &= \lambda v_{x,x} + (\lambda + 2\mu) v_{y,y} + \lambda v_{z,z} \\ &+ \lambda \left[ \frac{1}{\beta_x} - 1 \right] v_{x,x} + (\lambda + 2\mu) \left[ \frac{1}{\beta_y} - 1 \right] v_{y,y} + \lambda \frac{1}{\beta_x} V_x^x + (\lambda + 2\mu) \frac{1}{\beta_y} V_y^y \\ &- \frac{\lambda^2}{\lambda + 2\mu} \left\{ \left[ \frac{1}{\beta_x} - 1 \right] v_{x,x} + \left[ \frac{1}{\beta_y} - 1 \right] v_{y,y} \right\} - \frac{\lambda^2}{\lambda + 2\mu} \left[ \frac{1}{\beta_x} V_x^x + \frac{1}{\beta_y} V_y^y \right]. \end{aligned} \quad (\text{A-13})$$



## REFERENCES

- Abarbanel, S. and D. Gottlieb, 1997, A mathematical analysis of the PML method: *J. Comput. Phys.*, **134**, 357–363.
- Appelö, D. and G. Kreiss, 2006, A new absorbing layer for elastic waves: *Journal of Computational Physics*, **215**, 642–660.
- Bayliss, A., K. E. Jordan, B. J. Lemesurier, and E. Turkel, 1986, A 4th-order accurate finite-difference scheme for the computation of elastic-waves: *Bull. Seism. Soc. Am.*, **76**, 1115–1132.
- Bécache, E., S. Fauqueux, and P. Joly, 2003, Stability of perfectly matched layers, group velocities and anisotropic waves: *J. Comput. Phys.*, **188**, 399–433.
- Bérenger, J. P., 1994, A perfectly matched layer for the absorption of electromagnetic waves: *J. Comput. Geophys.*, **114**, 185–200.
- Cerjan, C., D. Kosloff, R. Kosloff, and M. Reshef, 1985, A nonreflecting boundary-condition for discrete acoustic and elastic wave-equations: *Geophysics*, **50**, 705–708.
- Chew, W. and Q. Liu, 1996, Perfectly matched layers for elastodynamics: a new absorbing boundary condition: *J. Comput. Acoustics*, **4**, 341–359.
- Chew, W. and W. Weedon, 1994, A 3D perfectly matched medium from modified maxwell's equations with stretched coordinates: *Microwave and Optical Technology Letters*, **7**, 599–604.
- Clayton, R. and B. Engquist, 1977, Absorbing boundary conditions for acoustic and elastic wave equations: *Bull. Seismol. Soc. Am.*, **67**, 1529–1540.
- Collino, F. and C. Tsogka, 2001, Application of the PML absorbing layer model to the linear elastodynamic problem in anisotropic heterogeneous media: *Geophysics*, **66**, 294–307.
- Drossaert, F. H. and A. Giannopoulos, 2007a, Complex frequency shifted convolution PML for FDTD modelling of elastic waves: *Wave Motion*, **44**, 593–604.
- , 2007b, A nonsplit complex frequencyshifted PML based on recursive integration for FDTD

- modeling of elastic waves: *Geophysics*, **72**(2), T9T17.
- Festa, G., E. Delavaud, and J. P. Vilotte, 2005, Interaction between surface waves and absorbing boundaries for wave propagation in geological basins: 2D numerical simulations: *Geophysical Research Letters*, **32**, L20306.
- Festa, G. and J. P. Vilotte, 2005, The newmark scheme as velocity-stress time-staggering: An efficient PML implementation for spectral-element simulations of elastodynamics: *Geophysical Journal International*, **161**, 789–812.
- Gedney, S. D., 1996, An anisotropic PML absorbing media for the FDTD simulation of fields in lossy and dispersive media: *Electromagnetics*, **16**, 399–415.
- , 1998, The perfectly matched layer absorbing medium, *in* Taflove, A., ed., *Advances in Computational Electrodynamics: The Finite-Difference Time-Domain Method*, 263–340, Artech House.
- Giannopoulos, A., 2008, An improved new implementation of complex frequency shifted PML for the FDTD method: *Antennas and Propagation, IEEE Transactions on*, **56**, 2995–3000.
- Gottschammer, E. and K. Olsen, 2001, Accuracy of the explicit planar free-surface boundary condition implemented in a fourth-order staggered-grid velocity-stress finite-difference scheme: *Bull. Seism. Soc. Am.*, **91**, 617–623.
- Graves, R., 1996, Simulating seismic wave propagation in 3d elastic media using staggered-grid finite differences: *Bull. Seism. Soc. Am.*, **86**, 1091–1106.
- Hagstrom, T., 2003, Perfectly matched layers for hyperbolic systems with applications to the linearized euler equations, *in* et al., C., ed., *Mathematical and Numerical Aspects of Wave Propagation*, *Proceedings Waves 2003*, 125129, Springer-Verlag.
- Hastings, F., J. Schneider, , and S. Broschat, 1996, Application of the perfectly matched layer (PML) absorbing boundary condition to elastic wave propagation: *J. Acoust. Soc. Am.*, **100**(5),

3061–3069.

Higdon, R., 1986, Absorbing boundary conditions for difference approximations to the multidimensional wave equation: *Math. Comput.*, **47**, 437–459.

———, 1990, Radiation boundary conditions for elastic wave propagation: *SIAM J. Numer. Anal.*, **27**, 831–870.

Hixon, R., 1997, On increasing the accuracy of MacCormack schemes for aeroacoustic applications: Presented at the AIAA Paper 97-1586, 3rd AIAA/CEAS Aeroacoustics Conference.

Komatitsch, D. and R. Martin, 2007, An unsplit convolutional perfectly matched layer improved at grazing incidence for the seismic wave equation: *Geophysics*, **72**(5), SM155SM167.

Kristek, J., P. Moczo, and R. Archuleta, 2002, Efficient methods to simulate planar free surface in the 3D 4(th)-order staggered-grid finite-difference schemes: *Studia Geophysica et Geodaetica*, **46**, 355–381.

Kuzuoglu, M. and R. Mittra, 1996, Frequency dependence of the constitutive parameters of causal perfectly matched anisotropic absorbers: *IEEE Microwave and GuidedWave Letters*, **6**, 447–449.

Levander, A., 1988, 4th-order finite-difference P-SV seismograms: *Geophysics*, **53**, 1425–1436.

Liao, Z. P., H. L. Wong, B. P. Yang, and Y. F. Yuan, 1984, A transmitting boundary for transient wave analysis: *Scientia Sinica*, **27**, 1063–1076.

Liu, Q., 1999, Perfectly matched layers for elastic waves in cylindrical and spherical coordinates: *JOURNAL OF THE ACOUSTICAL SOCIETY OF AMERICA*, **105**, 2075–2084.

Luebbers, R. J. and F. Hunsberger, 1992, FDTD for Nth-order dispersive media: *IEEE Transactions on Antennas and Propagation*, **40**, 1297–1301.

Marcinkovich, C. and K. Olsen, 2003, On the implementation of perfectly matched layers in a three-dimensional forth-order velocity-stress finite difference scheme: *J. Geophys. Res.*, **108**, B5,2276.

Martin, R., D. Komatitsch, and A. Ezziiani., 2008a, An unsplit convolutional perfectly matched layer

- improved at grazing incidence for seismic wave propagation in poroelastic media: *Geophysics*, **73**(4), T51–T61.
- Martin, R., D. Komatitsch, and S. D. Gedney, 2008b, A variational formulation of a stabilized unsplit convolutional perfectly matched layer for the isotropic or anisotropic seismic wave equation: *CMES*, **37**(3), 274–304.
- Meza-Fajardo, K. C. and A. S. Papageorgiou, 2008, A nonconvolutional, split-field, perfectly matched layer for wave propagation in isotropic and anisotropic elastic media; stability analysis: *Bull. Seismol. Soc. Am.*, **98**(4), 1811–1836.
- Petropoulos, P. G., 2000, Reflectionless sponge layers as absorbing boundary conditions for the numerical solution of maxwell's equations in rectangular, cylindrical, and spherical coordinates: *SIAM J. Appl. Math.*, **60**(3), 1037–1058.
- Ramadan, O., 2003, Auxiliary differential equation formulation: An efficient implementation of the perfectly matched layer: *IEEE Microwave and Wireless Components Letters*, **13**(2), 69–71.
- Randall, C. J., 1988, Absorbing boundary condition for the elastic wave equation: *Geophysics*, **53**, 611–624.
- Roden, J. A. and S. D. Gedney, 2000, Convolution PML (CPML): An efficient FDTD implementation of the CFS-PML for arbitrary media: *Microwave and Optical Technology Letters*, **27**, 334–339.
- Sacks, Z., D. Kingsland, R. Lee, and J. Lee, 1995, A perfectly matched anisotropic absorber for use as an absorbing boundary condition: *IEEE Transactions on Antennas and Propagation*, **43**, 1460–1463.
- Sochacki, J., R. Kubichek, J. George, W. R. Fletcher, and S. Smithson, 1987, Absorbing boundary conditions and surface waves: *Geophysics*, **52**, 60–71.
- Teixeira, F. L. and W. C. Chew, 2000, Complex space approach to perfectly matched layers: a

review and some new developments: *Int. J. Numer. Model.*, **13**, 441–455.

Wang, L. and C. Liang, 2006, A new implementation of CFS-PML for ADI-FDTD method: *Microwave and Optical Technology Letters*, **48(10)**, 1924–1928.

Wang, T. and X. Tang, 2003, Finite-difference modeling of elastic wave propagation: A nonsplitting perfectly matched layer approach: *Geophysics*, **68**, 1749–1755.

Zeng, Y. and Q. Liu, 2004, A multidomain PSTD method for 3D elastic wave equations: *Bull. Seism. Soc. Am.*, **94(3)**, 1002–1015.

Zhang, W. and X. Chen, 2006, Traction image method for irregular free surface boundaries in finite difference seismic wave simulation: *Geophysical Journal International*, **167**, 337–353.

## LIST OF FIGURES

1 A 3D computational domain surrounded by PML layers on each face. Dashed lines mark the PML-interior interfaces. Along the edge of the computational domain, two directional PMLs exist. At the corner, three directional PMLs co-exist.

2 (a) Maximum amplitude distribution for different  $\beta$  values ( $\beta_0 = 1$ , solid line and  $\beta_0 = 9$ , dotted line) for a 25-cell-thick PML of a normal incident plane wave.  $\alpha = 0$  and an optimal  $d$  are used. (b) Velocity seismogram at the grid point 15-cell into the PML for  $\beta_0=1$  (solid line) and  $\beta_0 = 9$  (dotted line). The wave using  $\beta_0 = 9$  arrives later than that using  $\beta_0 = 1$  due to the reduced wave speed by  $\beta_x$ .

3 A thin homogeneous 3D slab surrounded by 10-cell-thick PMLs on all six faces (three cross-sections are shown). The PML-interior interfaces are indicated by dashed lines. The medium has a compressional wave speed  $c_p = 3200$  m/s, shear wave speed  $c_s = 1600$  m/s, and density  $\rho = 2200$  kg/m<sup>3</sup>. The grid spacing is 10 m, the total grid number is  $600 \times 600 \times 81$ , and the size of the model is  $5990 \times 5990 \times 800$  m. The star symbol shows the location of the vertical force (200, 3000, 600) m, ten cells away both from the PML-interior interface at the negative  $x$  face and from that at the positive  $z$  face. The triangle symbol indicates the receiver (5790, 3000, 600) m, ten cells away from both the PML-interior interface at the positive  $x$  face and that at the positive  $z$  face.

4 Snapshots of the  $v_z$  component of the thin slab model (Figure 3) at 3.75 s. The color is scaled to 0.1% of the maximum absolute amplitude. White lines are the PML-interior interfaces. (a) Reference solution. (b) Standard PML. (c)  $\alpha_0 = \pi f_c$  and  $\beta_0 = 1$ . (d)  $\alpha_0 = \pi f_c$  and  $\beta_0 = 10$ . (e)  $\alpha_0 = \pi f_c$ ,  $\beta_0 = 7$  and a three times larger  $d_0$ . (f)  $\alpha_0 = \pi f_c$  and  $\beta_0 = 11$  for a 20-cell-thick PML.

5 The  $v_z$  seismograms at the receiver shown in Figure 3. The right column shows the same seismograms except that the  $y$  axis is scaled to 1% of that of the left column to highlight the dif-

ference. The first arrival in the right column is P wave, which is nearly invisible in the left column. (a)-(b) Standard PML. (c)-(d)  $\beta_0 = 1$  and  $\alpha_0 = \pi f_c$ . (e)-(f)  $\beta_0 = 10$  and  $\alpha_0 = \pi f_c$ . (g)-(h)  $\beta_0 = 7$ ,  $\alpha_0 = \pi f_c$  and a three times larger  $d_0$ .

6 Snapshots of  $v_z$  on the cross-section in the middle of  $y$  axis at 3.75 s. The color is scaled to the same maximum absolute amplitude. Green lines are the PML-interior interfaces. (a)  $\alpha_0 = \pi f_c$  and  $\beta_0 = 1$ . The amplitude of S wave in the upper PML layer is even larger than that in the physical region, which indicates  $\alpha$  does not efficiently absorb this near-grazing propagating body wave. The distribution of the peak amplitude is wider than Figure 6b, which indicates the reflected wave propagates into the physical domain. (b)  $\alpha_0 = \pi f_c$  and  $\beta_0 = 10$ . The wave front is bended towards the normal direction inside both the upper PML layer and the bottom PML layer. The amplitude of S wave exhibits damping in the PML layers.

7 Local error distribution. The color is scaled to 0.5. White lines show the PML-interior interfaces. (a) Standard PML. (b)  $\beta_0 = 1$  and  $\alpha_0 = \pi f_c$ . (c)  $\beta_0 = 10$  and  $\alpha_0 = \pi f_c$ . (d)  $\beta_0 = 7$ ,  $\alpha_0 = \pi f_c$  and a three times larger  $d_0$ .

8 (a) Contours of the global error as a function of  $\alpha_0$  and  $\beta_0$ . The values of  $\frac{\alpha_0}{\pi f_c}$  between 1 to 2 do not significantly affect the overall accuracy. The optimal value of  $\beta_0$  is around  $10 \sim 12$ . (b) Global error variation with respect to  $\beta_0$ , PML thickness  $N$  and S velocities  $c_s$  ( $\alpha_0$  is fixed to  $\pi f_c$ ). The minimal global error is around 11 for different PML thicknesses of 10, 12 and 20 ( $c_s = 1600$  m/s), indicating the optimal  $\beta_0$  is not sensitive to the thickness of the PML. For  $N = 20$  and  $c_s = 2200$  m/s, the optimal  $\beta_0$  is around 15. (c) Normalized points per dominant wavelength variation inside the PML layer for S wave for different PML thickness  $N$  and S wave speed  $c_s$ . (d) The zoom view of Figure 8c to highlight details. The normalized points per dominant wavelength is around 0.5 at the exterior boundary in difference cases.

9 Thin slab model with the free surface. A 10-cell-thick PML (dashed lines) is applied

on all the faces except the free surface. The star symbol shows the location of the vertical force (200, 3000, 795) m, ten cells away from the PML-interior interface at the negative  $x$  direction and half cell below the free surface. Other parameters are the same as in Figure 3.

10 Snapshots of the  $v_z$  component of the free-surface slab model at 3.75 s. The color is scaled to 0.1% of the maximum absolute amplitude. White lines show the PML-interior interfaces. (a) Reference solution. (b) Standard PML. (c)  $\beta_0 = 1$  and  $\alpha_0 = \pi f_c$ . (d) Standard PML without using the modified PML equations 31 and 32. Strong spurious reflected surface waves can be clearly seen. (e) Standard PML with the free surface coincident with the location of the  $\sigma_{xz}$  component.

11 The two-layered model with the free surface topography, which is defined by  $z = 1000 \exp(-r^2/1000^2)$ , where  $r = \sqrt{x^2 + y^2}$ . When  $r > 2000$  m,  $z_0$  is damped to zero by a Gaussian function. The model is 19.95 km in length, 6.15 km in width and 10.7 km in depth (including PML layers). The interface is at  $z = -8$  km, and the medium parameters are  $c_p = 3000$  m/s,  $c_s = 2000$  m/s,  $\rho = 1200$  kg/m<sup>3</sup> for the upper layer and  $c_p = 5000$  m/s,  $c_s = 2500$  m/s,  $\rho = 1800$  kg/m<sup>3</sup> for the lower layer. A 12-cell-thick PML is applied on all the faces except the free surface (white lines). The star symbol shows the location of the vertical force (−8000, 0, −500) m, and the triangle symbols indicates the receiver's location (9000, 0, 0) m, seven cells distance to the PML-interior interface at the positive  $x$  face.

12 Snapshots of  $v_z$  at 7 s on the  $xz$  cross-section through the middle point of  $y$  axis. The color is scaled to less than 1% of the maximum absolute amplitude. White lines are the PML-interior interfaces. (a) Reference solution. (b)  $\beta_0 = 1$ ,  $\alpha_0 = \pi f_c$ .

13 (a) Comparison of seismograms ( $v_z$ ) for the reference (solid line),  $\beta_0 = 1$  (dashed line) and  $\beta_0 = 8$  (dotted line) at the receiver shown in Figure 11. (b) Detailed comparison within the time window 13 ~ 21 s and the amplitude is zoomed in to 0.2% of that in Figure 13a. Difference can be seen between the reference and  $\beta_0 = 1$ . The solution with  $\beta_0 = 8$  overlaps with the reference.



(c) Difference between solutions from the CFS ADE-PML and the reference. Solid line shows the difference for  $\beta_0 = 1$ , and dotted line for the optimal  $\beta_0 = 8$ .

For Peer Review

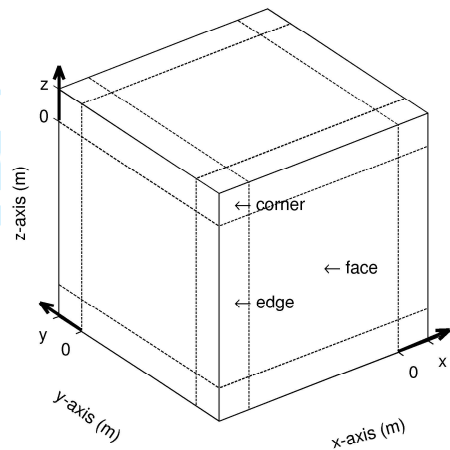


Figure 1: A 3D computational domain surrounded by PML layers on each face. Dashed lines mark the PML-interior interfaces. Along the edge of the computational domain, two directional PMLs exist. At the corner, three directional PMLs co-exist.

**Zhang & Shen –**

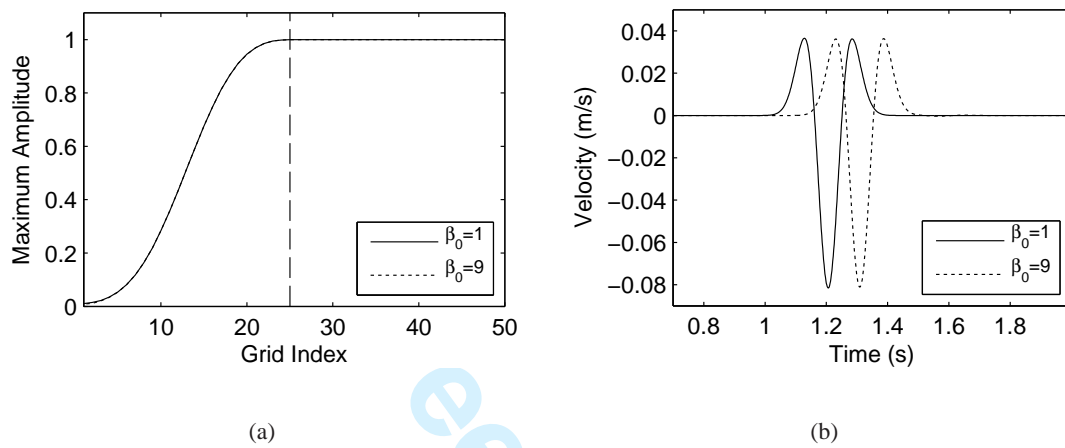


Figure 2: (a) Maximum amplitude distribution for different  $\beta$  values ( $\beta_0 = 1$ , solid line and  $\beta_0 = 9$ , dotted line) for a 25-cell-thick PML of a normal incident plane wave.  $\alpha = 0$  and an optimal  $d$  are used. (b) Velocity seismogram at the grid point 15-cell into the PML for  $\beta_0=1$  (solid line) and  $\beta_0 = 9$  (dotted line). The wave using  $\beta_0 = 9$  arrives later than that using  $\beta_0 = 1$  due to the reduced wave speed by  $\beta_x$ .

Zhang & Shen –

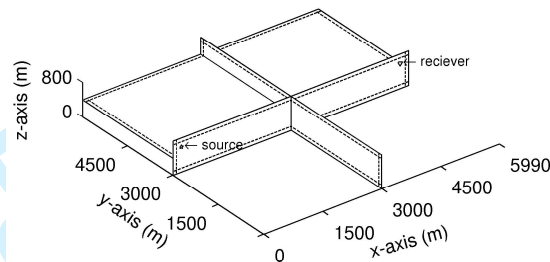


Figure 3: A thin homogeneous 3D slab surrounded by 10-cell-thick PMLs on all six faces (three cross-sections are shown). The PML-interior interfaces are indicated by dashed lines. The medium has a compressional wave speed  $c_p = 3200$  m/s, shear wave speed  $c_s = 1600$  m/s, and density  $\rho = 2200$  kg/m<sup>3</sup>. The grid spacing is 10 m, the total grid number is  $600 \times 600 \times 81$ , and the size of the model is  $5990 \times 5990 \times 800$  m. The star symbol shows the location of the vertical force (200, 3000, 600) m, ten cells away both from the PML-interior interface at the negative  $x$  face and from that at the positive  $z$  face. The triangle symbol indicates the receiver (5790, 3000, 600) m, ten cells away from both the PML-interior interface at the positive  $x$  face and that at the positive  $z$  face.

**Zhang & Shen –**

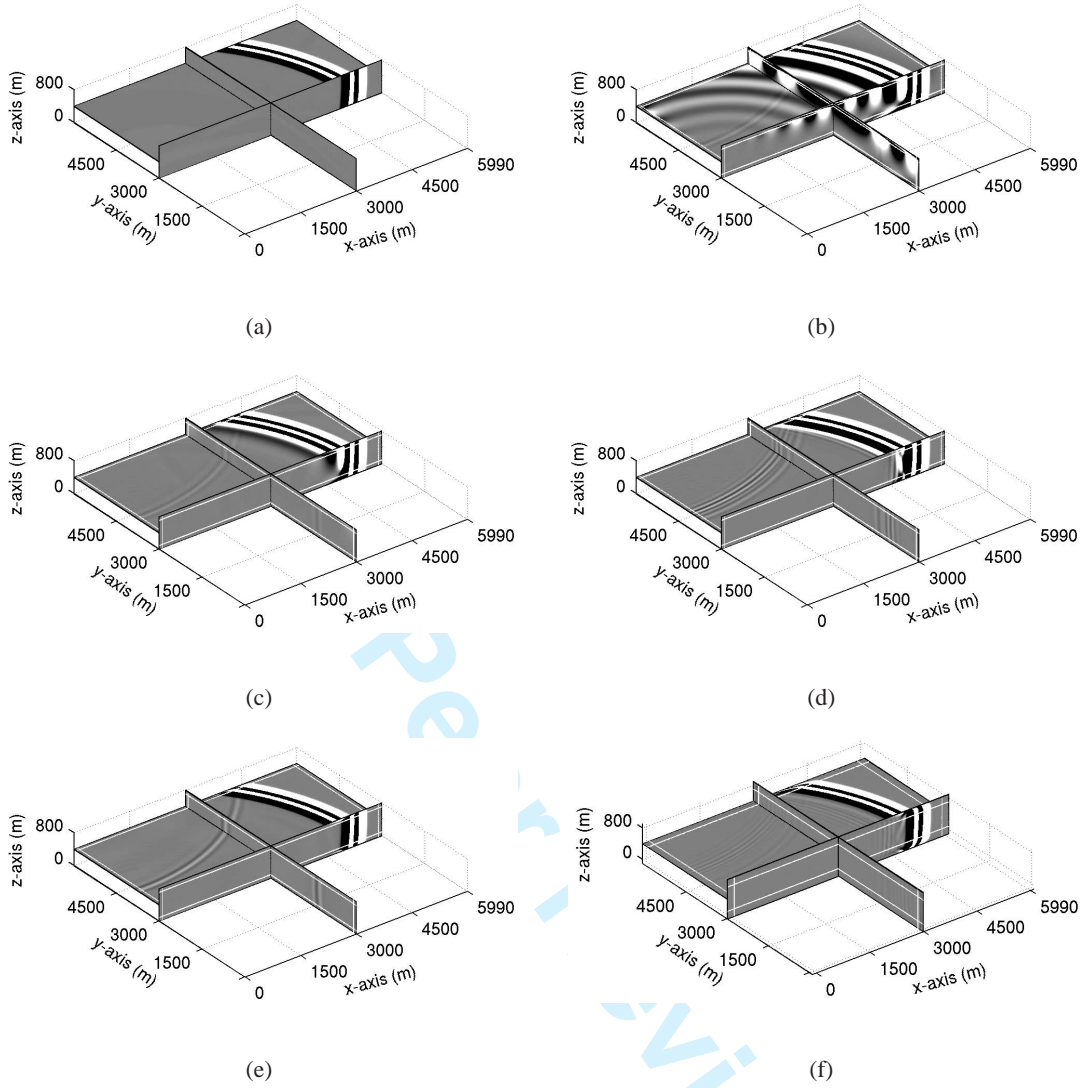


Figure 4: Snapshots of the  $v_z$  component of the thin slab model (Figure 3) at 3.75 s. The color is scaled to 0.1% of the maximum absolute amplitude. White lines are the PML-interior interfaces. (a) Reference solution. (b) Standard PML. (c)  $\alpha_0 = \pi f_c$  and  $\beta_0 = 1$ . (d)  $\alpha_0 = \pi f_c$  and  $\beta_0 = 10$ . (e)  $\alpha_0 = \pi f_c$ ,  $\beta_0 = 7$  and a three times larger  $d_0$ . (f)  $\alpha_0 = \pi f_c$  and  $\beta_0 = 11$  for a 20-cell-thick PML.

Zhang & Shen –

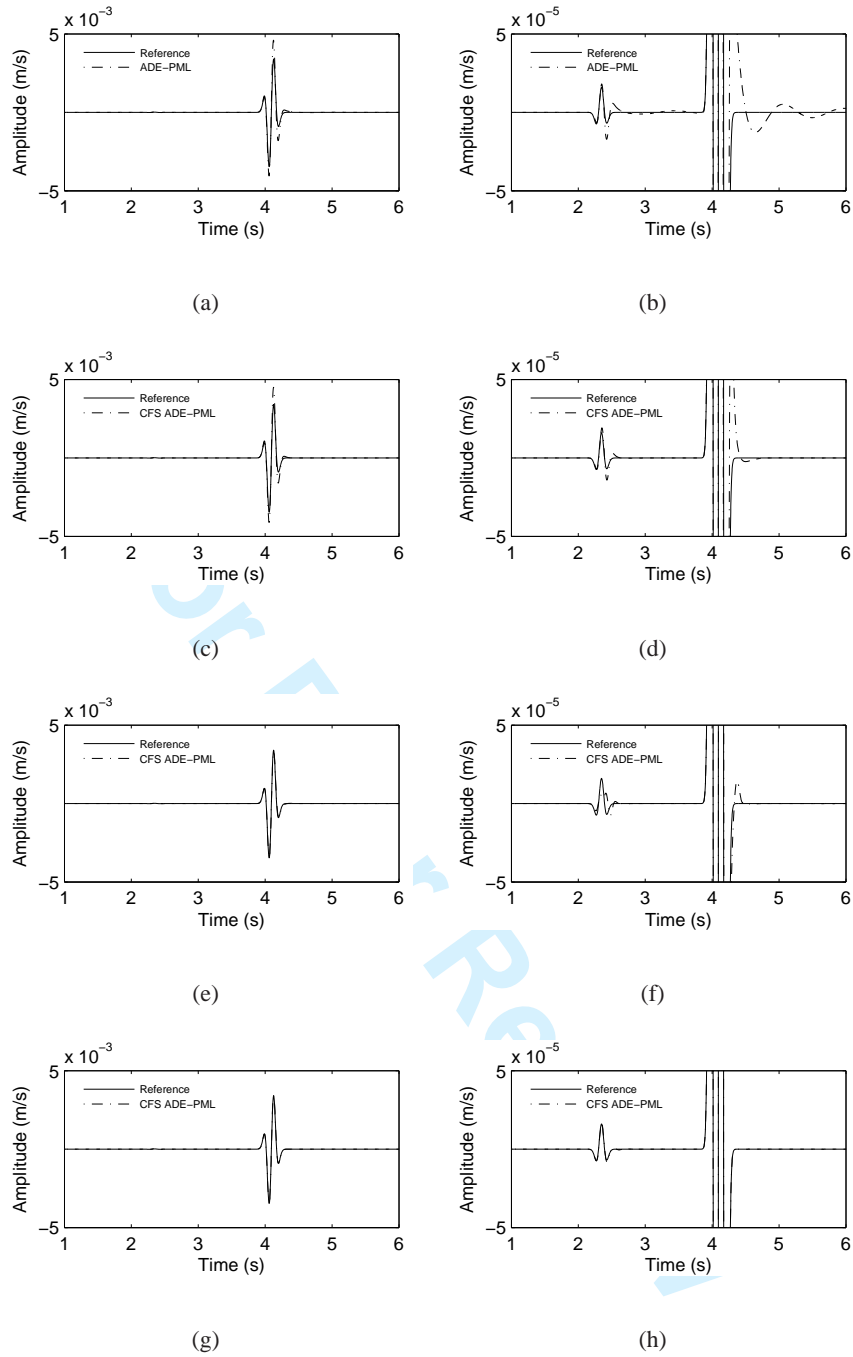


Figure 5: The  $v_z$  seismograms at the receiver shown in Figure 3. The right column shows the same seismograms except that the  $y$  axis is scaled to 1% of that of the left column to highlight the difference. The first arrival in the right column is P wave, which is nearly invisible in the left column. (a)-(b) Standard PML. (c)-(d)  $\beta_0 = 1$  and  $\alpha_0 = \pi f_c$ . (e)-(f)  $\beta_0 = 10$  and  $\alpha_0 = \pi f_c$ . (g)-(h)  $\beta_0 = 7$ ,  $\alpha_0 = \pi f_c$  and a three times larger  $d_0$ . 41

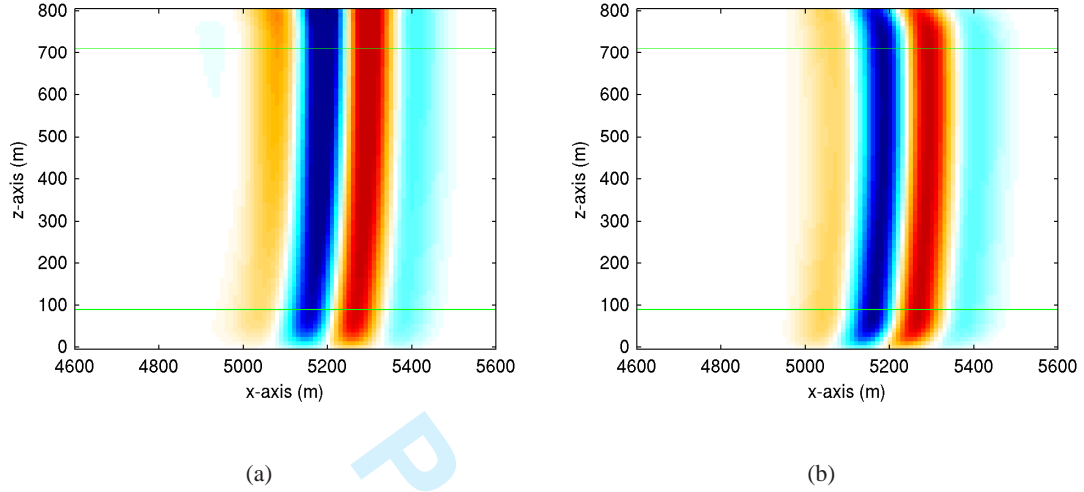


Figure 6: Snapshots of  $v_z$  on the cross-section in the middle of  $y$  axis at 3.75 s. The color is scaled to the same maximum absolute amplitude. Green lines are the PML-interior interfaces. (a)  $\alpha_0 = \pi f_c$  and  $\beta_0 = 1$ . The amplitude of S wave in the upper PML layer is even larger than that in the physical region, which indicates  $\alpha$  does not efficiently absorb this near-grazing propagating body wave. The distribution of the peak amplitude is wider than Figure 6b, which indicates the reflected wave propagates into the physical domain. (b)  $\alpha_0 = \pi f_c$  and  $\beta_0 = 10$ . The wave front is bended towards the normal direction inside both the upper PML layer and the bottom PML layer. The amplitude of S wave exhibits damping in the PML layers.

**Zhang & Shen –**

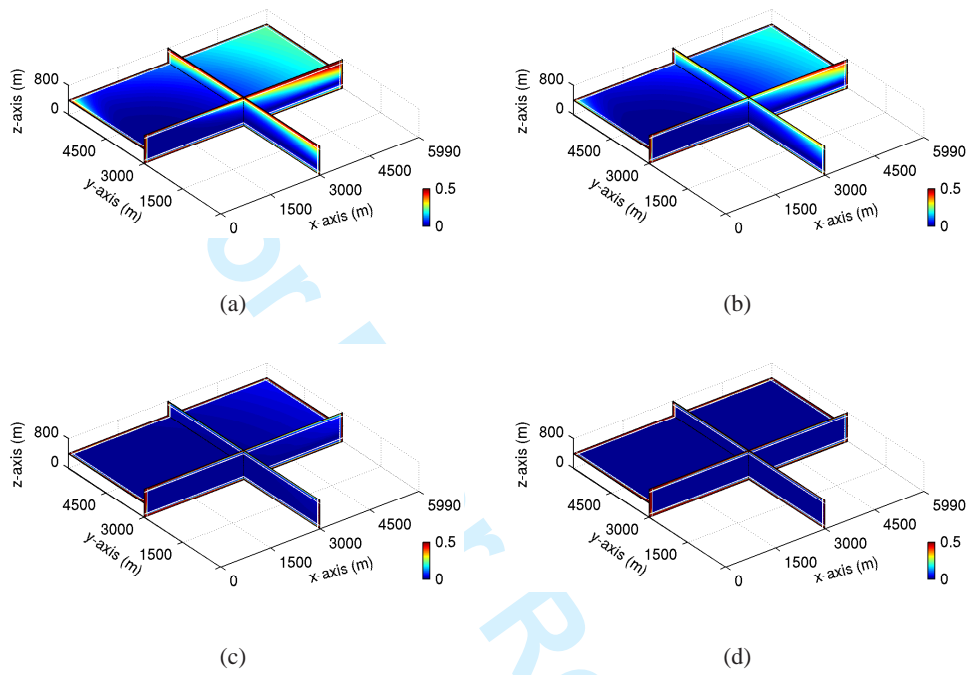


Figure 7: Local error distribution. The color is scaled to 0.5. White lines show the PML-interior interfaces. (a) Standard PML. (b)  $\beta_0 = 1$  and  $\alpha_0 = \pi f_c$ . (c)  $\beta_0 = 10$  and  $\alpha_0 = \pi f_c$ . (d)  $\beta_0 = 7$ ,  $\alpha_0 = \pi f_c$  and a three times larger  $d_0$ .

**Zhang & Shen –**



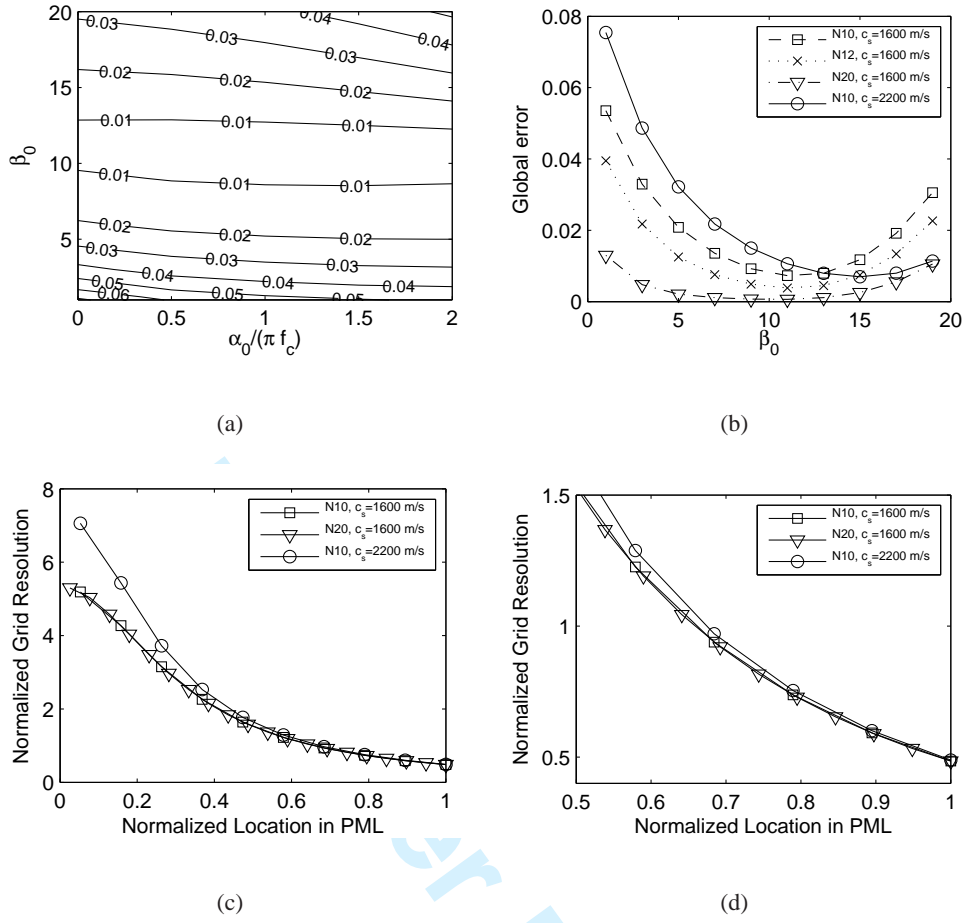


Figure 8: (a) Contours of the global error as a function of  $\alpha_0$  and  $\beta_0$ . The values of  $\frac{\alpha_0}{\pi f_c}$  between 1 to 2 do not significantly affect the overall accuracy. The optimal value of  $\beta_0$  is around  $10 \sim 12$ . (b) Global error variation with respect to  $\beta_0$ , PML thickness  $N$  and S velocities  $c_s$  ( $\alpha_0$  is fixed to  $\pi f_c$ ). The minimal global error is around 11 for different PML thicknesses of 10, 12 and 20 ( $c_s = 1600$  m/s), indicating the optimal  $\beta_0$  is not sensitive to the thickness of the PML. For  $N = 20$  and  $c_s = 2200$  m/s, the optimal  $\beta_0$  is around 15. (c) Normalized points per dominant wavelength variation inside the PML layer for S wave for different PML thickness  $N$  and S wave speed  $c_s$ . (d) The zoom view of Figure 8c to highlight details. The normalized points per dominant wavelength is around 0.5 at the exterior boundary in difference cases.

Zhang & Shen –

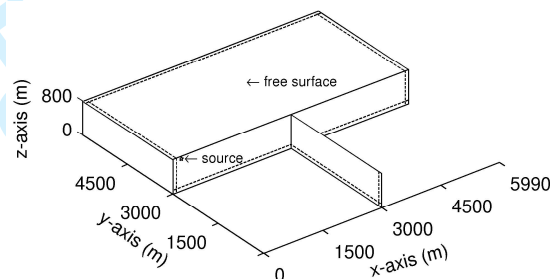


Figure 9: Thin slab model with the free surface. A 10-cell-thick PML (dashed lines) is applied on all the faces except the free surface. The star symbol shows the location of the vertical force (200, 3000, 795) m, ten cells away from the PML-interior interface at the negative  $x$  direction and half cell below the free surface. Other parameters are the same as in Figure 3.

**Zhang & Shen –**

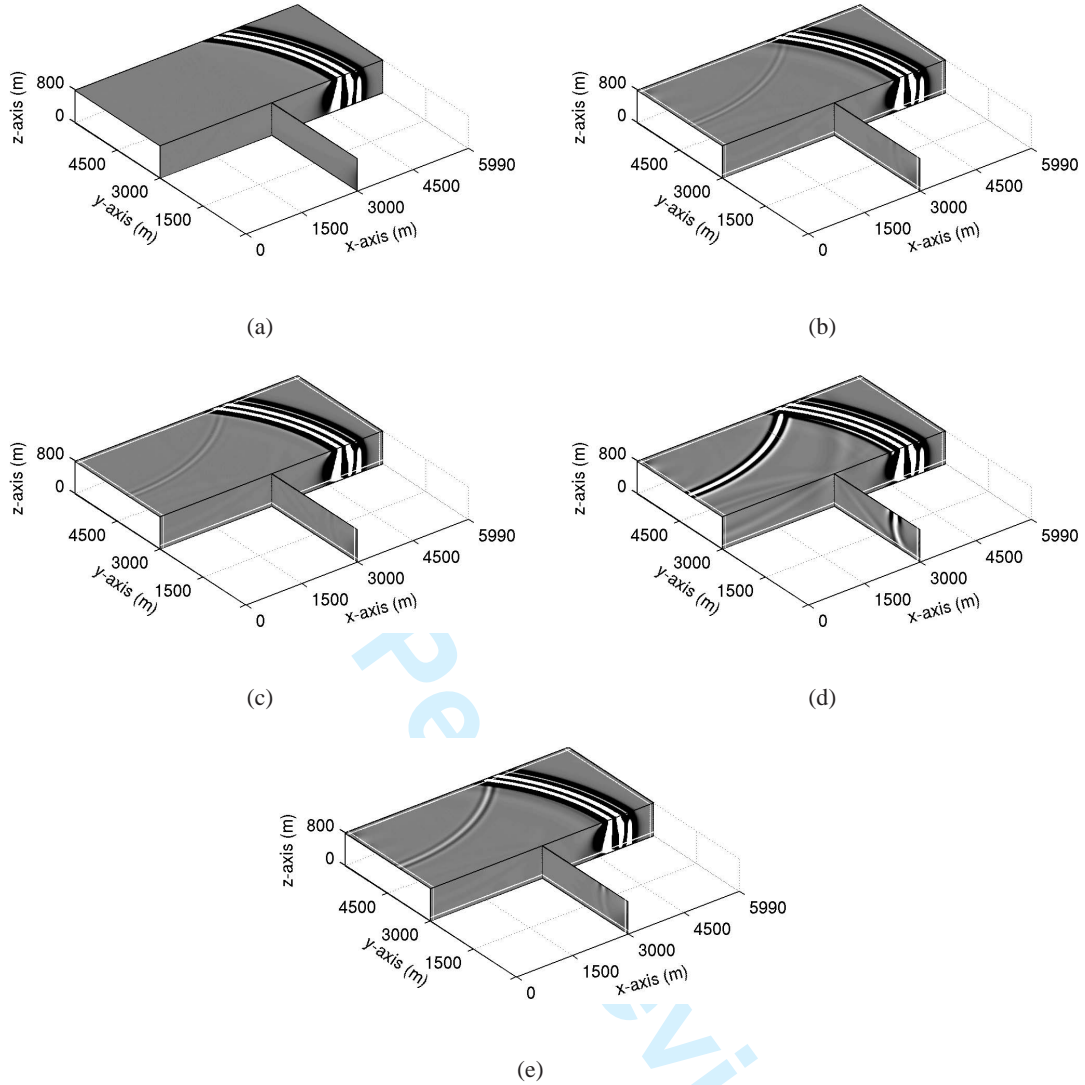


Figure 10: Snapshots of the  $v_z$  component of the free-surface slab model at 3.75 s. The color is scaled to 0.1% of the maximum absolute amplitude. White lines show the PML-interior interfaces. (a) Reference solution. (b) Standard PML. (c)  $\beta_0 = 1$  and  $\alpha_0 = \pi f_c$ . (d) Standard PML without using the modified PML equations 31 and 32. Strong spurious reflected surface waves can be clearly seen. (e) Standard PML with the free surface coincident with the location of the  $\sigma_{xz}$  component.

Zhang & Shen –

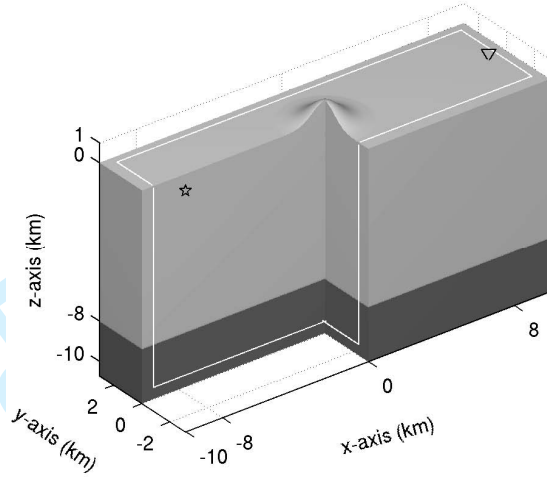


Figure 11: The two-layered model with the free surface topography, which is defined by  $z = 1000 \exp(-r^2/1000^2)$ , where  $r = \sqrt{x^2 + y^2}$ . When  $r > 2000$ m,  $z_0$  is damped to zero by a Gaussian function. The model is 19.95km in length, 6.15km in width and 10.7km in depth (including PML layers). The interface is at  $z = -8$ km, and the medium parameters are  $c_p = 3000$  m/s,  $c_s = 2000$  m/s,  $\rho = 1200$  kg/m<sup>3</sup> for the upper layer and  $c_p = 5000$  m/s,  $c_s = 2500$  m/s,  $\rho = 1800$  kg/m<sup>3</sup> for the lower layer. A 12-cell-thick PML is applied on all the faces except the free surface (white lines). The star symbol shows the location of the vertical force  $(-8000, 0, -500)$  m, and the triangle symbols indicates the receiver's location  $(9000, 0, 0)$  m, seven cells distance to the PML-interior interface at the positive  $x$  face.

**Zhang & Shen –**

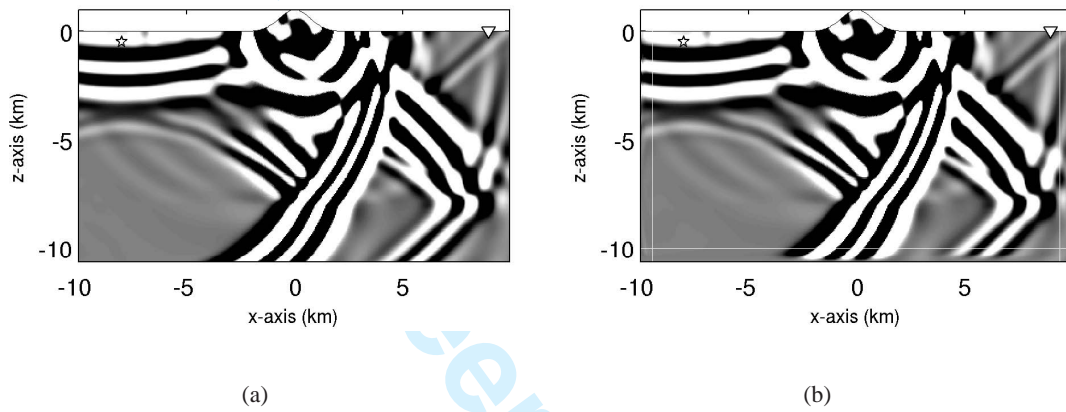


Figure 12: Snapshots of  $v_z$  at 7 s on the  $xz$  cross-section through the middle point of  $y$  axis. The color is scaled to less than 1% of the maximum absolute amplitude. White lines are the PML-interior interfaces. (a) Reference solution. (b)  $\beta_0 = 1, \alpha_0 = \pi f_c$ .

Zhang & Shen –

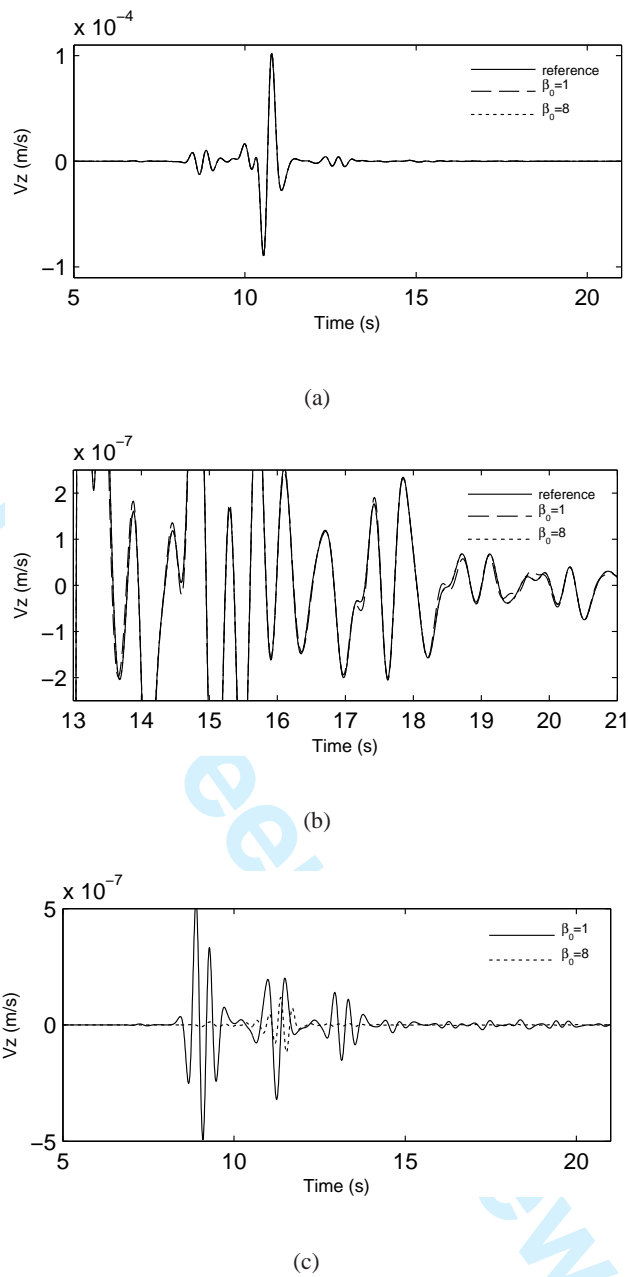


Figure 13: (a) Comparison of seismograms ( $v_z$ ) for the reference (solid line),  $\beta_0 = 1$  (dashed line) and  $\beta_0 = 8$  (dotted line) at the receiver shown in Figure 11. (b) Detailed comparison within the time window 13 ~ 21 s and the amplitude is zoomed in to 0.2% of that in Figure 13a. Difference can be seen between the reference and  $\beta_0 = 1$ . The solution with  $\beta_0 = 8$  overlaps with the reference. (c) Difference between solutions from the CFS ADE-PML and the reference. Solid line shows the difference for  $\beta_0 = 1$ , and dotted line for the optimal  $\beta_0 = 8$ .

# APPENDIX B



# **Moment inversions of earthquakes in the southeast Tibetan plateau using finite-difference strain Green tensor database**

Journal:	<i>Geophysical Journal International</i>
Manuscript ID:	GJI-09-0286.R1
Manuscript Type:	Research Paper
Date Submitted by the Author:	
Complete List of Authors:	Shen, Yang; University of Rhode Island, Graduate School of Oceanography Zhang, Zhigang; University of Rhode Island, Graduate School of Oceanography Zhang, Wei; University of Rhode Island, Graduate School of Oceanography
Keywords:	Computational seismology < SEISMOLOGY, Earthquake source observations < SEISMOLOGY, Seismicity and tectonics < SEISMOLOGY





**Moment inversions of earthquakes in the southeast Tibetan plateau using finite-difference  
strain Green tensor database**

Yang Shen, Zhigang Zhang, Wei Zhang

Graduate School of Oceanography, University of Rhode Island, Narragansett, Rhode Island,  
02882, USA

Accepted *date*. Received *date*; in original form *date*

Abbreviated title: FDSGT Moment tensors of earthquakes in the SE Tibetan plateau

Contact information of the corresponding author:

Yang Shen

Phone: 1-401-874-6848

Fax: 1-401-874-6811

Email: yshen@gso.uri.edu

## SUMMARY

Advance in computation has made routine use of Green functions based on three-dimensional (3D) reference models an increasingly attractive option in earthquake source inversion, as 3D reference models help to isolate source phenomena from propagation effects. This paper extends the source inversion method based on the strain Green tensor (SGT) database from local to regional scales and presents the location and moment-tensor determinations of earthquakes between 2001 and 2004 in the southeast Tibetan plateau. A non-staggered grid finite-difference (FD) method is used to simulate wave propagation in a 3D spherical earth model and construct the SGT database. The FDSGT inversion takes advantage of the source-receiver reciprocity and is well suited for (near) real time earthquake source studies. The SGT database approach makes it computationally efficient to determine the best solution in a grid search surrounding the reference location, by minimizing the waveform misfit of time-windowed first arrivals, teleseismic S waves and surface waves recorded at local to teleseismic distances. The waveforms are bandpass-filtered in four frequency bands to accommodate frequency-dependent waveform quality and time shifted to accommodate errors in the SGTs due to an imperfect reference model. No prior source mechanism solution is needed in the inversion. The new solutions are in general agreement with the global centroid moment tensor solutions, though the two source locations may differ up to 10s km. The moment tensor solutions are not sensitive to uncertainties in lateral source location, partly due to the time shift of waveforms. Inspection of waveform fit in detail suggests that regional stations, the 3D reference model and short-period body waves tend to provide tighter constraints on the locations of the earthquakes. The lowest magnitude of the earthquakes in this study is Mw 4.35. As the crustal velocity model improves,

one may extend useful waveforms to short-period ( $<15$  s) surface waves and be able to apply the FDSGT method to smaller earthquakes at regional scales.

**Key words:** moment tensor inversion, earthquake source mechanism, Tibetan plateau, three-dimensional reference models, strain Green tensor database

1 INTRODUCTION

Accurate source mechanisms are essential in the studies of earthquakes as well as waveform-based investigations of the earth structure. Earthquake focal mechanisms can be determined from first-motion polarities or a combination of first-motion polarities and ratios of maximum P amplitude to maximum S amplitude (e.g., Kisslinger, 1980; Shen et al., 1997; Hardebeck & Shearer, 2003). With the development of digital seismograph, seismologists have also pursued various waveform approaches in source inversion by minimizing the misfit between synthetic and observed body and surface waveforms (e.g., Dziewonski et al., 1981; Nabelek, 1984; Dreger & Helmberger, 1991; Kikuchi & Kanamori, 1991; Zhao & Helmberger, 1994; Zhu & Helmberger, 1996). While source mechanisms of moderate-to-large earthquakes have been routinely determined by modeling teleseismic waveforms (e.g., Dziewonski et al., 1981), characterization of small-to-moderate earthquakes has been uneven geographically and usually incomplete. Yet small-to-moderate earthquakes provide valuable information about regional tectonics due to their relative abundance and broader distribution. Part of the difficulties in applying a generic moment tensor inversion scheme to different areas is the strong lateral variation in crustal structure, which generates complex short-period waves propagating at local and regional distances.

Most earthquake source studies to date utilize one-dimensional (1D) earth model in the calculation of synthetic waveforms or Green functions. To accommodate three-dimensional (3D) structural heterogeneities, segments of body and surface waves are time-shifted before waveform fitting (e.g., Zhao & Helmberger, 1994; Zhu & Helmberger, 1996). In places with highly heterogeneous earth structure, this “cut-and-paste” of waveform segments may not fully account for the complexity of waveform phenomena caused by 3D structures (e.g., focusing and defocusing of waves). One of the major sources of errors in moment tensor inversion is phase skipping between the observed and synthetic waveforms. When traveltimes delays due to 3D velocity heterogeneities are comparable to the wave period, phase skipping becomes a challenging problem.

Advance in computation has made a routine use of 3D Green function in earthquake source inversion an increasingly attractive option. Synthetic waveforms from good 3D reference models account for complex waveform phenomena and reduce phase differences. Liu et al. (2004) determined the source mechanisms of small to moderate earthquakes in southern California using synthetic waveforms calculated with the spectral-element method. Because the derivatives of the source parameters are determined numerically by differentiating synthetics with respect to the source parameters, up to 10 forward simulations are needed for each earthquake (6 moment tensor components, latitude, longitude, depth, and the reference location). When the reference location is far from the true location, the derivatives of the location parameters may not adequately reflect the non-linear variation of waveforms as a function of location. Taking advantage of source-receiver reciprocity, Zhao et al. (2006) introduced the use of strain Green tensors (SGTs) in source inversion based on 3D reference models. In this approach, the SGTs are calculated with a finite-difference code and saved in a database. The

number of forward waveform simulations is three times the number of stations used in source inversion. When the sources outnumber the stations, the Green's tensor or SGT-database approach is more computationally efficient (e.g., Graves & Wald, 2001; Eisner & Clayton, 2001). More importantly since the SGTs are pre-calculated, the SGT-database approach is better suited for (near) real-time source inversion. Zhao et al. (2006) adopted a perturbation approach in source inversion and chose to minimize frequency-dependent arrival time and amplitude anomalies.

In this paper, we extend the SGT-database approach from local scales with waveforms calculated in a Cartesian coordinate (Zhao et al., 2006) to regional and teleseismic scales with waveforms calculated in a spherical coordinate (Zhang et al., in preparation), so we are able to use any combination of local and teleseismic waveforms in source inversion. Instead of frequency-dependent arrival time and amplitude anomalies, we fit multi-frequency filtered and time-shifted waveforms directly. For a given source location, the waveforms are linear functions of the moment tensor elements, which can be solved as a linear inverse problem. To account for perturbations in earthquake source location, we carry out a grid search in the vicinity of the reference location. This is necessary for earthquakes with location errors of 5 km and more, as in the case of most global earthquake catalogs. When the true source location is far from the reference location, the derivative of waveform misfit about the reference location may not be a good approximation to obtain the true location. This in turn affects the waveforms and the moment tensor solution. The grid search is computationally efficient as it involves extracting pre-calculated SGTs in a small volume containing the reference source location from the database. We apply the new method to southeast Tibet in conjunction with a full-wave tomographic imaging effort, as good earthquake source mechanisms are essential for waveform-

based tomographic inversions. An updated upper mantle model (CUB 2.0, Shapiro & Ritzwoller, 2002) is used as the 3D reference model.

## 2 SEISMOTECTONICS OF THE TIBETAN PLATEAU AND SEISMIC DATA

Due to the collision between the Indian and Eurasian plates, the Tibetan plateau has abundant and widely distributed seismic activities. Source mechanism solutions show diverse styles of thrust, normal and strike-slip faulting in the plateau and surrounding areas (e.g., Chen et al., 1981; Zhou et al., 1983; Ni & Barazangi, 1984; Pettersen & Doornbos, 1987; Wu et al., 2004). Using seismic waves recorded by the WWSSN seismographs, Monlar & Lyon-Caen (1989) and Zheng & Suzuki (1993) studied the moment tensors of earthquakes occurred in the region in the 60s to 80s. Randall et al. (1995) used regional seismograms recorded during the 1991-1992 PASSCAL experiment on the Tibetan plateau and estimated the source mechanisms for earthquakes with  $M_w$  ranging from 3.8 to 5.0. Similarly regional earthquake records from other PASSCAL experiments in central Tibetan plateau (Langin et al., 2003) and southern Tibet (de la Torre et al., 2007) were used to determine earthquake source mechanisms. In this study, we focus on earthquakes in the southeastern Tibetan plateau recorded by the HIMNT (de la Torre & Sheehan, 2005), BUTHAN (Velasco et al., 2007), Namche Barwa (Sol et al., 2007), and MIT-China (Xu et al., 2007) experiments between 2001 and 2004. We augment seismic data recorded by portable instruments with records from selected permanent seismic stations at regional and teleseismic distances (Fig. 1).

## 3 MOMENT TENSOR INVERSION

### 3.1 The inverse problem

Following Kikuchi & Kanamori (1991), we represent a general moment tensor  $\mathbf{M}$  as a linear combination of 6 elementary (basis) moment tensors,

$$\mathbf{M} = \sum_{m=1}^6 \alpha_m \mathbf{M}_m \quad (1)$$

where  $\alpha_m$  is the coefficient for the elementary moment tensors and,

$$\mathbf{M}_1 = \begin{bmatrix} 0 & 1 & 0 \\ 1 & 0 & 0 \\ 0 & 0 & 0 \end{bmatrix}; \mathbf{M}_2 = \begin{bmatrix} 1 & 0 & 0 \\ 0 & -1 & 0 \\ 0 & 0 & 0 \end{bmatrix}; \mathbf{M}_3 = \begin{bmatrix} 0 & 0 & 0 \\ 0 & 0 & 1 \\ 0 & 1 & 0 \end{bmatrix};$$

$$\mathbf{M}_4 = \begin{bmatrix} 0 & 0 & 1 \\ 0 & 0 & 0 \\ 1 & 0 & 0 \end{bmatrix}; \mathbf{M}_5 = \begin{bmatrix} -1 & 0 & 0 \\ 0 & 0 & 0 \\ 0 & 0 & 1 \end{bmatrix}; \mathbf{M}_6 = \begin{bmatrix} 1 & 0 & 0 \\ 0 & 1 & 0 \\ 0 & 0 & 1 \end{bmatrix}.$$

We adopt this representation because of an important advantage of using the elementary moment tensors instead of the 6 independent elements of a general moment tensor. Namely, specific solutions (e.g., double couple with a vertical nodal plane or pure deviatoric moment tensor) can be obtained with subgroups of the elementary moment tensors, thus requiring fewer than 6 coefficients or unknowns in the inversion. Let  $b_{nm}^j(t, p)$  denote the displacement component  $n$  at station  $j$  from an elementary moment tensor  $\mathbf{M}_m$  at source location  $p$ .  $b_{nm}^j(t, p)$  can be constructed from the SGTs for the station (Zhao et al., 2006),

$$b_{nm}^j(t, p) = \sum_{i,k=1}^3 [G_{in,k}(p, t; j) M_m^{ik}] * S(t, p)$$

$$= \sum_{i,k=1}^3 [E_{ik}^n(p, t; j) M_m^{ik}] * S(t, p) \quad (2)$$

where  $E_{ik}^n(p, t; j)$  is the strain tensor component  $ik$  at source location  $p$  due to a unit impulsive force acting at receiver  $j$  in the direction  $n$ ,  $M_m^{ik}$  the component  $ik$  of the elementary moment  $M_m$ , and  $S(t, p)$  the source time function.

The displacement  $s_n$  due to a general moment tensor can be expressed as a linear combination of the basis displacements,

$$s_n^j(t, p) = \sum_{m=1}^{N_b} \alpha_m b_{nm}^j(t, p) \quad (3)$$

where  $N_b$  is the number of the elementary moment tensors used (up to 6). For brevity, we hereinafter drop the superscript denoting receiver and the subscript denoting the direction of the displacement and define a least-square misfit function as,

$$E(\mathbf{m}, p) = \frac{1}{A} \sum_{i=1}^N w_i \int_{t_1}^{t_2} [d_i(t) - \sum_{m=1}^{N_b} \alpha_m b_{im}(t, p)]^2 dt \quad (4)$$

where  $d_i(t)$  is the  $i$ -th seismogram,  $N$  the number of time segments,  $t_1$  to  $t_2$  the time window of the waveform,  $\mathbf{m} = [\alpha_1, \dots, \alpha_{N_b}]^T$  the unknown coefficients to be solved, and  $w_i$  a weighting factor to account for waveform quality, station azimuthal distribution and amplitude. The misfit function is normalized by  $A = \sum_{i=1}^N w_i$ . The normal equation for the least-square problem is (Kikuchi & Kanamori, 1991),

$$\sum_{m=1}^{N_b} G_{km} \alpha_m = D_k, \quad \text{for } k=1, \dots, N_b \quad (5)$$

where

$$G_{km} = \sum_{i=1}^N w_i \int [b_{ik}(t, p) b_{im}(t, p)] dt \quad (6)$$



$$D_k = \sum_{i=1}^N w_i \int [b_{ik}(t, p) d_i(t)] dt \quad (7)$$

The solution  $\mathbf{m} = [\alpha_1, \dots, \alpha_{N_b}]^T$  is obtained by singular value decomposition and the moment tensor solution is calculated from equation 1.

### 3.2 The 3D reference model and construction of strain Green's tensor database

One way to select a 3D reference model is to compare the goodness of fit between the observed and synthetic waveforms. We compare CRUST 2.0 (Bassin et al., 2000) and CUB 2.0 (Shapiro & Ritzwoller, 2002) in this study. We extend CRUST 2.0 beneath the Moho with the AK135 model (Kennett et al., 1995) and scale P-wave speed to S-wave speed in CUB 2.0 using a  $V_p/V_s$  of 1.74 in the crust and that of AK135 in the mantle. The density is converted from the density-velocity relationship of Christensen & Mooney (1995). When necessary, we also extend CUB 2.0 to below 400 km depth with AK135. At the reference model selection stage, we use the global centroid moment tensor solutions (GCMT, formerly known as Harvard CMT) of select earthquakes to calculate synthetic waveforms. The band-pass filtered synthetic waveforms of the entire earthquake wave train are cross-correlated with the observed. Fig. 2 shows that on average CRUST 2.0 predicts a much earlier wave train than the observed and more importantly a poor maximum cross-correlation coefficient than CUB 2.0 at all frequency bands. As expected, the correlation coefficients are close to 1 and relatively less scattered at long periods (50-120 s). At periods of 15 s and shorter, the correlation coefficients are highly variable. Since the correlation is dominated by surface waves, which have relatively large amplitudes compared to those of body waves, the highly variable correlation coefficients at short periods indicates that these two models do not accurately represent the real shallow crust.

We select CUB 2.0 as our initial reference model in source mechanism and full-wave tomographic inversions for its overall better performance in the waveform cross-correlation test (Shen et al., 2008). The source mechanism inversion presented in this paper uses a new model derived from CUB 2.0 after the first iteration of full-wave inversion.

To construct the station SGTs to be used in source inversion, we use a non-staggered-grid finite-difference method in the spherical coordinate (Zhang et al., in preparation). Three simulations, one for each orthogonal unit impulsive point force acting at the receiver, are needed for each station used in the source inversion. We select 49 stations at regional and teleseismic distances from the temporary and permanent seismic networks (Fig. 1). Simulations are carried out on three geographic scales: (1) within the southeast Tibetan plateau, (2) at far-regional distances, and (3) teleseismic distances. The finite-difference grid in the regional and far-regional simulations has a grid spacing of  $0.04^\circ$  (latitude),  $0.045^\circ$  (longitude), and 1-6 km (with the small depth interval near the free surface). This yields accurate P wave synthetics at periods great than  $\sim 7$  s and accurate shear and surface wave synthetics at periods greater than  $\sim 10$  s. The moment rate is a Gaussian time function with an effective cutoff frequency below  $\sim 0.5$  Hz and centered at 3 s. Because the synthetics are low-pass filtered to  $\sim 0.13$  Hz, the periods of the waveforms used in the inversion are much longer than the typical source duration of the earthquakes in this study (M 4-6). For larger earthquakes, it may be necessary to use an empirically determined source time magnitude relationship or determine the source-time function in the source inversion. For each simulation, we use 16 cpu cores (AMD Opteron 2218, 2.6 Ghz, 2 GB memory per core) and carry out up to 6 simultaneous simulations on a 104-core cluster. The finite-difference grid in the teleseismic simulations has three times the lateral spacing and twice the vertical spacing of the regional simulations. Thus for teleseismic arrivals, we use only synthetics at periods greater

than 30 s. The SGTs are saved on the same spatial grids ( $0.12^\circ$  in latitude,  $0.135^\circ$  in longitude, and 2 km in depth) within the southeast Tibetan plateau, because all earthquakes studied in this paper are within the southeast Tibetan plateau. The same SGTs are also used to calculate the finite-frequency sensitivity kernels (Zhao et al., 2005; Zhang et al., 2007) in a parallel effort to improve the velocity model by full-wave tomography inversion. For a study just on earthquake moment tensors, one can save SGTs only in the vicinity of the target earthquakes and in finer grids. The SGTs extracted from the database for the inversions of the 23 earthquakes in this study take ~23 GB disk space.

### 3.3 Data Processing

From a list of earthquakes in the southern Tibetan plateau between 2001 and 2004 in the EHB earthquake catalog (E.R. Engdahl, personal communication), we collect earthquake records from the portable and permanent broadband seismic stations in southeastern Tibet and selected stations at far-regional and teleseismic distances (Fig. 1). We remove the instrument response and bandpass filter the records in four frequency bands (0.00833-0.0167, 0.0167-0.0333, 0.0333-0.0667, 0.0667-0.133 Hz). We select the records by their signal-to-noise ratios (SNRs) using an automated process. The signal level is the maximum amplitude of the trace, while the noise level is defined as the amplitude of the trace in the time window between 100 s prior to the earthquake origin time and the first arrival. Those with SNRs greater than a cut-off value (3) are selected for further analysis. Bandpass-filtering allows records useable in one frequency band but noisy in other frequency bands to pass the SNR test. We further select the earthquakes by their geographic distributions and limit our source inversions to earthquakes that are well recorded by at least 5 stations.

#### 3.3.1 Selection of waveforms

Following Zhao & Helmberger (1994), we select two time windows on each seismic record. At regional and far-regional distances, we use the surface wave and the first arrival (Pg, Pnl), though we avoid the first arrival at the upper mantle triplication distance (1400-3000 km). This restriction can be relaxed if seismic records at other distances are insufficient and the benefit of the addition of body waves out-weights the potential downside of an inaccurately modeled complex triplication waveform. At teleseismic distances ( $> 3000$  km), we use the first arrival (P) and S wave. Generally the first arrivals and teleseismic body waves are less affected by shallow heterogeneities and provide relatively consistent waveforms between the synthetics and observed, though they tend to have lower SNRs due to their relatively low amplitude. Long-period (60-120 s) surface waves also provide consistent waveforms. But for smaller earthquakes ( $M < 5$ ), intermediate-period records often have better SNRs.

Because synthetic surface waves from the current reference model do not fit the observed well at short periods (15 s and less, Fig. 2), we limit surface waves to 30 s and longer period in the source inversion. As the velocity model improves, one can increase the bandwidth of useable surface waves to shorter periods. We also exclude the lowest frequency body waves (since they often overlap with surface waves at long period) and only use body wave signals at periods below 60 s. For the first arrival, the length of the time window varies with the frequency band. From the onset of the first arrival to the end of the time window is one full period of the long-period end of the frequency band. This is designed to minimize contributions from later arrivals (e.g., PmP), which are likely less well captured by the reference model.

### 3.3.2 *Waveform weighting and time shift*

The 3D reference model helps to reduce the phase shifts between the observed and synthetics, but significant phase mismatches remain due to errors and unaccounted

heterogeneities in the reference model. As in Zhao & Helmberge (1994), we allow the observed and synthetic waveforms to shift in time and calculate the misfit between the observed and time shifted synthetics. The amount of time shift is determined by waveform cross-correlation and limited within a fraction of the arrival time of the phase. This is equivalent to a prescribed value that varies with distance (Liu et al., 2004). By trial and error, we set the allowable time shift of a body wave to within  $\pm 3\%$  of its travel time. For surface waves, we allow the phase to shift by a larger fraction ( $\pm 5\%$ ). Too large a fraction may lead to phase skip and unreasonably large phase shifts, while too small a fraction does not allow otherwise very similar waveforms to match in time. As the velocity model improves, one may use smaller fractional values, which are expected to generate a stronger gradient in the misfit function.

Since data quality and source-receiver distribution vary greatly from earthquake to earthquake, from station to station, and from frequency band to frequency band, it is often necessary to treat the data by a weighting scheme that takes into account our knowledge of individual data quality. Different researchers may adopt different weighting schemes, making this perhaps the most subjective aspect of source inversion. Though for earthquakes with good azimuthal coverage and high SNR records, weighting is likely non-critical.

The assigned weight in equation 4,  $w_i = w_i^{snr} w_i^{az} w_i^{amp}$ , is composed of weighting for signal noise ratio  $w_i^{snr}$ , station distribution  $w_i^{az}$ , and amplitude  $w_i^{amp}$ . To account for various qualities of seismic arrivals, we assign  $w_i^{snr}=1$  for time windows with SNR between 3-6 and  $w_i^{snr}=2$  for windows with SNR  $> 6$ . The station weight  $w_i^{az}$  is inversely proportional to the number of traces in  $30^\circ$  azimuthal bins to lessen the likelihood that waveforms from a cluster of closely spaced stations dominate the solution. The amplitude weight is inversely proportional to the time

integration of the square of the amplitude of observed waveforms, so body-wave time windows contribute approximately equally to the misfit function.

Partly because waveforms can be shifted in time, the moment tensor solution and the waveform misfit is insensitive to lateral changes in location. Yet for some traces, the onset times of first arrivals can be picked accurately. To integrate this arrival time information into the global optimization of the source solution, we calculate a transformed misfit function by multiplying the weight  $w_i$  with an additional first-arrival-time-related factor after the moment inversion. This posterior factor does not affect the moment inversion at individual grid but helps to select the best amplitude-fitting solutions close to the best location(s) required by the travel times of the reference model. Unlike other weighting factors, it is a function of grid search location  $w_i^{\Delta t}(p) = (1 + |\Delta t_i(p)|)^2 / (1 + aT_i)^2$ , where  $\Delta t$  is the time difference between the onset times of the observed and synthetic first arrivals,  $T$  the travel time of the first arrival, and  $a$  the scaling factor ( $\sim 0.01$ ) to account for a larger uncertainty in  $\Delta t$  at a greater distance due to errors in the velocity model. For traces with no picked first arrival time,  $w_i^{\Delta t}(p) = 1$ . For noise-free synthetics, the picking of the onset of the first arrival involves the detection of the first value deviated from zero (above numerical errors), which is trivial. The onsets of the observed first arrivals are picked by hand (though an automated first-arrival picking scheme can be implemented for routine and quick processing), with the synthetics generated from the SGTs and an explosive source at the EHB earthquake location as guidance for the pick. Since the SGTs are saved at 1 s time interval, we estimate that  $\Delta t$  has an uncertainty of  $\sim 1$  s (For a study just on source mechanisms, one may save the SGTs at much smaller time intervals at the target locations). The traces with first arrival times thus have, as a group, relatively larger weights. As grid search moves away from the best travel-time solution(s), the traces with first-arrival times

have even larger weights. This effectively penalizes solutions that predict the onsets of first arrivals significantly different from the observed and causes the transformed misfit to increase more quickly away from the best solution than that giving no consideration to the onset times of first arrivals. For most earthquakes in this study, this posterior treatment of the global misfit function does not affect the moment tensors, but changes the estimates of the location errors.

**3.4 Inversion procedures**

For a given source location, the synthetics are linear combinations of the elementary moment tensors (equation 3). But waveform varies in a nonlinear fashion as the source location changes. To deal with this linear-nonlinear, moment-tensor-and-location problem, we adopt a grid-search approach, solving the linear problem at each grid in a 3D volume surrounding the reference (EHB) source location. The SGT databases are well suited for this approach, as this involves only extracting SGTs at the target 3D grids. We limit the search to a volume of approximately 91 km x 91 km x 28 km in the latitude, longitude, and vertical directions, respectively, centered on the reference source location. This translates to 7 x 7 x 15 grid points, or 735 moment tensor solutions, one for each grid. Adjustments are made for events with the reference locations near the surface (no search above the free surface). Because of discrete search, the solution has an intrinsic numerical location error of approximately half grid (6.5 km laterally and 1 km vertically), which is comparable to or smaller than the location error caused by inaccurate reference models and the error in the earthquake catalog. As the velocity model improves, it may warrant saving the SGTs at every finite-difference wave simulation grid (~4.4 km laterally and 1 km vertically) or finer grid (by interpolation) in the target volumes of earthquakes.

At each grid, we obtain an initial solution from the normal equations using only longer-period waves (30-60 s and 60-120 s). Only the basis displacements  $b_{nm}^j(t, p)$  for the elementary

1  
2  
3 moment tensors are used (equations 6 and 7) and no synthetic waveforms are required at this  
4  
5 stage. For long-period waves, a small phase shift is less problematic. Because the earthquakes  
6  
7 studied are all tectonic events as opposed to, say, explosions, we solve for pure-deviatoric  
8  
9 moment tensors, so the number of unknown coefficients for the elementary moment tensors is 5.  
10  
11 The deviatoric moment tensor is constructed from the coefficients as in Kikuchi & Kanamori  
12  
13 (1991). After we obtain the initial solution, we construct the synthetics using equation 3. The  
14  
15 time-windowed and bandpass-filtered synthetics are cross-correlated with the observed, and the  
16  
17 synthetics are shifted by the time lag of maximum cross-correlation. We obtain a new moment  
18  
19 tensor solution using the time-shifted synthetics. Since a new moment tensor yields somewhat  
20  
21 different synthetics and different time-shifts, this process is repeated until the solution is stable.  
22  
23 We find the solution usually becomes stable after 2 iterations.  
24  
25  
26  
27  
28

29 After we loop through all the grids, the solution (the moment tensor and grid location) that  
30  
31 yields the minimum misfit is selected as our tentative preferred solution. We then check the  
32  
33 cross-correlation coefficients between the bandpass-filtered, time windowed and shifted  
34  
35 synthetics from the tentative solution and the observed. If all the cross-correlation coefficients  
36  
37 are greater than a prescribed value (0.5), then the tentative solution becomes the final preferred  
38  
39 solution. Otherwise a second and final round of grid search is carried out with the frequency-  
40  
41 time windows having cross-correlation coefficient less than the cutoff value removed from the  
42  
43 inversion. The poor waveform similarity for the best solution in the first round of grid search  
44  
45 can be due to (1) non-stationary random noise that is stronger in the time window than before the  
46  
47 first arrival (SNRs are calculated from the noise level before the first arrival), and (2)  
48  
49 heterogeneities that are not accounted for in the 3D reference models. In either case, if poor-fit  
50  
51 frequency-time windows are not removed from the inversion, they may significantly degrade the  
52  
53  
54  
55  
56  
57  
58  
59  
60



moment tensor solution. Liu et al. (2004) select good data traces based on synthetic waveforms of already good source parameters determined previously in other studies. Our approach provides, in essence, the same quality control on input data without a prior solution.

We estimate the location errors by examining the variation of the misfit function within the grids. We adopt the approach of Sambridge & Kennett (1986) and normalize the misfit function by the misfit of our preferred solution (the minimum misfit). The region that satisfies the confidence limit  $(1-\alpha)$  is

$$\frac{[E(\mathbf{m}) - E(\mathbf{m}^{sol})]}{E(\mathbf{m}^{sol})} \leq \frac{\chi^2_{N_{df}}(1-\alpha)}{N_{df}} \quad (8)$$

where  $E(\mathbf{m}^{sol})$  is the misfit of our preferred solution and  $N_{df}$  the number of degrees of freedom for the chi-squared distribution. Since there are five elementary moment tensors for deviatoric earthquakes and three location parameters (latitude, longitude and depth), the total degree of freedom is 8. Because we allow the synthetics to shift in time in waveform fitting, we do not consider the origin time another degree of freedom, though increasing the degree of freedom to 9 does not significantly change the right hand side. At the one-standard deviation ( $\sigma$ , 68% confidence limit) level,  $\chi^2_8(0.68)/8 = 1.159$  versus  $\chi^2_9(0.68)/9 = 1.156$ . At the 95% confidence limit, the normalized chi-squared values are 1.938 and 1.879, respectively.

In the following section we present examples of the source mechanisms determined from the method outlined above. For events in the GCMT catalog, we compare the waveform fits for the new FDSGT and GCMT solutions.

#### 4 FDSGT MOMENT TENSORS

The October 27, 2001 (Ms 5.5) Yunnan earthquake (event 2001.300.05.35.42 in Supplementary) was recorded by the HIMNT temporary network stations (de la Torre & Sheehan, 2005) and the permanent stations at regional and teleseismic distances (Fig. 3g). Body and surface waves at both regional and teleseismic distances in all frequency bands provide useful constraints on the source parameters, though the SNR for this earthquake is best in the 30-60 s period range (Fig. 3a-d). Approximately  $1/3^{\text{rd}}$  of the frequency-time windows are rejected in the final inversion because of their low SNRs or correlation coefficients calculated before and after the first round of grid search, respectively.

The source locations in the EHB and GCMT catalogs differ by ~50 km (Fig. 3f). For moderate and small ( $M_w < 6.5$ ) earthquakes like this one, the difference in location is unlikely the effects of finite spatial rupture, but dominated by location errors (Smith & Ekstrom, 1997). Our new solution is southeast of the EHB location and southwest of the GCMT solution, though the EHB location is within the one- $\sigma$  uncertainty region defined by waveform misfit and both the EHB and GCMT locations are within the 95% confidence limit. The depth of the preferred solution ( $8 \pm 3$  km) is significantly shallower (at the 1- $\sigma$  uncertainty level) than the GCMT depth (15 km) and the EHB depth ( $16.7 \pm 3.2$  km). The waveform fit at the GCMT and EHB depths (15-17 km) is substantially worse than the fit at the best solution (Fig. 3e). Compared to the traveltimes-based EHB solution and long-period waveform-based GCMT solution, the depth resolution in this study comes from variations in waveform as a function of the event depth and shorter-period body waves used in this study. The above comparison is based on the FDSGT moment tensor solutions at the individual grids. If we use the GCMT moment tensor at the

closest grid to the GCMT location, the waveform misfit is nearly three times larger than that of the best FDSGT solution (1.64 of GCMT versus 0.52 of FDSGT).

Figure 4a shows the lowest misfit solution at each grid-search depth. The solutions at very shallow (2 km) and large ( $> 18$  km) depths are noticeably different from the global best solution. In contrast, a  $\sim 10$  km lateral shift in location does not affect the moment tensor solution significantly (Fig. 4b). This low sensitivity to lateral shift in location is partly due to time-shift in waveform fitting to account for errors in the 3D reference model.

A close comparison of the observed waveforms and the synthetics predicted by the GCMT and our FDSGT solutions reveals that the FDSGT location yields waveforms that are better matched in time. To illustrate this, we zoom in on the first arrivals at station LSA and CHTO, and the teleseismic S wave at station MDJ (Fig. 5). At station LSA, the GCMT and FDSGT synthetics essentially overlap and both are  $\sim 4 \pm 1$  s later than the observed. The delay may result from a  $\sim 3\%$  lower-than-real upper mantle P velocity in the reference model. Since a significant portion of the event to LSA path cuts through the Indian mantle indentor, the velocity anomaly seems possible. At station CHTO, the onset of the first arrival from the FDSGT solution matches fairly well with the observed. Changing the source to the GCMT location (and the GCMT moment tensor), we have an onset of the synthetic first arrival that appears  $\sim 10$  s later than the observed. To fit the arrival, the upper mantle P velocity along the event to CHTO path has to be 8% higher than in the reference model, a value too large to be likely true. At station MDJ, the teleseismic P wave is below the SNR threshold. The synthetic teleseismic S wave from the FDDGT solution arrives slightly later than that of the GCMT solution and fits the observed better in time.

Also shown in Figure 5 are the synthetics of 200 random realizations of the FDSGT solution. In each realization, we take each of the estimated standard deviations for the six moment tensor components and change each component by a random value that follows a normal distribution with the standard deviation for this component. These realizations thus reflect only the uncertainties of the moment tensor components and do not include the uncertainties of the source location. There are two underlying assumptions in this calculation: (1) the waveform misfits are due to random noise, and (2) the moment tensor components are independent. These assumptions are unlikely to be fully true, since part of the waveform misfit is certainly caused by un-modeled velocity heterogeneities and thus not fully random. Nevertheless, the range of variations in the 200 realizations is comparable to the observed misfit in waveforms after time shift (also see Fig. 3), suggesting that the estimated level of uncertainties in the moment tensor solution is correct. Increasing the moment tensor uncertainties by a factor of 2 results in realizations that may be opposite in phase polarity (not shown). On the other hand, reducing the moment tensor uncertainties by a factor of 2 results in a range of waveform variations that is much smaller than the observed. We note that the middle of the S wave train at station MDJ is particularly sensitive to errors in the moment tensor compared to the rest of the waveform. The variation in synthetic waveforms due to uncertainties in the moment tensor together with the estimates of the source location errors can be used to provide proper weighting of the data in waveform-based tomographic inversion.

The June 29, 2002 (Ms 5.5) Qinghai earthquake (event 2002.180.06.54.42 in Supplementary) was also recorded by the HIMNT temporary network stations (de la Torre & Sheehan, 2005) and the permanent stations at regional and teleseismic distances (Fig. 6g). Our new solution is ~25 km south of the EHB and GCMT locations, which are outside of the 95% confidence limit (Fig.

6f). Inspection of the first arrivals at KMI, LSA and the HIMNT stations confirms that the southward shift in location from the reference is required by the data (and the 3D reference model). At  $8\pm 3$  km depth, the new solution is also significantly shallower than the EHB (16.4 km) and GCMT (33 km) estimates (Fig. 6e). Despite the  $\sim 25$  km offset in the lateral locations, the FDSGT and GCMT moment tensors are very similar (Fig. 7), reflecting again the low sensitivity of the moment tensor solutions to lateral shift in source location.

Figure 7 shows a comparison of the FDSGT and GCMT solutions for 13 earthquakes. For most of the earthquakes, the two solutions are in general agreement. One notable exception is the August 18, 2003 earthquake at the eastern Himalayan syntaxis. The GCMT solution shows a strike-slip event at 33 km depth, while our FDSGT solution is a shallow ( $2\pm 16$  km) thrust event.

No all FDSGT solutions are significantly shallower than the GCMT solutions. Four out of thirteen are significantly shallower than the GCMT solutions, one significantly deeper, and the rest within the 95% confidence limit. The one with a FDSGT source depth significantly deeper than the GCMT solution (the July 21, 2003 earthquake, event 2003.202.15.16.37 in Supplementary) has a local minimum near the GCMT depth (15 km), but the global minimum is at  $46.7\pm 3.6$  km depth. This example highlights the benefit of a global optimization approach in earthquake source parameter study, such as grid search. Though if the grid search volume is not large enough for a poor reference location, one may still miss the real solution. A perturbation approach about the reference runs the risk that the solution is trapped at a local minimum.

Also shown in Figure 7 are the FDSGT solutions for 10 additional earthquakes with no corresponding GCMT solutions. de la Torre et al. (2007) analyzed the December 2, 2001 earthquake (2001.336.22.41.14 in Supplementary) along the Himalayan arc in northeast India and identified it as a strike-slip event with P axis trending to the south, a result generally

consistent with our FDSGT determination. A list of the moment tensor solutions and additional waveform fits are available in Supplementary Materials.

## 5 DISCUSSION AND CONCLUSION

We determined source parameters for 23 earthquakes between 2001 and 2004 in the southeast Tibetan plateau, using the SGTs of 49 temporary and permanent seismic stations at regional and teleseismic distances. A 3D reference model based on CUB 2.0 is used in the calculation of the SGTs. Taking advantage of the SGT database, we search the best source location and the corresponding moment tensors in a volume surrounding the reference EHB location. At each location, the moment tensor is determined by minimizing the waveform misfit function of time-windowed first arrivals, teleseismic S waves and surface waves. The waveforms are bandpass-filtered in four frequency bands to accommodate variations in the quality of waveforms at different frequencies. The waveforms are time shifted to accommodate errors in the SGTs due to the imperfect reference model. No prior source mechanism solution is needed in the inversion.

Our FDSGT moment tensor determinations are in general agreement with the GCMT solutions, though there are significant differences for some earthquakes. The differences are likely due to differences in the data used in the GCMT inversion and in this study, in addition to the differences in the Green functions (1D versus 3D reference models). Because waveforms are time-shifted before inversion, the moment tensor solutions are not sensitive to uncertainties in lateral source location, and the FDSGT and GCMT source locations may differ up to 10s km. Inspection of the observed and synthetics in details shows that regional stations, the 3D reference model, and shorter-period body waves in this study tend to provide tighter constraints on the lateral position as well as depth.

1  
2  
3  
4  
5  
6  
7  
8  
9  
10  
11  
12  
13  
14  
15  
16  
17  
18  
19  
20  
21  
22  
23  
24  
25  
26  
27  
28  
29  
30  
31  
32  
33  
34  
35  
36  
37  
38  
39  
40  
41  
42  
43  
44  
45  
46  
47  
48  
49  
50  
51  
52  
53  
54  
55  
56  
57  
58  
59  
60

The benefits of FDSGT moment tensor inversion are likely greatest for small to moderate earthquakes (e.g., the additional earthquakes with no corresponding GCMT solutions in Figure 7), which usually do not generate long-period waves at teleseismic distances, the records used in GCMT solutions. The lowest magnitude of the earthquakes in this study is Mw 4.35, though the method is applicable to smaller earthquakes. We note that the 3D SGT approach is most effective when the model used to represent earth structure predicts significantly better waveform fit than 1D models. The 3D reference model used in this study does not adequately predict short-period (<15 s) surface waves, so only long-period surface waves and intermediate-period body waves are used in the inversion. As the crustal velocity model improves, one may extend the useful surface waves to shorter periods and be able to determine the moment tensors of lower magnitude earthquakes.

**ACKNOWLEDGMENTS**

Financial support for this work has been provided by the U.S. National Science Foundation under Grants EAR-0738779 and the Air Force Research Laboratory under Contract FA8718-06-C-0014. Comments by two anonymous reviewers helped improve the manuscript.

1  
2  
3 **REFERENCES**  
4

- 5 Bassin, C., Laske, G. & Masters, G., 2000. The current limits of resolution for surface wave  
6 tomography in North America, *Eos Trans. AGU*, **81**, F897.  
7  
8  
9  
10 Chen, W.P., Nabelek, J.L., Fitch, T.J. & Molnar, P., 1981. An intermediate depth earthquake  
11 beneath Tibet: Source characteristics of the event of September 14, 1976, *J. Geophys. Res.*,  
12 **86**, 2863-2876.  
13  
14  
15  
16  
17 Christensen, N.I., & Mooney, W.D., 1995. Seismic velocity structure and composition of the  
18 continental crust: a global view, *J. Geophys. Res.*, **100**, 9761–9788.  
19  
20  
21  
22 Dziewonski, A.M., Chou, T.-A., & Woodhouse, J.H., 1981. Determination of earthquake source  
23 parameters from waveform data for studies of global and regional seismicity, *J. Geophys.*  
24 *Res.*, **86**, 2825-2852.  
25  
26  
27  
28  
29 de la Torre, T.L., Monsalve, G., Sheehan, A.F., Sapkota, S., & Wu, F., 2007. Earthquake  
30 processes of the Himalayan collision zone in eastern Nepal and the southern Tibetan plateau,  
31 *Geophys. J. Int.*, **171**, 718-738.  
32  
33  
34  
35  
36 de la Torre, T.L. & Sheehan, A.F., 2005. Broadband seismic noise analysis of the Himalaya  
37 Nepal Tibet seismic experiment, *Bull. Seism. Soc. Am.*, **95**, 1202-1208.  
38  
39  
40  
41 Dreger, D.S. & Helmberger, D.V., 1991. Source parameters of the Sierra Madre earthquake from  
42 regional and local body waves, *Geophys. Res. Lett.*, **18**, 2015-2018.  
43  
44  
45  
46 Eisner, L. & Clayton, R.W., 2001. A reciprocity method for multiple-source simulations, *Bull.*  
47 *Seism. Soc. Am.*, **91**, 553-560.  
48  
49  
50  
51 Graves, R.W. & Wald, D.J., 2001. Resolution analysis of finite fault source inversion using one-  
52 and three-dimensional Green's functions, 1, Strong motions, *J. Geophys. Res.*, **106**, 8745-  
53 8766.  
54  
55  
56  
57  
58  
59  
60



Hardebeck, J.L. & Shearer, P.M., 2003. Using S/P amplitude ratios to constrain the focal mechanisms of small earthquakes, *Bull. Seism. Soc. Am.*, **93**, 2434-2444.

Kennett, B.L.N., Engdahl, E.R. & Buland R., 1995. Constraints on seismic velocities in the Earth from travel times, *Geophys. J. Int.*, **122**, 108-124.

Kikuchi, M. & Kanamori, H., 1991. Inversion of complex body waves-III, *Bull. Seism. Soc. Am.*, **81**, 2335-2350.

Kisslinger, C., 1980. Evaluation of S to P amplitude ratios for determining focal mechanisms from regional network observations, *Bull. Seism. Soc. Am.*, **70**, 999-1010.

Langin, W.R., Brown, L.D., & Sandvol, E.A., 2003. Seismicity of central Tibet from project INDEPTH III seismic recordings, *Bull. Seism. Soc. Am.*, **93**, 2146-2159.

Liu, Q., Polet, J., Komatitsch, D., & Tromp, J., 2004. Spectral-element moment tensor inversions for earthquakes in southern California, *Bull. Seism. Soc. Am.*, **94**, 1748-1761.

Molar, P. & Lyon-Caen, H., 1989. Fault plane solutions of earthquakes and active tectonics of the Tibetan plateau and its margins, *Geophys. J. Int.*, **99**, 123-153.

Nabelek, J.L., 1984. Determination of earthquake source parameters from inversion of body waves, Ph.D. Thesis, MIT, Cambridge, Massachusetts.

Ni, J. & Barazangi, M., 1984. Seismotectonics of the Himalayan collision zone: Geometry of the underthrusting Indian plate beneath the Himalaya, *J. Geophys. Res.*, **89**, 1147-1163.

Pettersen, O. & Doornbos, D.J., 1987. A comparison of source analysis methods as applied to earthquakes in Tibet, *Phys. Earth. Planet. Int.*, **47**, 125-136.

Randall, G.E., Ammon, C.J., & Owen, T.J., 1995. Moment tensor estimation using regional seismograms from a Tibetan Plateau portable network deployment, *Geophys. Res. Lett.*, **22**, 1665-1668.

- Sambridge, M.S. & Kennett, B.L.N., 1986. A novel method of hypocenter location, *Geophys. J. R. astr. Soc.*, **87**, 679-697.
- Shapiro, N.M. & Ritzwoller, M.H., 2002. Monte-Carlo inversion for a global shear velocity model of the crust and upper mantle, *Geophys. J. Int.*, **151**, 88-105.
- Shen, Y., Forsyth, D.W., Conder, J. & Dorman, L.M., 1997. Investigation of microearthquake activity following an intraplate teleseismic swarm on the west flank of the Southern East Pacific Rise, *J. Geophys. Res.*, **102**, 459-475.
- Shen, Y., Zhang, W., Ren, Y. & Liang, X., 2008. Imaging the crust and upper mantle in the southern and southeastern Tibetan plateau: A three-dimensional full-wavefield approach, *Eos Trans. AGU*, **89**(53), Fall Meet. Suppl., Abstract T11E-06.
- Smith, G.P. & Ekstrom, G., 1997. Interpretation of earthquake epicenter and CMT centroid locations, in terms of rupture length and direction, *Phys. Earth Planet. Int.*, **102**, 123-132.
- Sol, S., Meltzer, A., Burgmann, R., van der Hilst, R.D., King, R., Chen, Z., Koons, P.O., Lev, E., Liu, Y.P., Zeitler, P.K., Zhang, X., Zhang, J. & Zurek, B., 2007. Geodynamics of the southeastern Tibetan plateau from seismic anisotropy and geodesy, *Geology*, **35**, 563-566.
- Velasco, A.A., Gee, V.L., Rowe, C., Grujic, D., Hollister, L.S., Hernandez, D., Miller, K.C., Tobgay, T., Fort, M. & Harder, S., 2007. Using small, temporary seismic networks for investigating tectonic deformation: brittle deformation and evidence for strike-slip faulting in Bhutan, *Seism. Res. Lett.*, **78**, 446-453.
- Wu, J., Ming, Y. & Wang, C., 2004. Source mechanism of small-moderate earthquakes and tectonic stress field in Yunnan province, *ACTA Seism. Sinica*, **17**, 509-517.

Xu, L., Rondenay, S. & van der Hilst, R.D., 2007. Structure of the crust beneath the Southeastern Tibetan Plateau from teleseismic receiver functions, *Phys. Earth Planet. Int.*, doi:10.1016/j.pepi.2007.09.002.

Zhang, Z., Shen, Y. & Zhao, L., 2007. Finite-frequency sensitivity kernels for head waves, *Geophys. J. Int.*, **171**, 847-856, doi:10.1111/j.1365-246X.2007.03575x.

Zhao, L., Chen, P. & Jordan, T. H., 2006. Strain Green tensor, reciprocity, and their applications to seismic source and structure studies, *Bull. Seism. Soc. Am.*, **96**, 1753-1763, doi:10.1785/0120050253.

Zhao, L. & Helmberger, D.V., 1994. Source estimation from broadband regional seismograms, *Bull. Seism. Soc. Am.*, **84**, 91-104.

Zhao, L., Jordan, T. H., Olsen, K. B. & Chen, P., 2005. Fréchet kernels for imaging regional Earth structure based on three-dimensional reference models, *Bull. Seismo. Soc. Am.*, **95**, 2066-2080.

Zheng, S. & Suzuki, Z., 1993. Moment tensors of earthquakes in and near the Tibetan plateau and their scaling law, *ACTA Seism. Sinica*, **6**, 365-377.

Zhou H.j, Liu, H.-L. & Kanamori, H., 1983. Source processes of large earthquakes along the Xianshuihe fault in southwestern China, *Bull. Seism. Soc. Am.*, **73**, 537-551.

Zhu, L. & Helmberger, D.V., 1996. Advancement in source estimation techniques using broadband regional seismograms, *Bull. Seism. Soc. Am.*, **86**, 1634-1641.

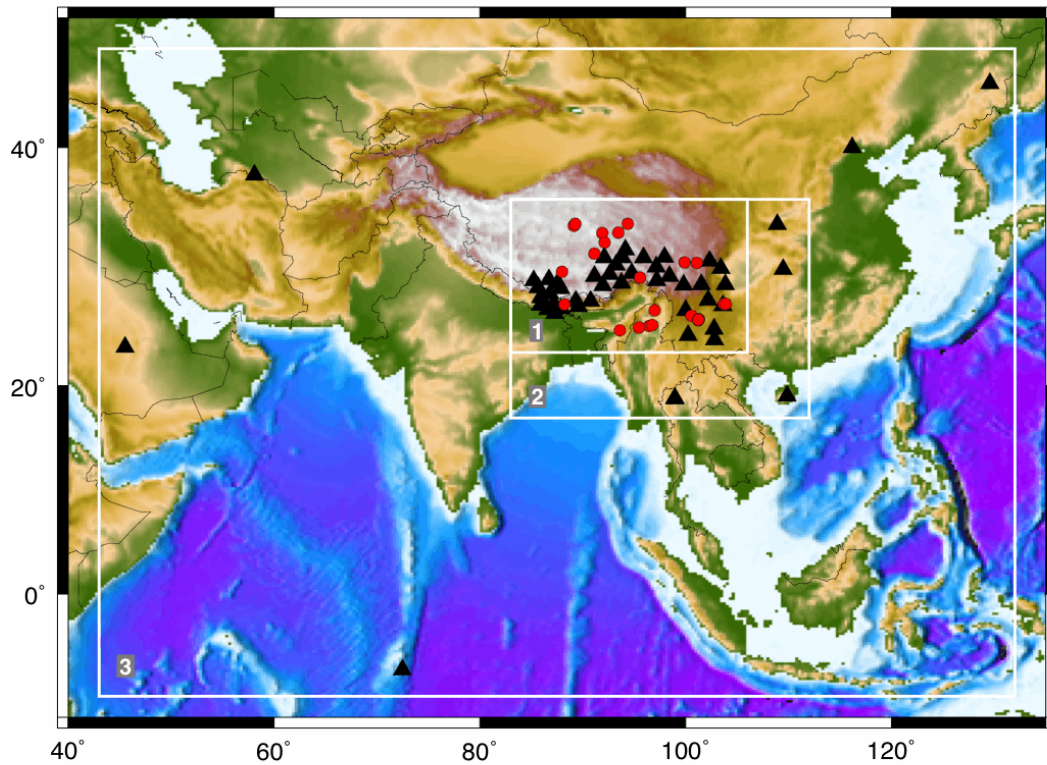


Figure 1. Distributions of the broadband seismic stations used in source inversion (triangles) and the earthquakes studied (dots). White rectangles outline the wave simulation models at (1) regional, (2) far-regional, and (3) teleseismic scales.

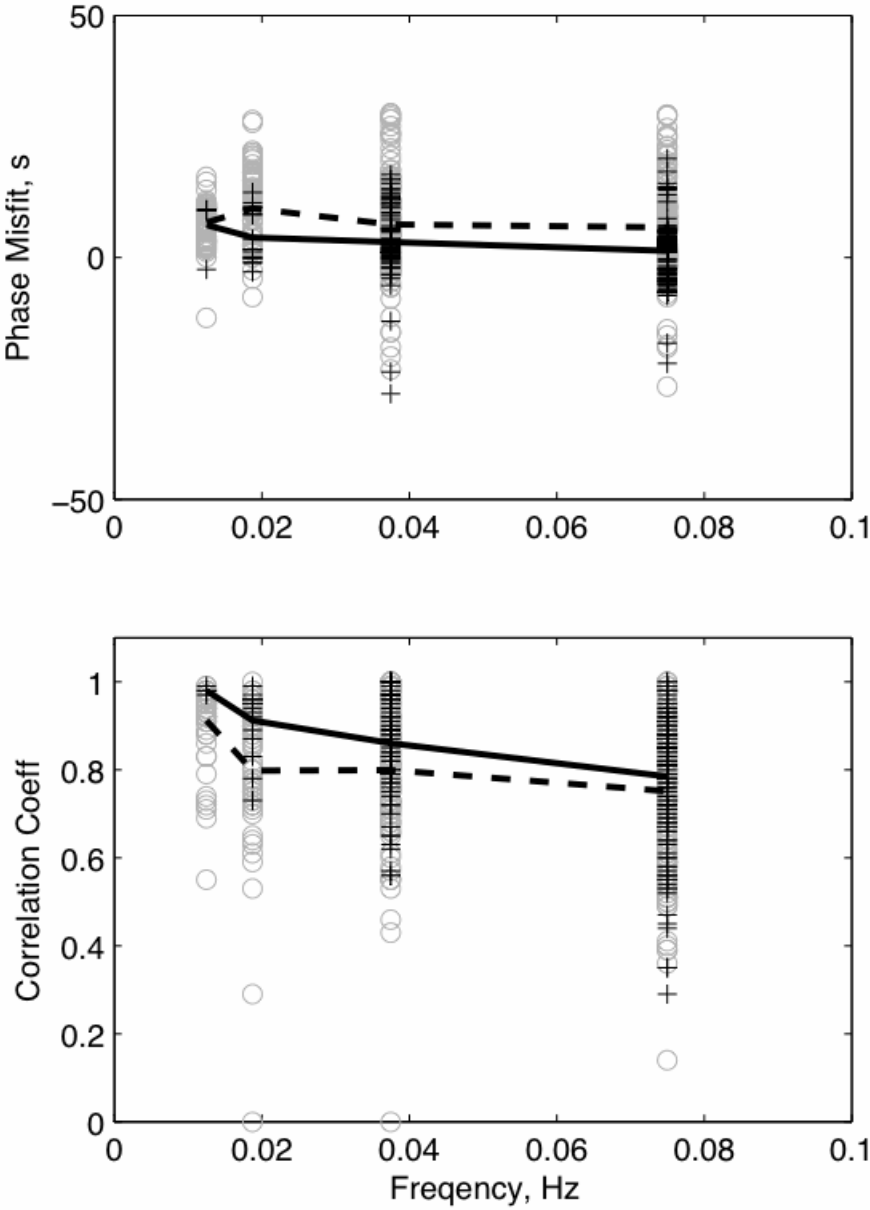


Figure 2. Phase delays and maximum cross-correlation coefficients between the observed and synthetic waveforms at four frequencies. The CRUST 2.0 model predicts a larger average phase delay and lower maximum cross-correlation coefficient (dashed lines) than the CUB 2.0 model (solid lines). The individual CRUST 2.0 values (circles) are also more scattered than the CUB 2.0 predictions (crosses). The GCMT moment tensor for this August 24, 2004 earthquake is used in the calculation of the synthetics.



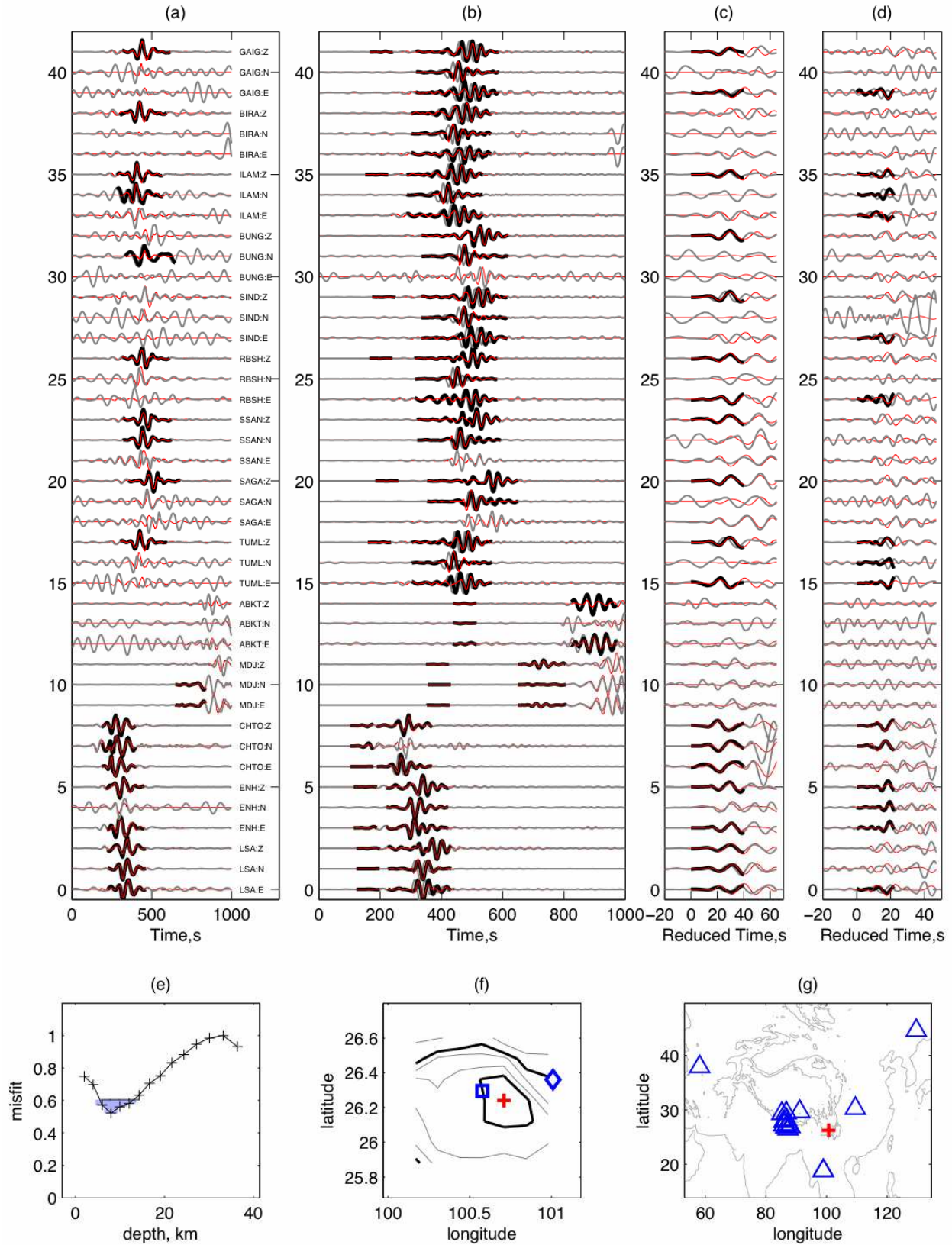


Figure 3. (a-d) Bandpass-filtered observed waveforms (thick gray lines) are compared with the synthetics for the best source solution (red lines). The frequency bands are, from left to right, 0.00833-0.0167, 0.0167-0.0333, 0.0333-0.0667, and 0.0667-0.167 Hz. Dark thick lines are time-shifted observed waveforms used in the final inversion. For the first arrivals (in c and d), the time is reduced to align the arrivals within the time window. The amplitude is normalized by individual trace. (e) Normalized waveform misfit as a function of depth. Crosses mark the grid-search depths. The shaded region indicates the 1- $\sigma$  confidence limit. (f) Contours of various confidence limits at the depth of the global best solution (8 km for this event). The cross marks the FDSGT location, the square the EHB location, and the diamond the GCMT location. From the innermost contour surrounding the FDSGT solution, the contours are the 68% (1- $\sigma$ , dark line), 80%, 90%, 95% (2- $\sigma$ , dark line), and 99% confidence limits. (g) Triangles and cross mark the stations used in the source inversion and the event, respectively. Gray contours follow the sea level, and 2000 and 4000 m elevation.

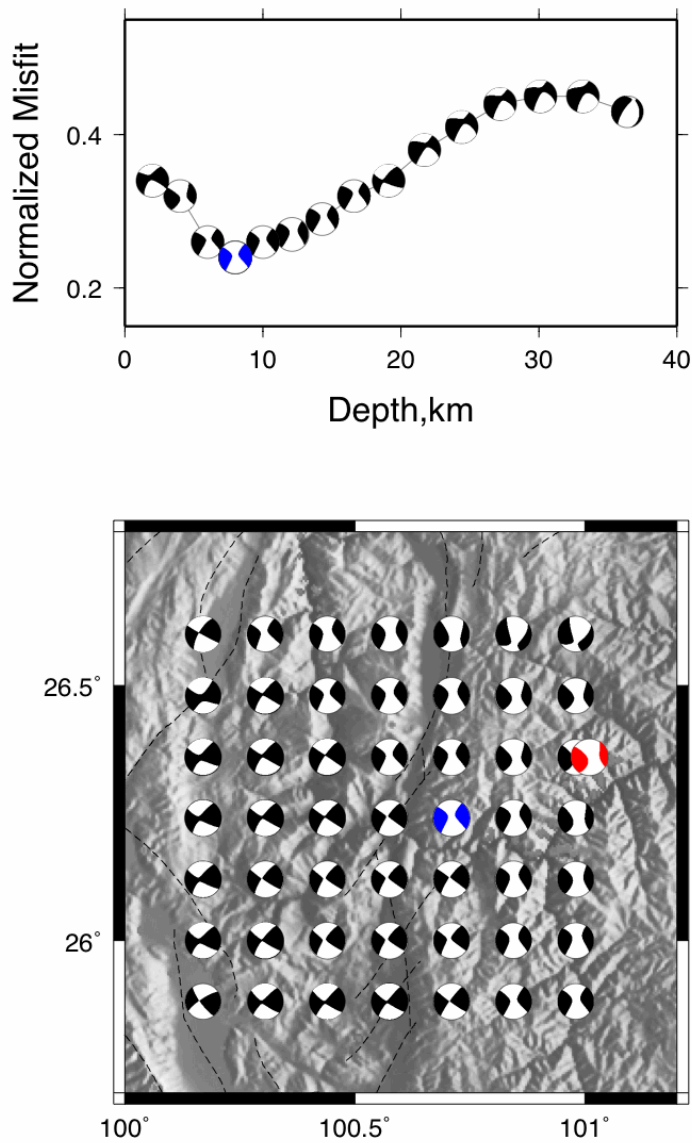


Figure 4. Variations of the best moment tensor solution as a function of depth (upper panel) and lateral locations at the global best solution depth (lower panel). The global best solution is shown as the blue-and-white beach ball. The GCMT solution (red-and-white beach ball) is drawn for comparison. The background is shaded topographic relief with known fault traces marked by dashed lines.



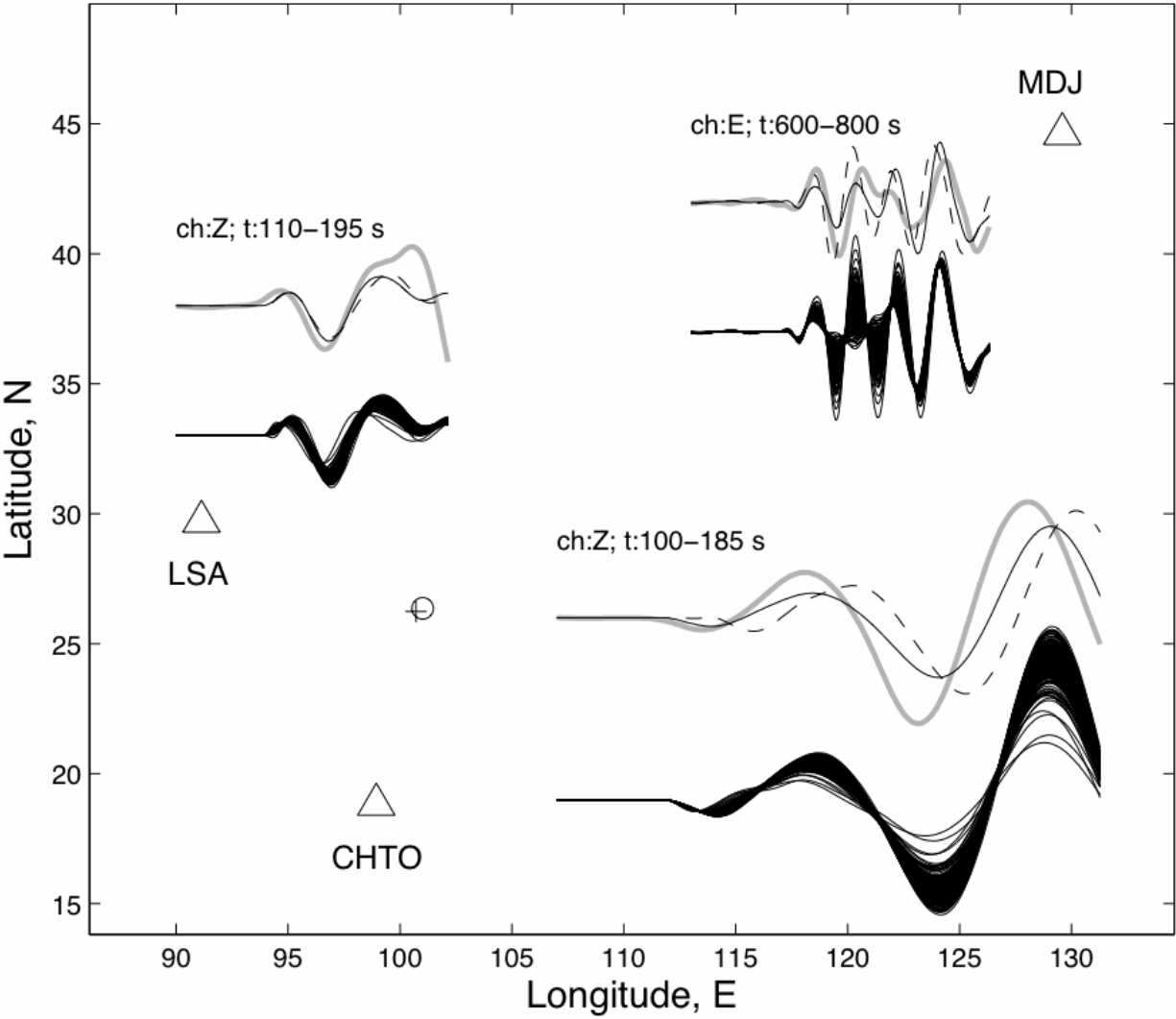


Figure 5. A comparison of the observed waveforms (thick gray lines) and the synthetics for the FDSGT (solid) and GCMT (dashed) solutions at stations LSA, CHTO and MDJ (triangles). The 200 random realizations of the FDSGT solution are plotted below the observed waveforms to show the range of waveform variation due to uncertainties in the moment tensor solution. The waveforms have been filtered between 0.01667-0.0333 Hz, but not shifted in time. The cross and circle near 26° latitude and 101° longitude are the FDSGT and GCMT locations, respectively. The channel and time window (after the earthquake origin) are marked above the waveforms.

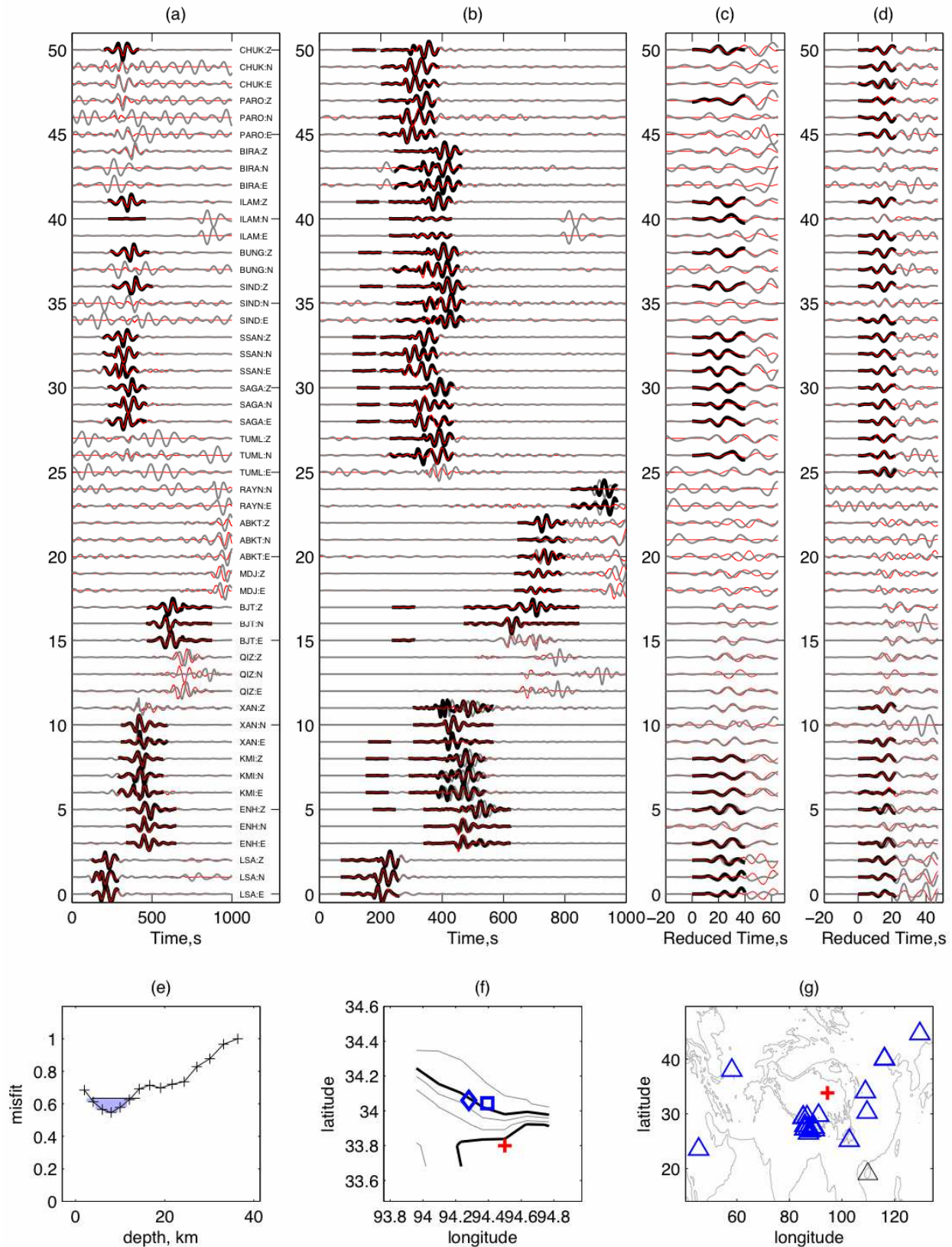


Figure 6. Same as Fig. 3, except for the June 29, 2002 earthquake.

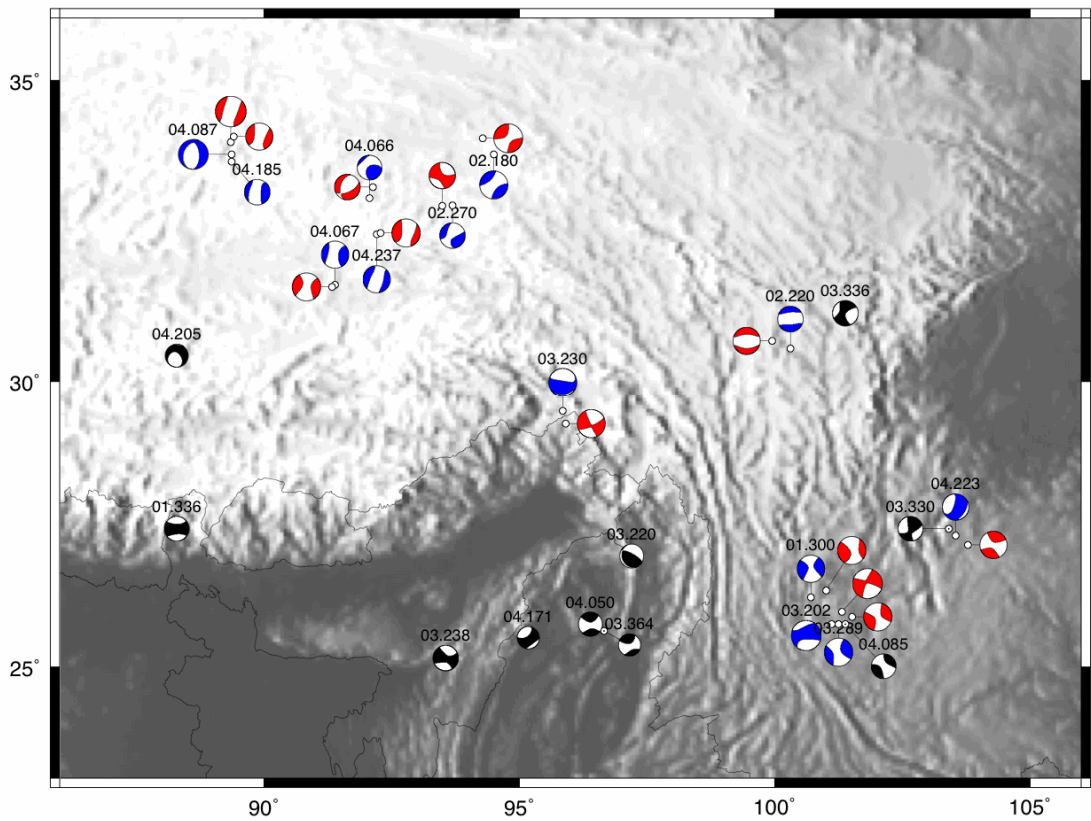


Figure 7. A comparison of the FDSGT (white-and-blue symbols) and GCMT (white-and-red symbols) solutions for 13 earthquakes in the southeast Tibetan plateau. The numbers above the FDSGT solution denote the year and Julian day of the earthquake. Also plotted are the source mechanisms of 10 additional earthquakes without GCMT solutions (black-and-white symbols).

## SUPPLEMENTARY MATERIALS

### Moment tensor solutions based on finite-difference strain Green tensor databases

The following list contains the source locations and moment tensors of 23 earthquakes in the southeast Tibetan plateau. It uses two lines for each earthquake.

*First line: Event ID, location, time and moment magnitude. Numbers stand for the positions of the variables in the line, which are separated by space.*

- 1 Event ID in the format of year.Julian-day.hour.minite.second
- 2-4 EHB latitude and longitude in degree, and depth in kilometer
- 5-6 Latitude and one standard deviation in degree
- 7-8 Longitude and one standard deviation in degree
- 9-10 Depth and one standard deviation in kilometer
- 11 Time with respect to the reference time in second
- 12  $M_w$  as defined in Dahlen and Tromp (1998, eq.5.91)

*Second line: Moment tensor components*

- 1-12 The six moment-tensor elements:  $M_{rr}$ ,  $M_{tt}$ ,  $M_{pp}$ ,  $M_{rt}$ ,  $M_{rp}$ ,  $M_{tp}$ , each followed by its one standard error. The subscript r denotes up, t south, and p east.
- 13 The exponent shared by all the moment-tensor elements and their standard errors. An exponent of 23 stands for  $10^{23}$  dyne-cm.

2001.300.05.35.42 26.295 100.578 16.7 26.240 0.120 100.710 0.068 8.00 3.05 -1.38 5.39  
-1.81e+00 1.54e+00 -1.37e+01 2.75e+00 1.55e+01 2.28e+00 2.38e+00 1.07e+00 8.01e-01 1.57e+00 -4.37e+00 1.99e+00 23  
2001.336.22.41.14 27.281 88.236 20.9 27.440 0.000 88.290 0.068 6.00 6.55 -3.18 4.83  
1.07e+00 2.02e-01 -2.56e+00 2.82e-01 1.49e+00 1.97e-01 -1.79e-01 3.91e-01 1.43e-01 1.64e-01 -1.30e-01 1.15e-01 23  
2002.180.06.54.42 34.043 94.393 16.4 33.800 0.060 94.500 0.270 8.00 4.05 -1.11 5.45  
-7.15e+00 8.55e-01 4.93e+00 1.00e+00 2.22e+00 5.19e-01 -8.56e-01 8.81e-01 -1.37e+00 3.84e-01 1.75e+01 8.57e-01 23  
2002.220.11.42.07 30.862 99.889 35.0 30.560 0.000 100.305 0.068 16.64 1.23 -0.21 4.99  
-3.09e+00 7.71e-02 4.17e+00 1.15e-01 -1.08e+00 8.51e-02 -4.55e-01 7.45e-02 9.03e-03 2.73e-02 4.83e-01 3.45e-02 23  
2002.270.17.14.40 33.324 93.484 35.0 32.960 0.000 93.690 0.068 50.34 22.76 1.82 4.93  
-1.04e+00 2.33e-01 -4.69e-01 4.67e-01 1.51e+00 4.04e-01 -1.38e+00 2.61e-01 -1.24e-01 1.01e-01 2.43e+00 4.77e-01 23  
2003.202.15.16.37 25.990 101.288 35.0 25.760 0.000 101.115 0.067 54.14 7.22 -0.74 5.91  
4.09e+01 4.00e+01 -8.24e+01 5.29e+01 4.15e+01 3.46e+01 4.05e+01 4.43e+01 -1.30e+01 2.09e+01 -4.23e+01 3.12e+01 23  
2003.220.09.59.24 26.738 97.003 6.4 26.960 0.000 97.200 0.202 6.00 5.05 0.26 4.70  
7.32e-01 6.30e-02 -3.21e-01 6.76e-02 -4.11e-01 2.47e-02 -1.05e+00 1.24e-01 4.97e-01 7.33e-02 4.50e-01 2.95e-02 23

1	
2	
3	2003.230.09.03.02 29.564 95.574 16.1 29.480 0.120 95.850 0.338 2.00 15.60 -5.34 5.49
4	6.41e+00 1.32e+00 -9.35e+00 1.41e+00 2.94e+00 4.90e-01 -1.98e+01 2.55e+01 3.74e+00 3.35e+00 -1.09e+00 7.60e-01 23
5	
6	2003.238.20.54.17 24.973 93.619 45.3 25.160 0.120 93.555 0.337 46.67 23.60 0.34 4.92
7	6.51e-01 2.14e-01 -2.78e+00 3.47e-01 2.13e+00 2.74e-01 -1.26e-01 9.51e-02 6.26e-01 7.26e-02 1.66e+00 2.73e-01 23
8	
9	2003.289.12.28.11 25.917 101.234 35.0 25.760 0.060 101.250 0.135 50.34 11.23 -2.90 5.56
10	-5.03e+00 2.13e+00 -1.80e+01 4.21e+00 2.30e+01 3.63e+00 3.13e+00 9.80e-01 -4.27e+00 9.48e-01 -1.68e+01 2.51e+00 23
11	
12	2003.330.13.39.00 27.311 103.726 35.0 27.440 0.000 103.410 0.068 54.14 5.91 0.07 4.87
13	5.20e-01 1.95e-01 9.96e-01 3.27e-01 -1.52e+00 2.63e-01 5.68e-01 1.25e-01 -8.00e-01 1.47e-01 -1.88e+00 2.99e-01 23
14	
15	2003.336.23.26.51 30.816 101.078 35.0 31.160 0.060 101.385 0.135 62.16 17.48 -1.73 5.01
16	1.44e-01 2.31e-01 2.83e+00 3.53e-01 -2.98e+00 2.67e-01 7.81e-01 1.57e-01 1.35e+00 1.09e-01 -2.41e+00 4.94e-01 23
17	
18	2003.364.20.59.49 25.381 96.469 35.0 25.640 0.060 96.660 0.068 19.09 13.24 -1.14 4.35
19	-6.24e-02 5.20e-02 3.34e-01 1.02e-01 -2.71e-01 8.76e-02 1.47e-01 2.77e-02 2.19e-03 1.38e-02 2.39e-01 8.17e-02 23
20	
21	2004.050.09.11.42 25.473 96.776 35.0 25.760 0.060 96.390 0.338 46.67 22.76 -2.03 4.73
22	-2.25e-01 7.07e-02 1.59e+00 2.65e-01 -1.37e+00 2.56e-01 2.97e-01 5.67e-02 -8.84e-02 2.56e-02 2.58e-01 3.13e-01 23
23	
24	2004.066.11.54.43 33.298 91.892 35.0 33.080 0.000 92.070 0.203 30.13 6.01 -0.66 4.85
25	5.43e-01 2.90e-01 -1.61e-01 5.38e-01 -3.82e-01 4.54e-01 -1.35e+00 1.74e-01 -1.08e+00 2.78e-01 1.59e+00 3.30e-01 23
26	
27	2004.067.13.29.44 31.581 91.153 4.4 31.640 0.000 91.395 0.068 10.00 3.05 -0.48 5.30
28	-4.02e+00 2.03e+00 -7.24e+00 2.61e+00 1.13e+01 1.64e+00 1.47e-01 1.88e+00 -3.87e+00 1.43e+00 3.49e+00 8.68e-01 23
29	
30	2004.085.21.15.01 25.953 101.220 35.0 25.760 0.060 101.385 0.067 50.34 11.23 -0.61 4.82
31	-5.55e-01 1.51e-01 -8.91e-03 3.27e-01 5.64e-01 2.90e-01 1.24e-01 1.04e-01 3.57e-01 7.37e-02 -2.04e+00 3.68e-01 23
32	
33	2004.087.18.47.29 33.912 89.128 10.7 33.800 0.060 89.370 0.270 8.00 2.00 1.48 5.83
34	-6.05e+01 2.02e+01 -4.49e-01 2.54e+01 6.09e+01 1.54e+01 1.31e+01 2.47e+01 -3.02e+01 1.99e+01 1.15e+01 6.64e+00 23
35	
36	2004.171.10.24.53 25.264 95.499 35.0 25.520 0.180 95.175 0.202 24.37 18.75 0.24 4.41
37	1.32e-01 2.22e-02 -1.95e-01 3.34e-02 6.37e-02 2.49e-02 -2.46e-01 1.28e-02 -1.55e-01 7.80e-03 -3.92e-01 3.05e-02 23
38	
39	2004.185.14.10.48 34.054 89.276 35.0 33.680 0.060 89.370 0.202 16.64 22.76 -1.63 4.99
40	-2.41e+00 2.06e-01 -1.36e+00 3.76e-01 3.77e+00 3.15e-01 3.54e-01 1.83e-01 -1.80e+00 4.05e-01 9.88e-01 2.17e-01 23
41	
42	2004.205.01.25.31 30.080 88.010 4.9 30.440 0.120 88.290 0.068 8.00 3.00 -0.94 4.50
43	-3.87e-01 3.82e-01 -1.17e-01 4.18e-01 5.04e-01 1.69e-01 4.70e-01 5.72e-01 -2.62e-01 1.52e-01 1.47e-01 2.27e-01 23
44	
45	2004.223.10.26.15 27.310 103.887 12.6 27.320 0.000 103.545 0.067 19.09 9.02 1.71 5.19
46	2.85e+00 1.62e+00 1.07e+00 2.16e+00 -3.92e+00 1.42e+00 -1.53e+00 6.18e-01 -5.65e+00 8.81e-01 -3.71e+00 8.63e-01 23
47	
48	2004.237.10.05.33 32.537 92.137 3.4 32.480 0.060 92.205 0.135 8.00 5.32 -1.18 5.30
49	-8.97e+00 8.16e-01 -1.98e+00 1.23e+00 1.10e+01 9.17e-01 1.67e+00 7.77e-01 4.82e-01 1.28e+00 4.83e+00 3.82e-01 23
50	
51	
52	
53	
54	
55	
56	
57	
58	
59	
60	



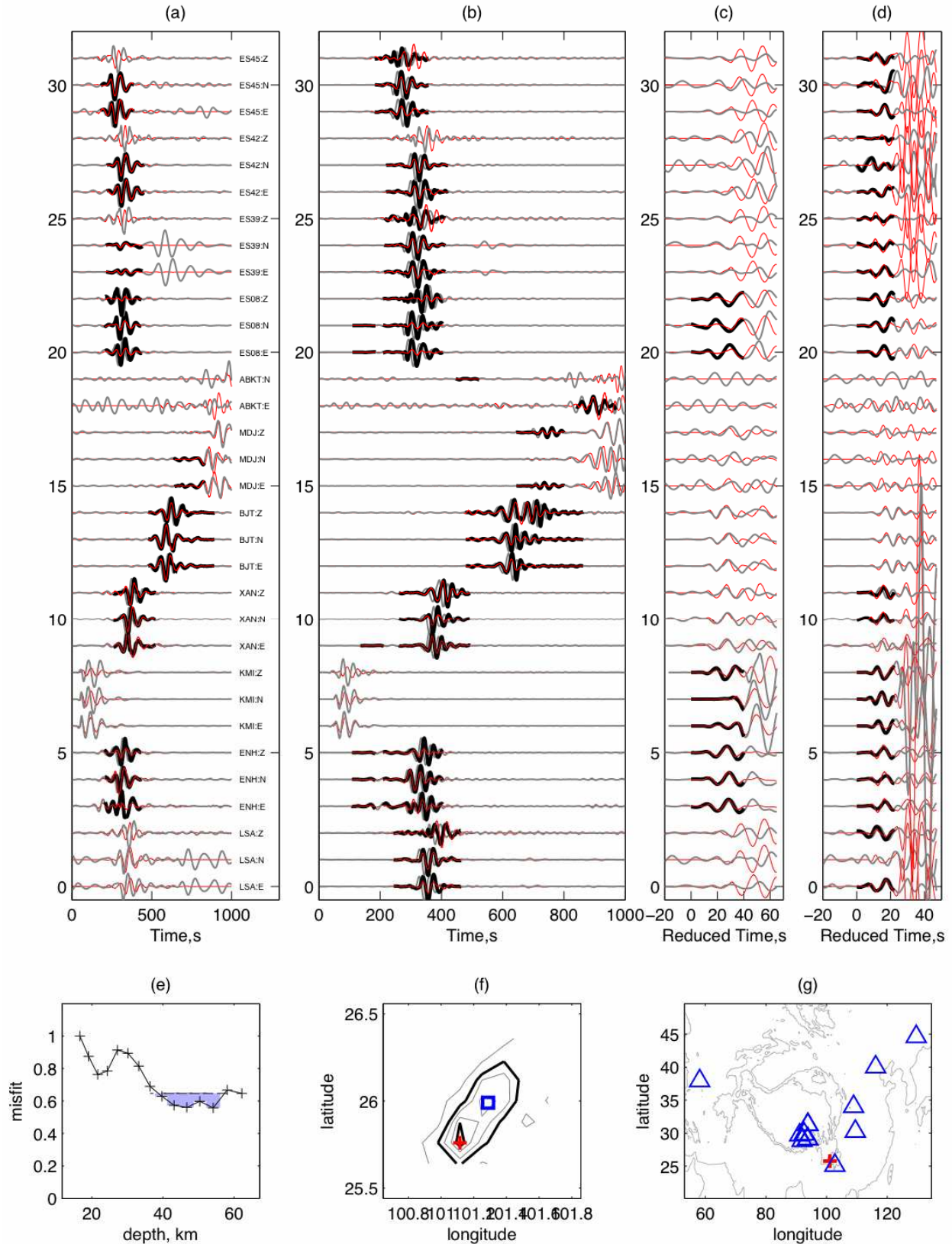


Figure S1. Same as Fig. 3, except for the July 21, 2003 earthquake (2003.202.15.16.37).

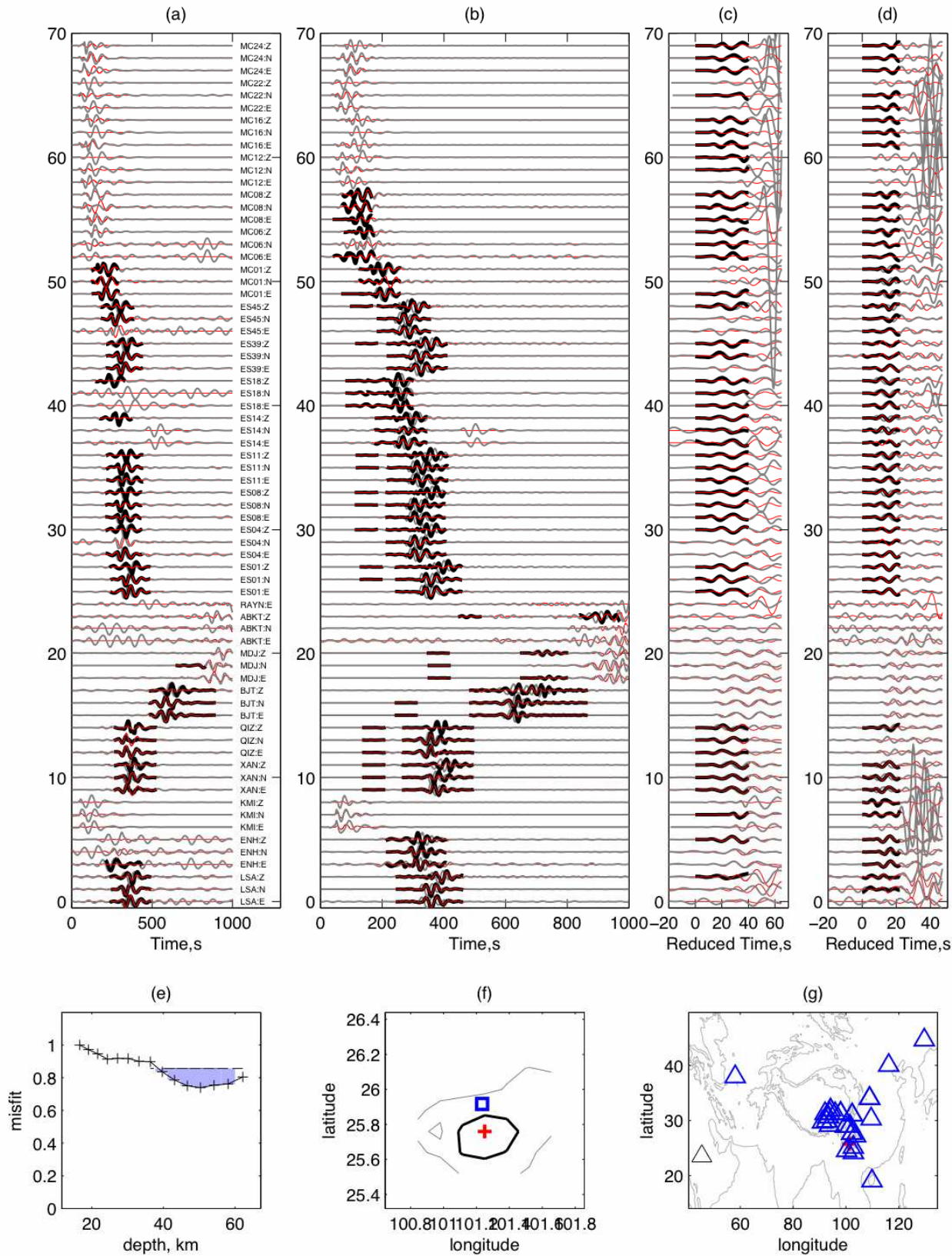


Figure S2. Same as Fig. 3, except for the October 16, 2003 earthquake (2003.289.12.28.11).



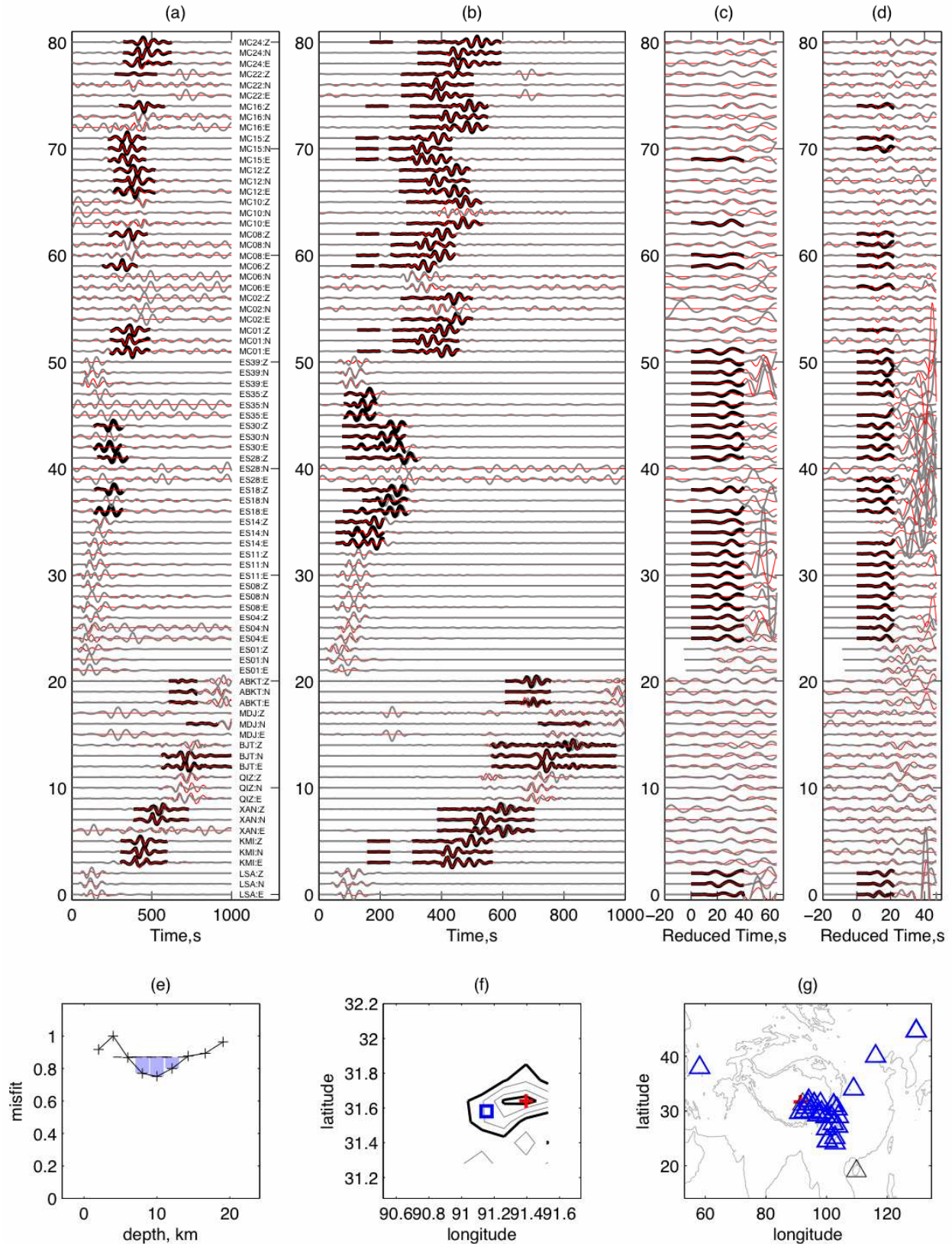


Figure S3. Same as Fig. 3, except for the March 7, 2004 earthquake (2004.067.13.29.44).



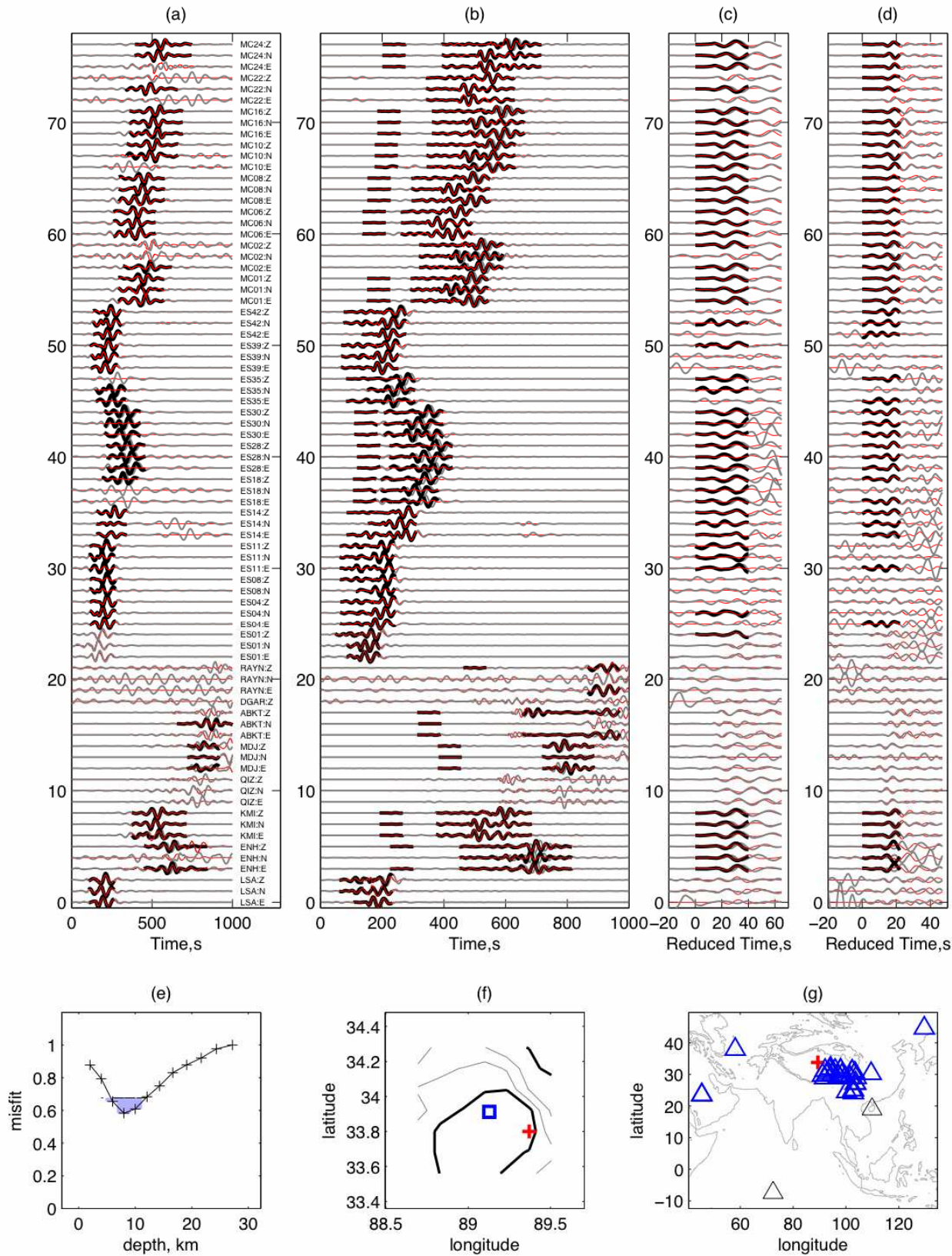


Figure S4. Same as Fig. 3, except for the March 28, 2004 earthquake (2004.087.18.47.29).

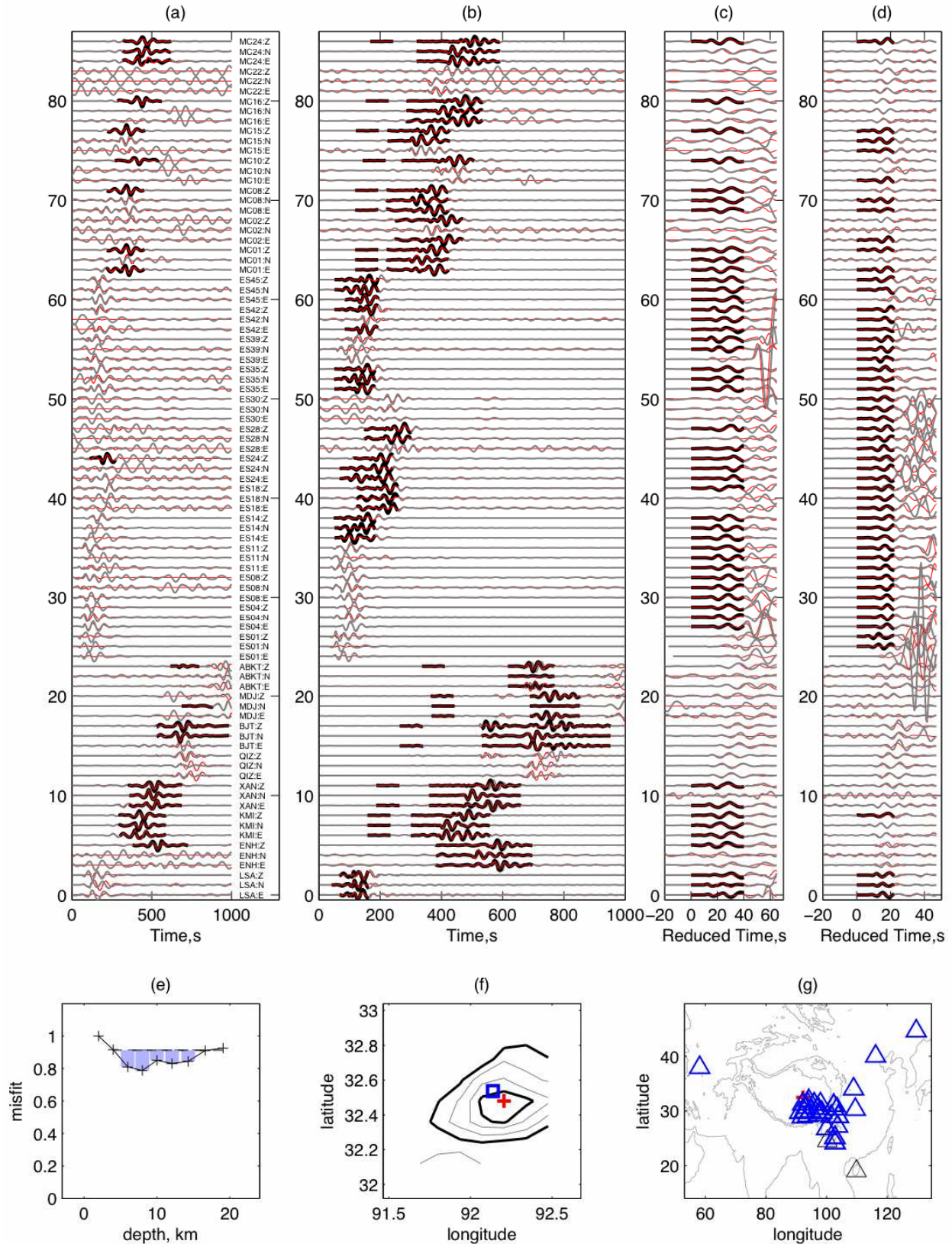


Figure S5. Same as Fig. 3, except for the August 24, 2004 earthquake (2004.237.10.05.33).

# APPENDIX C



# Cross-dependence of finite-frequency compressional waveforms to shear seismic wave speeds

Zhigang Zhang and Yang Shen

Graduate School of Oceanography, University of Rhode Island, Narragansett, RI 02882, USA. E-mail: zzhang@gso.uri.edu

Accepted 2008 April 29. Received 2008 April 28; in original form 2008 March 7

## SUMMARY

Seismic tomography has been one of the primary tools to image the interior of the earth and other elastic structures. To date the inversions of compressional ( $P$ ) and shear ( $S$ ) wave speeds have been carried out separately under the assumption that  $P$  traveltimes are affected only by the  $P$  wave speed of the elastic media and  $S$  traveltimes by the  $S$  wave speed. Using numerical and analytical solutions, we show that for finite-frequency seismic waves,  $S$  wave speed perturbations may have significant effects on  $P$  waveforms. This suggests that when waveform-derived traveltime and amplitude anomalies are used in tomographic inversions, the  $P$ -wave measurements should be related to not only  $P$  wave speed perturbations but also  $S$  wave speed perturbations.

**Key words:** Seismic tomography; Computational seismology; Theoretical seismology; Wave scattering and diffraction; Wave propagation.

## INTRODUCTION

For many years, seismologists have made fundamental discoveries about the earth's interior, using rays to describe the propagation of  $P$  and  $S$  seismic waves. However, with the increasing need for more accurate images of the earth structure at fine resolution, the limitations of ray theory become problematic. Several recent studies have developed a new theory that describes the sensitivities, or Fréchet kernels, of the traveltimes and amplitudes of finite-frequency seismic waves to perturbations in the properties of wave-propagation media (Dahlen *et al.* 2000; Zhao *et al.* 2000, 2005; Tromp *et al.* 2005). For a finite-frequency wave, the sensitivities to the elastic and anelastic properties are in general distributed in a 3D volume surrounding the ray path. Numerical experiments have demonstrated that, within the limit of Born approximation, the finite-frequency theory represents the propagation of realistic seismic waves more accurately than ray theory when the scales of wave speed heterogeneities are smaller than the Fresnel zones of the waves (Hung *et al.* 2000; Baig *et al.* 2003; Yang & Hung 2005; Zhang *et al.* 2007).

To date the inversions of  $P$  and  $S$  wave speeds have been carried out separately under the assumption that  $P$  traveltimes are affected only by the  $P$  wave speed of the elastic media and  $S$  traveltimes by the  $S$  wave speed (e.g. Dziewonski & Anderson 1984; Grand 1987; Zhao *et al.* 1992; van der Hilst *et al.* 1997). With the approximations of only forward scattering of body wave and far field, Dahlen *et al.* (2000) considered that only  $P$ -to- $P$  scattering off a compressional wave speed heterogeneity and like-type  $S$ -to- $S$  scattering off a shear wave speed heterogeneity are significant. Although several studies have documented the scattering of wave field by an arbitrary heterogeneity (Wu & Aki 1985) and have calculated the sensitivity kernels with the near-field terms or in a full-wave approach (Favier *et al.* 2004; Tromp *et al.* 2005; Zhao *et al.* 2005; Liu & Tromp

2006), the assumption that the propagation of  $P$  or  $S$  waves depends solely on the  $P$  or  $S$  wave speed structure, respectively, has remained unchanged in the applications of the finite-frequency theory to date (Hung *et al.* 2004; Montelli *et al.* 2006; Yang *et al.* 2006; Chen *et al.* 2007). In this paper, we document the contributions of  $S$  wave speed perturbations to the  $P$ -wave traveltimes and amplitude anomalies using numerical and analytical solutions. We conclude that neglecting the cross-dependence between  $P$  waveforms and  $S$  wave speed perturbations distorts the forward relation between the wave propagation medium and observations and may cause a systematic bias in the solution of  $P$  wave speeds.

## MODELS AND RESULTS

To demonstrate the cross-dependence of  $P$  and  $S$  waveforms and wave speed perturbations, we carry out numerical experiments using a 3-D staggered-grid, finite-difference method (Olsen 1994). We use a simple homogenous model as our reference model, so the results can be compared to and also analysed with the analytical solutions. The  $P$  and  $S$  wave speeds in the reference model are 6.5 and 3.5 km s<sup>-1</sup>, respectively. The grid spacing is 200 m, and the time step 0.01 s. We introduce a cylindrical-shaped velocity perturbation with a radius of 3 km, a height of 6 km at various depths along a vertical line between the source and receiver, the axis of which is always oriented vertically in the  $Z$  direction (Fig. 1). The traveltime and amplitude anomalies caused by the wave speed perturbation are measured by cross-correlation of the waveforms with and without the wave speed perturbation. For simplicity, an explosive source with a dominant period of 1.2 s is used to observe the direct  $P$  arrival. When only the  $P$  or  $S$  wave speed is perturbed, the sensitivities to the  $P$  or  $S$  wave speed perturbations (Fig. 2) calculated using the scattering-integral method (Appendix A) predict

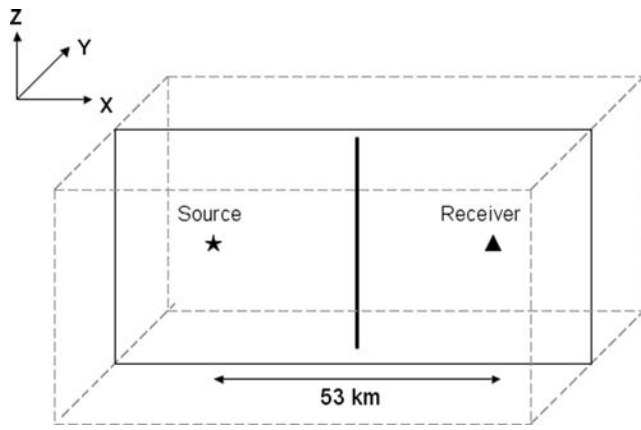


**Figure 1.** The geometry of the homogeneous and isotropic model used in the numerical simulations. The rectangle with solid lines shows the vertical cross-section of the model containing the source (star) and receiver (triangle). The horizontal distance from the source to the receiver is 53 km, or approximately 7.4 wavelengths of the dominant  $P$  wave. The vertical line in between the source and receiver shows where a cylindrical-shaped wave speed anomaly is placed.

the  $P$  traveltime and amplitude anomalies that accurately match the direct waveform cross-correlation measurements (Fig. 3). Since the density remains the same in all the calculations, a perturbation in only the  $P$  wave speed is equivalent to a perturbation in the bulk modulus, while a perturbation in only the  $S$  wave speed corresponds to changes in both the bulk and shear moduli. When both the  $P$  and  $S$  wave speeds are perturbed within the cylindrical anomaly, however, the predicted  $P$  traveltime and amplitude anomalies from the sensitivities to  $P$  wave speed perturbations alone do not match the direct waveform cross-correlation measurements (Fig. 3). Only after we add the contributions from the sensitivities of the  $P$  arrival to  $S$  wave speed perturbations, do the kernel predictions match the values from the direct waveform cross-correlation, indicating that  $S$  wave speed perturbations affect the  $P$  arrival. On the other hand,  $P$  wave speed perturbations have little effect on the direct  $S$  arrival in the experiment using a double-couple source to generate  $S$  waves (Fig. 3).

The sensitivities of  $P$  traveltime to  $P$  wave speed perturbations ( $K_{\alpha,p}^P$ , Fig. 2) are similar to the classic ‘banana–doughnut’ kernels of Dahlen *et al.* (2000), with a minimum sensitivity along the ray path, though in this study the ray path is a straight line and the kernels are calculated from the full wavefield. In contrast, the sensitivities of  $P$  traveltime to  $S$  wave speed perturbations are at the maximum along the ray path ( $K_{\beta,p}^P$ ). The patterns of the sensitivities for  $P$  amplitude variation to  $P$  and  $S$  wave speed perturbations are also reversed: the maximum amplitude sensitivities along the ray path for  $P$  wave speed perturbations ( $K_{\alpha,q}^P$ ) and minimum sensitivities along the ray path for  $S$  wave speed perturbations ( $K_{\beta,q}^P$ ).

In a homogeneous and isotropic medium, as in the above numerical experiments, the sensitivity kernels to  $P$  and  $S$  wave speed perturbations can also be calculated from the analytical wavefield solutions (Aki & Richards 2002) and the results confirm the finite-difference calculations. Using various combinations of the near- and far-field terms for the source and receiver, we find that both the far- and near-field terms from the source and receiver contribute to the  $P$  traveltime and amplitude sensitivities to  $S$  wave speed perturbations. In particular, the near- and mid-field terms are mainly responsible for the sensitivities along the ray path (more in the following section). Furthermore, the ratio of the maximum, absolute

traveltime sensitivities to  $S$  wave speed and  $P$  wave speed perturbations ( $K_{\beta,p}^P/K_{\alpha,p}^P$ ) is approximately  $4\lambda_P\beta^2/(l\alpha^2)$  at the mid point between the source and receiver, where  $\lambda_P$  is the wavelength of the  $P$  wave,  $l$  the source–receiver distance,  $\alpha$  the  $P$  wave speed, and  $\beta$  the  $S$  wave speed. Using the parameters in our numerical experiments (Fig. 1), we find a ratio of about 0.17, consistent with the sensitivity kernels (Fig. 2) and direct waveform cross-correlation measurements (Fig. 3).

Although a homogeneous and isotropic medium is an oversimplification of the real Earth, the above formula for the relative magnitude of the sensitivities to  $P$  and  $S$  wave speed perturbations provides a simple way to assess, to the first order, the condition under which the contributions of  $S$  wave speed perturbations to  $P$  waveforms are nontrivial. For a medium with a  $\alpha/\beta$  of 1.7–2.0, a value suitable for most of the solid earth, the ratio of the maximum traveltime sensitivities to  $S$  wave speed and  $P$  wave speed perturbations at the mid point between the source and receiver decreases from  $\sim 0.17$  for a source–receiver geometry with  $l/\lambda_P$  of  $\sim 7.4$  to  $\sim 0.017$  for a  $P$  wave of the same wavelength at 10 times the propagation distance ( $l/\lambda_P = 74$ ).

To assess the global relative contributions of  $P$  and  $S$  wave speed perturbations to  $P$  traveltimes and amplitudes, we integrate the absolute values of the sensitivities over the entire volume. For  $P$ -wave traveltimes, the ratio of the integrated absolute values ( $K_{\beta,p}^P/K_{\alpha,p}^P$ ) varies from 4.1 per cent at  $l/\lambda_P$  of  $\sim 600$  to 31 per cent at  $l/\lambda_P$  of  $\sim 7$  (Fig. 4). For  $P$ -wave amplitude anomalies, the ratio of the integrated absolute values ( $K_{\beta,q}^P/K_{\alpha,q}^P$ ) changes from 2.7 to 49 per cent at the same corresponding distances.

## DISCUSSION

In the above calculations, the magnitude of  $S$  wave speed perturbations is the same as the magnitude of  $P$  wave speed perturbations. In the real Earth,  $S$  wave speed variations are usually larger than  $P$  wave speed variations in percentage (e.g. Karato & Karki 2001). One per cent of partial melt in the upper mantle, for example, is estimated to cause 3.6 per cent  $P$  wave speed reduction and 7.9 per cent  $S$  wave speed reduction (Hammond & Humphreys 2000). The net effect of a larger  $S$  wave speed perturbation than the  $P$  wave speed change is an increase of the contribution and importance of  $S$  wave speed variations to  $P$  waveforms.  $P$  and  $S$  wave speed variations are also often coupled in the real earth. In such a case, a small-scale perturbation along the ray path affects  $P$  waveforms when both  $P$  and  $S$  wave speeds are taken into consideration. This proves to be important in the numerical validation of the sensitivity kernels (Fig. 3).

Separating the far-field term (with  $1/r$  decay, where  $r$  is the distance to the source or receiver) from the mid- and near-field terms (with  $1/r^2$  decay and  $1/r^3$  decay, respectively) in the analytical solution of a homogeneous and isotropic medium (Aki & Richards 2002), we find that the sensitivities of  $P$  traveltime to  $P$  wave speed perturbations calculated from the far-field alone are the same as the ‘banana–doughnut’ kernels of Dahlen *et al.* (2000), with a zero traveltime sensitivity along the ray path (Fig. 5). The far-field  $P$  traveltime sensitivity to  $S$  wave speed perturbations is also zero along the ray path. However, off the ray path the sensitivity is nontrivial compared to the sensitivity to  $P$  wave speed perturbations (Fig. 5). Unlike the scattering of a  $P$  wave by a  $P$  wave speed perturbation, the far-field Rayleigh scattering coefficient of a scattered  $P$  wave due to an  $S$  wave speed perturbation is zero on the ray path (fig. 4

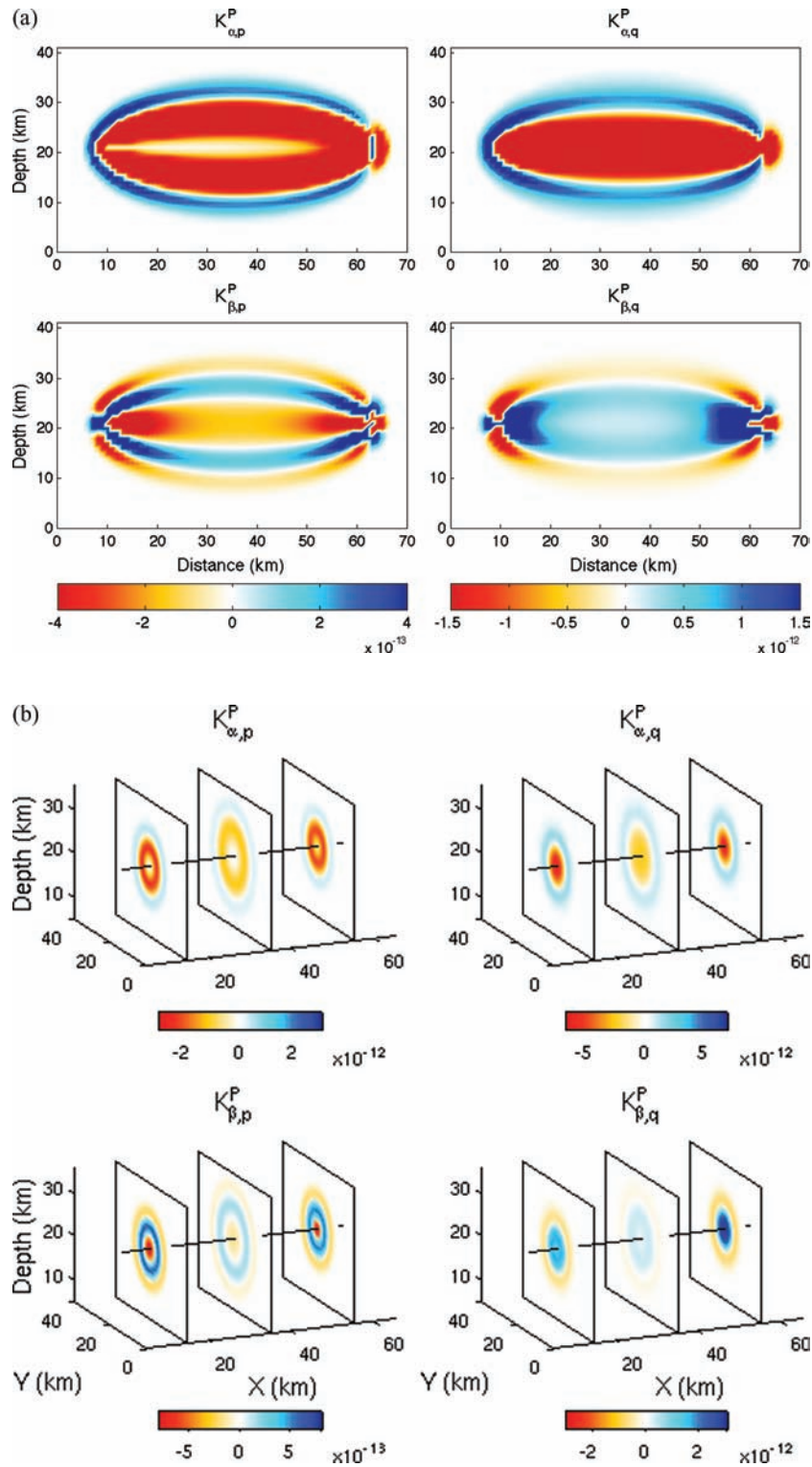


**Figure 2.** (a) The sensitivity kernels for the horizontal component of the direct  $P$  arrival in the vertical plane containing the source and receiver.  $K_{\alpha,p}^P$  and  $K_{\alpha,q}^P$  are the traveltime and amplitude sensitivity kernels to  $P$  wave speed perturbations, respectively;  $K_{\beta,p}^P$  and  $K_{\beta,q}^P$  are the traveltime and amplitude sensitivities to  $S$  wave speed perturbations, respectively. The unit of the traveltime sensitivity is s m<sup>-3</sup> and that of the amplitude sensitivity is m<sup>-3</sup> (Zhang *et al.* 2007). (b) The  $K_{\alpha,p}^P$ ,  $K_{\alpha,q}^P$ ,  $K_{\beta,p}^P$  and  $K_{\beta,q}^P$  sensitivities at three vertical planes perpendicular to the ray path. The black line crossing the three planes represents the ray path. The source is located at the left-hand side of this figure. The three planes are 6.5, 26.5 and 46.5 km away from the source, respectively. Less saturated and different colour scales are used to illustrate the details of the kernels.

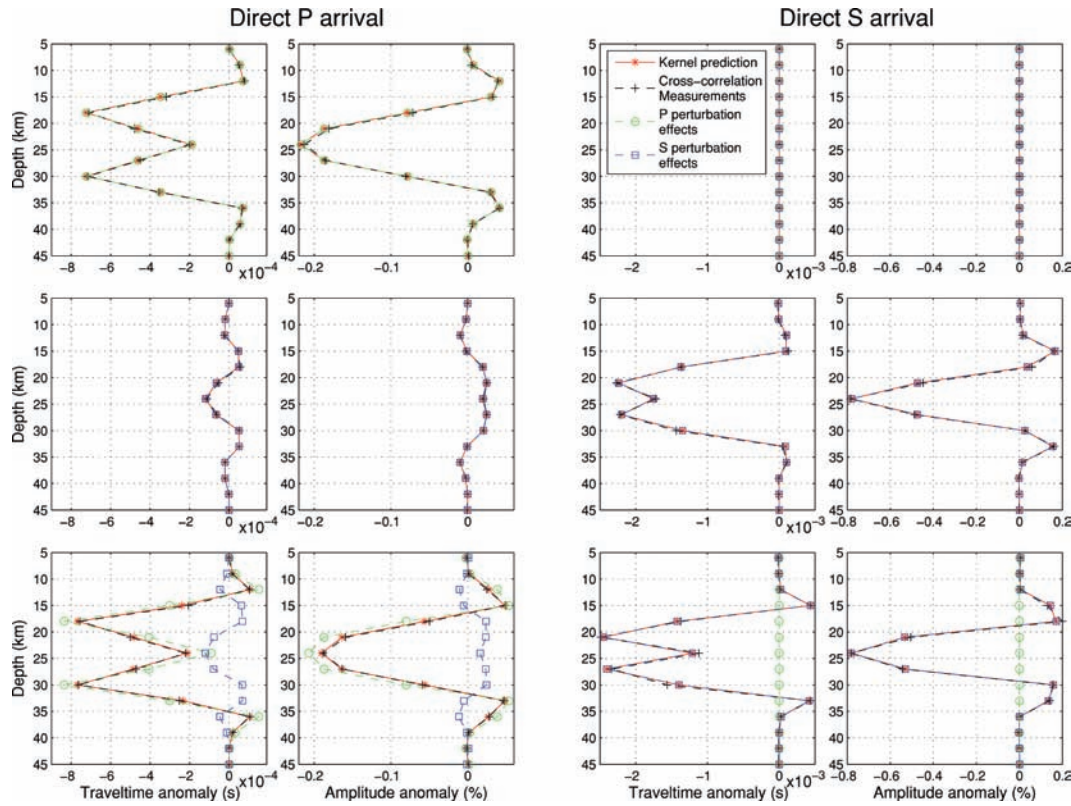


**Figure 3.** The waveform cross-correlation measurements of the traveltime and amplitude anomalies caused by the cylindrical-shaped wave speed perturbation are compared to the predicted values from the sensitivity kernels. The horizontal axes are traveltime or amplitude anomaly, and the vertical axes are the depth of the centre of the cylindrical-shaped wave speed perturbation along the vertical line between the source and receiver in Fig. 1. The left-hand panels are for the direct  $P$  arrival. The right-hand panels are for the direct  $S$  arrival when a double couple source is used. The top row is for the model with only  $P$  wave speed perturbations (a square cosine function with the 3 per cent maximum at the centre of the perturbation and zeros at the boundaries), the middle row for the model with only  $S$  wave speed perturbations of the same magnitude, and the bottom row for the model with both  $P$  and  $S$  wave speed perturbations (3 per cent uniform).

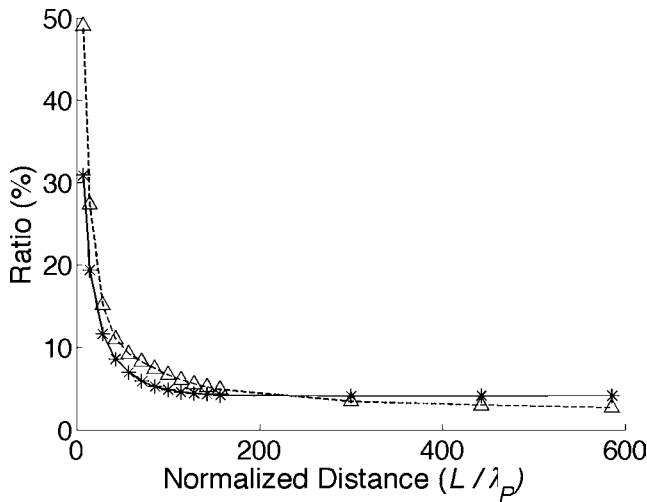


**Figure 4.** The relative magnitudes of the integrated absolute  $P$  traveltime (asterisk) and amplitude (triangle) sensitivities to  $S$  and  $P$  wave speed perturbations vary with the normalized distance between the source and receiver. The  $P$  and  $S$  wave speeds of the medium and the source time function are the same as in the numerical experiment (Fig. 1). At one wavelength distance, the ratios are 110 per cent for traveltime and 540 per cent for amplitude (off scale).

in Dahlen *et al.* 2000). This causes a noticeably wider ‘doughnut’ hole in  $K_{\beta,p}^P$  compared to that of  $K_{\alpha,p}^P$ .

Keeping the far-field term on the source side but including also the near- and mid-field terms on the receiver side results in the  $P$  traveltime sensitivity to  $S$  wave speed perturbations along the ray path, with the most significant change on the receiver side (Fig. 6). The change of  $K_{\beta,p}^P$  from the zero sensitivity along the ray path in the case with only the far-field term (Fig. 5) to the local maximum sensitivity in Fig. 6 is attributed to two factors. First, the scattering coefficient for a mid-field scattered  $P$  wave due to an  $S$  wave speed perturbation is the maximum along the ray path (Aki & Richards 2002; Favier *et al.* 2004). Second, the mid-field term of a scattered wave is proportional to the time derivative of the reference displacement at the receiver (Aki & Richards 2002). For such a perturbed waveform, the delay time calculated by eq. (A1) in Appendix A is the maximum when there is no offset in the arrival times of the reference and scattered waves (in other word, when the scatter is on the ray path).

Replacing the far-field term on the source side with the near- and mid-field terms while keeping the full terms on the receiver side reveals that the near- and mid-field terms on the source side also contribute to the  $P$  traveltime sensitivity to  $S$  wave speed perturbations along and near the ray path, with a stronger sensitivity near the source (Fig. 7).



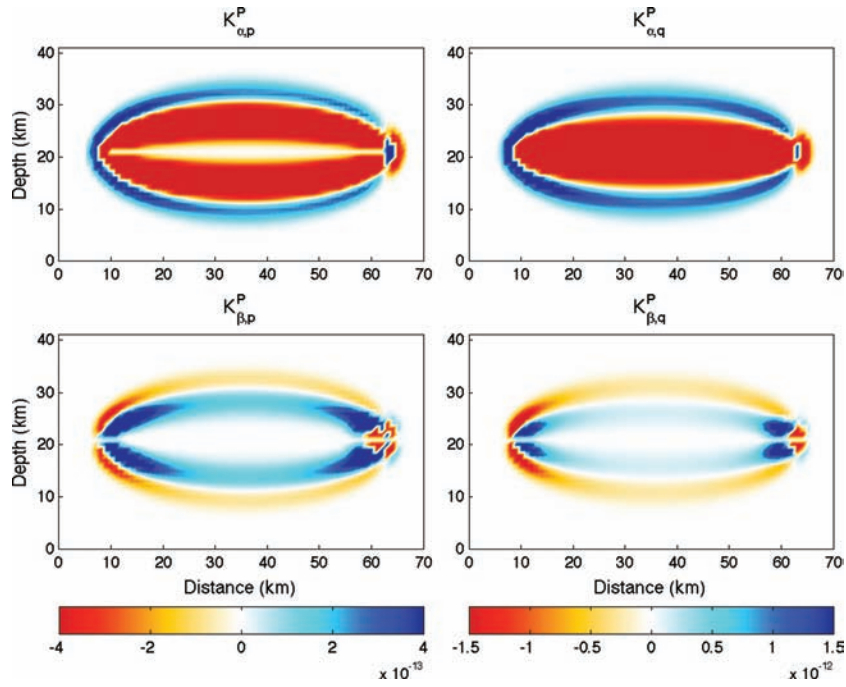


**Figure 5.** Far-field  $P$  traveltime and amplitude sensitivity kernels to  $P$  (top panels) and  $S$  (bottom panels) wave speed perturbations in the vertical plane containing the source and receiver. The units of the sensitivities are the same as in Fig. 2.

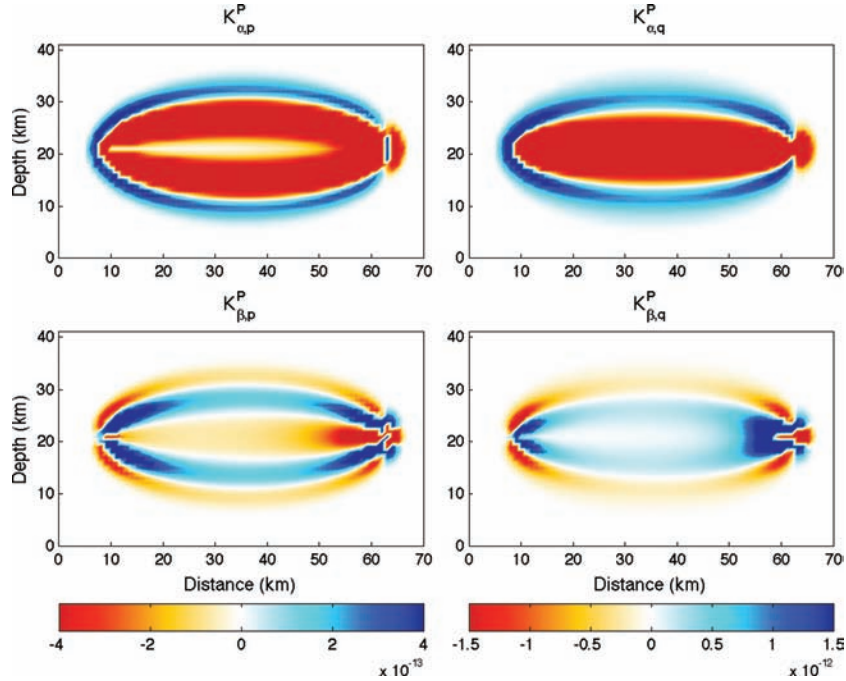


**Figure 6.** The  $P$  traveltime and amplitude sensitivity kernels to  $P$  (top panels) and  $S$  (bottom panels) wave speed perturbations are calculated with the contributions from the far-field term on the source side and all the field terms on the receiver side. The vertical cross-section contains the source and receiver and the units of the sensitivities are the same as in Fig. 2.

We note the sensitivity to  $S$  wave speed perturbations oscillates from negative to positive values away from the ray path (Figs 2, 3 and 6). Unlike the sensitivity to  $P$  wave speed perturbations, integration of the sensitivity to  $S$  wave speed perturbations in a plane perpendicular to the ray path causes the cancellation of the positive and negative values. A uniform  $S$  wave speed perturbation in a plane perpendicular to the ray path yields no travel time anomaly in the  $P$

arrival. This means that  $S$  wave speed perturbations that are much larger than the width of the Fresnel zone ( $\sim 2\sqrt{\lambda l}$  when  $l \gg \lambda$ , where  $l$  is the distance to the receiver and  $\lambda$  the wavelength, Dahlen *et al.* 2000) contribute little to  $P$  waveform perturbations. Integrating  $P$  delay times caused by the near-, mid- and far-field terms in planes perpendicular to the ray path, Favier *et al.* (2004) noted that the far-field term becomes predominant at distances greater than



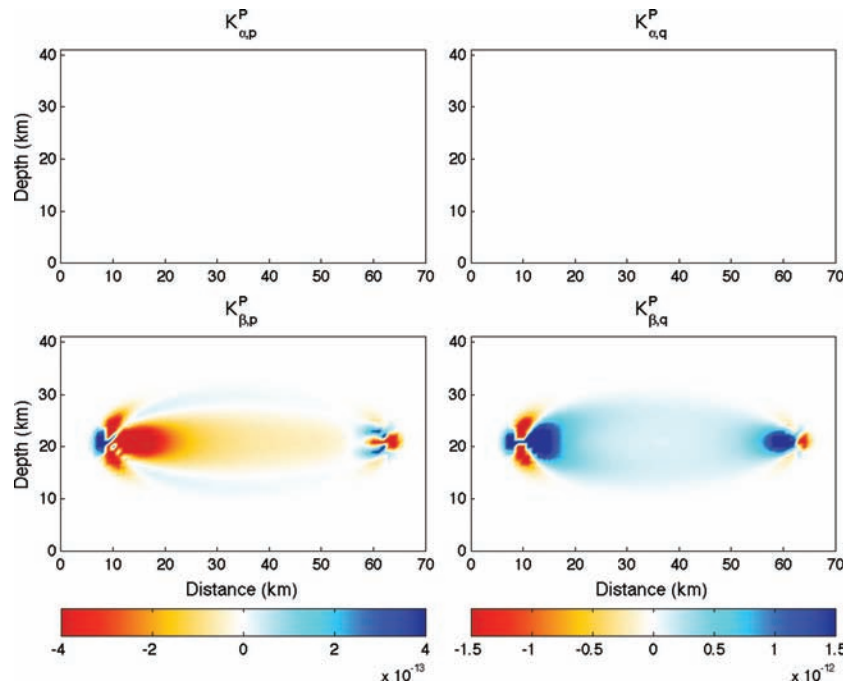


**Figure 7.** The  $P$  traveltime and amplitude sensitivity kernels to  $P$  (top panels) and  $S$  (bottom panels) wave speed perturbations are calculated with the contributions from the near- and mid-field terms on the source side and all the field terms on the receiver side. The vertical cross-section contains the source and receiver. The units of the sensitivities are the same as in Fig. 2.

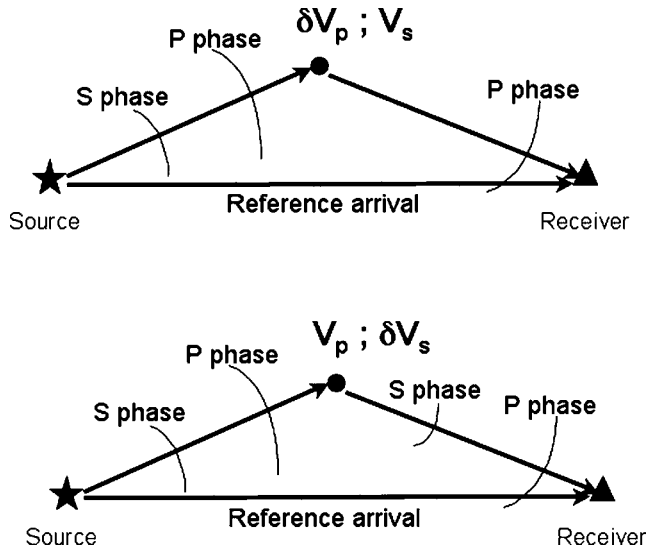


**Figure 8.** A cartoon illustrating wave propagation due to a scatter. The star represents a source, the triangle a receiver, and the circle a scatter. If only the  $P$  wave speed is perturbed, only  $P$  wave is scattered by the scatter (the upper figure). But both  $P$  and  $S$  waves are scattered if the  $S$  wave speed is perturbed (the lower figure).

1/20th wavelength from the receiver and concluded that the mid-field term cannot be neglected at distances within one wavelength from the receiver. However, for heterogeneities on the scale of, and smaller than, the width of the sensitivity kernels (in other words in places where the finite-frequency kernels matter for tomography), the absolute or maximum sensitivities are more meaningful values to assess the relative importance of the finite-frequency kernels to  $P$  and  $S$  wave speed perturbations. Fig. 4 shows that the contributions of  $S$  wave speed perturbations to  $P$  traveltime and amplitude anoma-

lies are substantial at distances within several tens of wavelengths from the source and receiver. So this cross-dependence of  $P$  traveltime and amplitude on  $S$  wave speed is a typical finite-frequency effect, important where the scale of the velocity heterogeneity is comparable or smaller than the Fresnel zone of the wave.

Our results differ from the common practice in tomographic inversion, in which  $P$ -wave traveltimes depend only on  $P$  wave speed and  $S$ -wave traveltimes only on  $S$  wave speed. This common practice may stem from two well-known theoretical derivations: the Helmholtz potential decomposition in a homogenous isotropic medium, and ray theory, in which the spatial gradients of the elastic properties are neglected under the high-frequency approximation (e.g. Dahlen & Tromp 1998; Aki & Richards 2002). The effects of  $S$  wave speed perturbations on  $P$  waveforms presented in this paper result from the terms neglected by ray theory. For general elastic media, the spatial gradients of the elastic properties result in a scalar ( $P$ ) wave potential that explicitly depends on the spatial gradient of the  $S$  wave speed (Appendix B). The finite-frequency kernels quantitatively reflect that there is only scattered  $P$  wave when only  $P$  wave speed is perturbed. But an  $S$  wave speed perturbation generates both scattered  $P$  and  $S$  wave (Fig. 8).

Although the reference model used in this paper is an isotropic and homogeneous medium, the spatial gradient in the elastic properties must be considered once a wave speed perturbation is introduced into the medium. The numerical approach shown in Fig. 2 can be applied to any general inhomogeneous media, in which the finite-frequency phenomena documented in this paper should also exist.

## CONCLUSIONS

For finite-frequency waves,  $S$  wave speed perturbations may have significant effects on  $P$  waveforms. Whether this cross-dependence is small enough to be neglected depends on the scale of wave speed

heterogeneities in the Earth and achievable resolution in specific studies. At short source–receiver distances (Fig. 4) and near the source and receiver, the cross-dependence of  $P$  waveforms on  $S$  wave speed is substantial. This has important implications for seismic tomography, particularly for regional teleseismic tomography and local earthquake tomography, in which the volume of interest is often within several 10s of wavelength from receivers or both sources and receivers. Even for regions far from sources and receivers, neglecting this cross-dependence means that the estimate of the  $P$  wave speed near the source (e.g. subduction zone) and receiver is likely biased and such errors may propagate into the rest of the model in tomographic inversions. When the goal of tomographic inversion is to place constraints on thermal and compositional variations in the crust and mantle, the cross-dependence of  $P$  waveforms on  $S$  wave speed variations documented above becomes important and requires a joint solution of both the  $P$  and  $S$  wave speed structures.

## ACKNOWLEDGMENTS

Kim Olsen provided the finite-difference waveform simulation code used in the waveform simulation. We thank Wei Zhang and Li Zhao for discussions, Po Chen and an anonymous reviewer for constructive reviews. This work was supported by Air Force Research Laboratory FA8718-06-C-0014 and U.S. National Science Foundation under grant no. 0241655.

## REFERENCES

- Aki, K. & Richards, P.G., 2002. *Quantitative Seismology*, University Science Books, Sausalito, California.
- Baig, A.M., Dahlen, F.A. & Hung, S.-H., 2003. Traveltimes of waves in three-dimensional random media, *Geophys. J. Int.*, **153**, 467–482.
- Chen, P., Zhao, L. & Jordan, T.H., 2007. Full 3D tomography for crustal structure of the Los Angeles Region, *Bull. seism. Soc. Am.*, **97**(4), 1094–1120, doi:10.1785/0120060222.
- Dahlen, F.A., Nolet, G. & Hung, S.-H., 2000. Fréchet kernels for finite-frequency traveltime. I: theory, *Geophys. J. Int.*, **141**, 157–174.
- Dahlen, F.A., & Tromp, J., 1998. *Theoretical Global Seismology*, Princeton University Press, Princeton, New Jersey.
- Dziewonski, A.M. & Anderson, D.L., 1984. Seismic tomography of the Earth's interior, *Am. Sci.*, **72**, 483–494.
- Favier, N., Chevrot, S. & Komatitsch, D., 2004. Near-field influence on shear wave splitting and traveltime sensitivity kernels, *Geophys. J. Int.*, **156**, 467–482, doi:10.1111/j.1365-246X.2004.02178.x.
- Grand, S.P., 1987. Tomographic inversion for shear velocity beneath the North American plate, *J. geophys. Res.*, **92**, 14 065–14 090.
- Hung, S.-H., Dahlen, F.A. & Nolet, G., 2000. Fréchet kernels for finite-frequency traveltimes—II, Examples, *Geophys. J. Int.*, **141**, 175–203.
- Hung, S.-H., Shen, Y., & Chiao, L.-Y., 2004. Imaging seismic velocity structure beneath the Iceland hotspot – A finite frequency approach, *J. geophys. Res.*, **109**, B08305, doi:10.1029/2003JB002889.
- Hammond, W. C. & Humphreys, E. D., 2000. Upper mantle seismic wave velocity: Effects of realistic partial melt geometries, *J. geophys. Res.*, **105**, 10 975–10 986.
- Karato, S. & Karki, B.B., 2001. Origin of lateral variation of seismic wave velocities and density in the deep mantle, *J. geophys. Res.*, **106**, 21 771–21 783.
- Liu, Q. & Tromp, J., 2006. Finite-frequency kernels based on adjoint methods, *Bull. seism. Soc. Am.*, **96**, 2383–2397, doi:10.1785/0120060041.
- Montelli, R., Nolet, G., Dahlen, F.A. & Masters, G., 2006. A catalogue of deep mantle plumes: new results from finite-frequency tomography, *Geochim. Geophys. Geosyst.*, **7**, Q11007, doi:10.1029/2006GC001248.
- Olsen, K.B., 1994. Simulation of three-dimensional wave propagation in the Salt Lake Basin, *PhD thesis*. University of Utah, Salt Lake City, Utah, 157p.
- Tanimoto, T., 1995. Formalism for traveltime inversion with finite frequency effect, *Geophys. J. Int.*, **121**, 103–110.
- Tromp, J., Tape, C.H., & Liu, Q., 2005. Seismic tomography, adjoint methods, time reversal, and banana-doughnut kernels, *Geophys. J. Int.*, **160**, 195–216.
- Van Der Hilst, R.D., Widyantoro, S. & Engdahl, E.R., 1997. Evidence for deep mantle circulation from global tomography, *Nature*, **386**, 578–584.
- Wu, R. & Aki, K., 1985. Scattering characteristics of elastic waves by an elastic heterogeneity, *Geophysics*, **50**, 582–595.
- Yang, H.-Y. & Hung, S.-H., 2005. Validation of ray and wave theoretical travel times in heterogeneous random media, *Geophys. Res. Lett.*, **32**, L20302, doi:10.1029/2005GL023501.
- Yang, T., Shen, Y., Van Der Lee, S., Solomon, S.C. & Hung, S.-H., 2006. Upper mantle structure beneath the Azores hotspot from finite-frequency seismic tomography, *Earth planet. Sci. Lett.*, **250**, 11–26.
- Zhang, Z., Shen, Y. & Zhao, L., 2007. Finite-frequency sensitivity kernels for head waves, *Geophys. J. Int.*, **171**, 847–856, doi:10.1111/j.1365-246X.2007.03575.x.
- Zhao, D., Hasegawa, A. & Horiuchi, S., 1992. Tomographic imaging of  $P$  and  $S$  wave velocity structure beneath northeastern Japan, *J. geophys. Res.*, **97**, 19 909–19 928.
- Zhao, L., Jordan, T.H. & Chapman, C.H., 2000. Three-dimensional Fréchet differential kernels for seismic delay times, *Geophys. J. Int.*, **141**, 558–576.
- Zhao, L., Jordan, T.H., Olsen, K.B. & Chen, P., 2005. Fréchet kernels for imaging regional earth structure based on three-dimensional reference models, *Bull. seism. Soc. Am.*, **95**(6), 2066–2080, doi:10.1785/0120050081.

## APPENDIX A: CALCULATION OF THE SENSITIVITIES BY THE SCATTERING INTEGRAL METHOD

We define the traveltime and amplitude anomalies,  $\delta\tau_p$  and  $\delta A_q$ , respectively, as (Tanimoto 1995; Dahlen *et al.* 2000; Zhao *et al.* 2005):

$$\delta\tau_p = -\frac{\int_{t_1}^{t_2} \dot{\tilde{u}}_l(t) \delta u_l(t) dt}{\int_{t_1}^{t_2} |\dot{\tilde{u}}_l(t)|^2 dt} \quad (\text{A1})$$

$$\delta A_q = -\frac{\int_{t_1}^{t_2} \tilde{u}_l(t) \delta u_l(t) dt}{\int_{t_1}^{t_2} |\tilde{u}_l(t)|^2 dt}, \quad (\text{A2})$$

where  $\tilde{u}_l(t)$  is the displacement calculated from the reference model in the direction  $\hat{e}_l$ , a unit vector;  $\delta u_l(t) = u_l(t) - \tilde{u}_l(t)$ ;  $u_l(t)$  is the displacement for the perturbed velocity model; a dot represent the time derivative;  $t_1$  and  $t_2$  are the upper and lower limit of the time window of the arrival. The amplitude anomaly defined here is different from that in Zhao *et al.* (2005) by a constant. Following the same algebra in Zhao *et al.*

(2005), we have:

$$K_{\alpha,p} = \frac{1}{P_l} \int_{t_1}^{t_2} 2\tilde{\rho}\tilde{\alpha}\dot{\tilde{u}}_l(r_R, t; r_S) \int_{-\infty}^{\infty} \hat{e}_l \cdot [(\nabla \cdot \tilde{G}^T)(\nabla \cdot \tilde{u})] d\tau dt \quad (A3)$$

$$K_{\alpha,p} = \frac{1}{Q_l} \int_{t_1}^{t_2} 2\tilde{\rho}\tilde{\alpha}\tilde{u}_l(r_R, t; r_S) \int_{-\infty}^{\infty} \hat{e}_l \cdot [(\nabla \cdot \tilde{G}^T)(\nabla \cdot \tilde{u})] d\tau dt \quad (A4)$$

$$K_{\beta,p} = \frac{1}{P_l} \int_{t_1}^{t_2} 2\tilde{\rho}\tilde{\beta}\dot{\tilde{u}}_l(r_R, t; r_S) \int_{-\infty}^{\infty} \hat{e}_l \cdot \{((\nabla \tilde{G}^{213}) : [(\nabla \tilde{u}) + (\nabla \tilde{u})^T] - 2(\nabla \cdot \tilde{G}^T)(\nabla \cdot \tilde{u}))\} d\tau dt \quad (A5)$$

$$K_{\beta,p} = -\frac{1}{Q_l} \int_{t_1}^{t_2} 2\tilde{\rho}\tilde{\beta}\tilde{u}_l(r_R, t; r_S) \int_{-\infty}^{\infty} \hat{e}_l \cdot \{((\nabla \tilde{G}^{213}) : [(\nabla \tilde{u}) + (\nabla \tilde{u})^T] - 2(\nabla \cdot \tilde{G}^T)(\nabla \cdot \tilde{u}))\} d\tau dt, \quad (A6)$$

where the  $\tilde{G}$  is the Green's tensor. The symbol  $()^{213}$  represents the transposition of the first and the second indices of a third-order tensor.  $P_l$  and  $Q_l$  are the normalization factor in the direction  $\hat{e}_l$ , which are:

$$P_l = \int_{t_1}^{t_2} |\dot{\tilde{u}}_l(t)|^2 dt \quad (A7)$$

$$Q_l = \int_{t_1}^{t_2} |\tilde{u}_l(t)|^2 dt. \quad (A8)$$

For the direct  $P$  wave, for example, the sensitivity kernels to  $P$  and  $S$  wave speed perturbations,  $K_{\alpha,p}^P$  and  $K_{\beta,p}^P$ , are calculated from eq. (A3) and (A5), respectively, with a time window  $(t_1, t_2)$  that contains the  $P$  arrival.

## APPENDIX B: WAVE EQUATION REPRESENTED BY THE HELMHOLTZ POTENTIAL

The cross-dependence of  $P$  waveforms to  $S$  wave speed perturbations and the lack of effects of  $P$  wave speed perturbations to  $S$  waveforms can be understood from the elastodynamic equation,

$$\rho \ddot{\vec{u}} = \nabla \cdot \vec{\sigma}, \quad (A9)$$

where  $\rho$  is density,  $\vec{u}$  displacement, and  $\vec{\sigma}$  stress. For simplicity, the body force term is omitted in the equation. The displacement can be represented by the Helmholtz scalar potential of  $P$  wave,  $\phi$ , and the vector potential of  $S$  wave,  $\vec{\psi}$  (e.g. Aki & Richards 2002),

$$\vec{u} = \nabla\phi + \nabla \times \vec{\psi} \quad \text{with} \quad \nabla \cdot \vec{\psi} = 0. \quad (A10)$$

Using the linear, isotropic stress–strain relationship, taking the divergence and curl of eq. (A9), and assuming a constant density, we have,

$$\nabla^2 \ddot{\phi} = \nabla^2 (\alpha^2 \nabla^2 \phi) + 2\nabla \cdot [\nabla \nabla \times \vec{\psi} \cdot \nabla \beta^2 + \nabla \nabla \phi \cdot \nabla \beta^2 - \nabla \beta^2 \nabla^2 \phi] \quad (A11)$$

$$\nabla \times \nabla \times \ddot{\vec{\psi}} = -\nabla \times \nabla \times [\beta^2 \nabla \times \nabla \times \vec{\psi}] + 2\nabla \times [\nabla \nabla \times \vec{\psi} \cdot \nabla \beta^2 + \nabla \nabla \phi \cdot \nabla \beta^2 - \nabla \beta^2 \nabla^2 \phi]. \quad (A12)$$

While eq. (A11) shows that the  $P$ -wave scalar potential  $\phi$  is explicitly related to the  $P$  wave speed,  $\alpha$ , and the spatial gradient of the  $S$  wave speed,  $\beta$ , the  $S$ -wave vector potential  $\vec{\psi}$  is related only to  $\beta$  in eq. (A12). Although eq. (A12) includes two terms related to  $\phi$ , they have no effect on  $\vec{\psi}$ , where the spatial gradient in  $S$  wave speed is zero or when  $\vec{\psi}$  and  $\phi$  are separated in the time domain.

# APPENDIX D

## AGU Abstracts

Shen, Y., W. Zhang, Y. Ren, and X. Liang, Imaging the crust and upper mantle in the southern and southeastern Tibetan plateau: A three-dimensional full-wavefield approach, *Eos Trans. AGU*, 89(53), Fall Meet. Suppl., abstract T11E-06 Invited, 2008b.

Finite-frequency, teleseismic traveltime tomography based on body-wave ray theory in conjunction with the Born approximation has shown wave-speed anomalies that are indicative of the delamination of the mantle lithosphere and possibly part of the lower crust as a likely cause for the north-south-trending rifts in the southern and southeastern Tibetan plateau. The images also show evidence that contradicts the notion of substantial under-thrusting of the Indian mantle lithosphere beneath southern and southeastern Tibet. To further improve resolution and verify the interpretations, we carry out a three-dimensional (3D) full-wavefield finite-frequency tomography study of the area, incorporating regional earthquakes and ambient signals recorded by the permanent and portable broadband seismic stations. The new approach accounts for complex wave propagation, enables fuller utilization of an arrival on all three components of seismic records, and linearizes the inverse problem by iteratively updating the 3D reference model. An important benefit of this physically realistic modeling of full wavefield is the consistency of the system of equations in inversion, which is particularly important for the integration of different types of observations and physical properties. We calculate synthetic waveforms using a non-staggered grid finite-difference code in a polar-spherical coordinate system. Frequency-dependent phase and amplitude anomalies are measured by the cross-correlation between synthetic and recorded seismograms. The finite-frequency structural sensitivity kernels of these measurements are calculated by the scattering-integral method. The final joint 3D P- and S-speed structural model is obtained through a non-linear iterative process. The results will be used to address the questions about the under-thrusting of the Indian mantle lithosphere, the origin of the north-south-trending rifts, crustal and mantle lithosphere delamination, and their implications for the rise of the Tibetan plateau.

Zhang, Z., Y. Shen, W. Zhang, Full-wave finite-frequency tomography of the southeast Tibetan plateau, American Geophysical Union Fall Meeting (abstract S31D-08), 2009.

We carry out a full-wave finite-frequency tomography of the Tibetan plateau using the scattering-integral method. We use about 110 stations from the PASSCAL experiments in the region, which include the HIMNT, MIT-China and Namche-Barwa experiments. We start by re-locating the earthquakes and re-determining the focal mechanisms using 3-D strain Green Tensors. The Harvard CMT solutions, if available, are used as initial solutions of the iteration. We then calculate the synthetic wave field using the updated source locations and focal mechanisms in a 3D reference model. Finite-frequency traveltimes measured by cross-correlating observed and synthetic waveforms are inverted for wave-speed perturbations to the 3D reference model. We iteratively redo the two steps to improve the quality of the tomographic images. After two iterations, the model reveals strong velocity heterogeneities, with local changes of  $\pm 10\%$  relative to the initial reference model (CUB 2.0). It shows low velocity anomalies between the Bangong-

Nujiang Suture and the Indus-Tsangpo Suture for both  $V_p$  and  $V_s$  velocities in a depth range of 30km to 100km. This result implies that the Indian mantle lithosphere does not underthrust beyond the Indus-Tsangpo Suture in eastern Tibet.